

1 SEARCH FOR PRODUCTION OF A HIGGS BOSON AND A SINGLE TOP  
2 QUARK IN MULTILEPTON FINAL STATES IN  $pp$  COLLISIONS AT  $\sqrt{s} = 13$   
3 TeV.

4 by

5 Jose Andres Monroy Montañez

# A DISSERTATION

7 Presented to the Faculty of

8 The Graduate College at the University of Nebraska

In Partial Fulfilment of Requirements

10 For the Degree of Doctor of Philosophy

11 Major: Physics and Astronomy

12 Under the Supervision of Kenneth Bloom and Aaron Dominguez

13 Lincoln, Nebraska

14 July, 2018

15 SEARCH FOR PRODUCTION OF A HIGGS BOSON AND A SINGLE TOP  
16 QUARK IN MULTILEPTON FINAL STATES IN pp COLLISIONS AT  $\sqrt{s} = 13$   
17 TeV.

18 Jose Andres Monroy Montañez, Ph.D.

19 University of Nebraska, 2018

20 Adviser: Kenneth Bloom and Aaron Dominguez

# **<sup>21</sup> Table of Contents**

<b><sup>22</sup> Table of Contents</b>	<b>iii</b>
<b><sup>23</sup> List of Figures</b>	<b>vii</b>
<b><sup>24</sup> List of Tables</b>	<b>x</b>
<b><sup>25</sup> 1 INTRODUCTION</b>	<b>1</b>
<b><sup>26</sup> 2 Theoretical approach</b>	<b>2</b>
<sup>27</sup> 2.1 Introduction . . . . .	2
<sup>28</sup> 2.2 Standard model of particle physics . . . . .	3
<sup>29</sup> 2.2.1 Fermions . . . . .	5
<sup>30</sup> 2.2.1.1 Leptons . . . . .	6
<sup>31</sup> 2.2.1.2 Quarks . . . . .	9
<sup>32</sup> 2.2.2 Fundamental interactions . . . . .	13
<sup>33</sup> 2.2.3 Gauge bosons . . . . .	19
<sup>34</sup> 2.3 Electroweak unification and the Higgs mechanism . . . . .	20
<sup>35</sup> 2.3.1 Spontaneous symmetry breaking (SSB) . . . . .	28
<sup>36</sup> 2.3.2 Higgs mechanism . . . . .	32
<sup>37</sup> 2.3.3 Masses of the gauge bosons . . . . .	35

38	2.3.4	Masses of the fermions . . . . .	36
39	2.3.5	The Higgs field . . . . .	37
40	2.3.6	Production of Higgs bosons at LHC . . . . .	38
41	2.3.7	Higgs boson decay channels . . . . .	42
42	2.4	Associated production of a Higgs boson and a single Top quark. . . . .	43
43	2.5	The CP-mixing in tH processes . . . . .	47
44	2.6	Experimantal status of the anomalous Higg-fermion coupling. . . . .	52
45	<b>3</b>	<b>The CMS experiment at the LHC</b>	<b>54</b>
46	3.1	Introduction . . . . .	54
47	3.2	The LHC . . . . .	55
48	3.3	The CMS experiment . . . . .	65
49	3.3.1	Coordinate system . . . . .	67
50	3.3.2	Pixels detector . . . . .	68
51	3.3.3	Silicon strip tracker . . . . .	70
52	3.3.4	Electromagnetic calorimeter . . . . .	72
53	3.3.5	Hadronic calorimeter . . . . .	73
54	3.3.6	Superconducting solenoid magnet . . . . .	75
55	3.3.7	Muon system . . . . .	76
56	3.3.8	CMS trigger system . . . . .	77
57	3.3.9	CMS computing . . . . .	79
58	<b>4</b>	<b>Event generation, simulation and reconstruction</b>	<b>83</b>
59	4.1	Event generation . . . . .	84
60	4.2	Monte Carlo Event Generators. . . . .	88
61	4.3	CMS detector simulation. . . . .	89
62	4.4	Event reconstruction. . . . .	91

63	4.4.1	Particle-Flow Algorithm. . . . .	91
64	4.4.1.1	Missing transverse energy. . . . .	103
65	4.4.2	Event reconstruction examples . . . . .	104
66	<b>5</b>	<b>Statistical methods</b>	<b>107</b>
67	5.1	Multivariate analysis . . . . .	107
68	5.1.1	Decision trees . . . . .	110
69	5.1.2	Boosted decision trees (BDT). . . . .	113
70	5.1.3	Overtraining. . . . .	116
71	5.1.4	Variable ranking. . . . .	116
72	5.1.5	BDT output example. . . . .	117
73	5.2	Statistical inference. . . . .	118
74	5.2.1	Nuisance parameters. . . . .	118
75	5.2.2	Maximum likelihood estimation method . . . . .	119
76	5.2.3	Hypothesis test . . . . .	120
77	5.3	exclusion limits . . . . .	121
78	5.4	asymptotic limits . . . . .	121
79	<b>6</b>	<b>Search for production of a Higgs boson and a single top quark in multilepton final states in pp collisions at <math>\sqrt{s} = 13</math> TeV</b>	<b>122</b>
81	6.1	Introduction . . . . .	122
82	6.2	$tHq$ signature . . . . .	124
83	6.3	Background processes . . . . .	126
84	6.4	Data and MC Samples . . . . .	128
85	6.4.1	Full 2016 dataset and MC samples . . . . .	128
86	6.4.2	Triggers . . . . .	129
87	6.5	Object Identification . . . . .	133

88	6.5.1 Jets and $b$ tagging. . . . .	133
89	6.5.2 Missing Energy MET. . . . .	134
90	6.5.3 Lepton reconstruction and identification . . . . .	135
91	6.5.4 Lepton selection efficiency . . . . .	143
92	6.6 Event selection . . . . .	145
93	6.7 Background predictions . . . . .	146
94	6.8 Signal discrimination . . . . .	148
95	6.8.1 Classifiers response . . . . .	150
96	6.9 Additional discriminating variables . . . . .	154
97	<b>Bibliography</b>	<b>156</b>
98	<b>References</b>	<b>158</b>

# <sup>99</sup> List of Figures

100	2.1 Standard Model of particle physics. . . . .	4
101	2.2 Transformations between quarks . . . . .	12
102	2.3 Fundamental interactions in nature. . . . .	13
103	2.4 SM interactions diagrams . . . . .	14
104	2.5 Neutral current processes . . . . .	21
105	2.6 Spontaneous symmetry breaking mechanism . . . . .	29
106	2.7 SSB Potential form . . . . .	30
107	2.8 Potential for complex scalar field . . . . .	31
108	2.9 SSB mechanism for complex scalar field . . . . .	32
109	2.10 Proton-Proton collision . . . . .	39
110	2.11 Higgs boson production mechanism Feynman diagrams . . . . .	40
111	2.12 Higgs boson production cross section and decay branching ratios . . . . .	41
112	2.13 Associated Higgs boson production mechanism Feynman diagrams . . . . .	43
113	2.14 Cross section for tHq process as a function of $\kappa_t$ . . . . .	46
114	2.15 Cross section for $tHW$ process as a function of $\kappa_{Htt}$ . . . . .	47
115	2.16 NLO cross section for $tX_0$ and $t\bar{t}X_0$ . . . . .	50
116	2.17 NLO cross section for $tWX_0$ , $t\bar{t}X_0$ . . . . .	51

117	2.18 Two dimentional $\kappa_t$ - $\kappa_V$ plot of the coupling modifiers. ATLAS and CMS 118 combination. . . . .	52
119	3.1 CERN accelerator complex . . . . .	55
120	3.2 LHC protons source. First acceleration stage. . . . .	56
121	3.3 The LINAC2 accelerating system at CERN. . . . .	57
122	3.4 LHC layout and RF cavities module. . . . .	58
123	3.5 LHC dipole magnet. . . . .	60
124	3.6 Integrated luminosity delivered by LHC and recorded by CMS during 2016	62
125	3.7 LHC interaction points . . . . .	63
126	3.8 Multiple $pp$ collision bunch crossing at CMS. . . . .	65
127	3.9 Layout of the CMS detector . . . . .	66
128	3.10 CMS detector coordinate system . . . . .	67
129	3.11 CMS pixel detector schematic view. . . . .	70
130	3.12 SST Schematic view. . . . .	71
131	3.13 CMS ECAL schematic view . . . . .	72
132	3.14 CMS HCAL schematic view . . . . .	74
133	3.15 CMS solenoid magnet . . . . .	75
134	3.16 CMS Muon system schematic view . . . . .	76
135	3.17 CMS Level-1 trigger architecture . . . . .	78
136	3.18 WLCG structure . . . . .	80
137	3.19 Data flow from CMS detector through hardware Tiers . . . . .	82
138	4.1 Event generation process. . . . .	84
139	4.2 Particle flow algorithm. . . . .	92
140	4.3 Jet reconstruction. . . . .	100
141	4.4 Jet energy corrections. . . . .	101

142	4.5	Secondary vertex in a b-hadron decay.	102
143	4.6	HIG-13-004 Event 1 reconstruction.	104
144	4.7	$e\mu$ event reconstruction.	105
145	4.8	Recorded event reconstruction.	106
146	5.1	Scatter plots-MVA event classification.	109
147	5.2	Scalar test statistical.	109
148	5.3	Decision tree.	111
149	5.4	Decision tree output example.	114
150	5.5	BDT output example.	117
151	6.1	$tHq$ event signature.	125
152	6.2	$t\bar{t}$ and $t\bar{t}W$ events signature.	127
153	6.3	Tight vs loose lepton selection efficiencies in the 2lss channel.	143
154	6.4	Tight vs loose lepton selection efficiencies in the 3l channel.	144
155	6.5	Input variables to the BDT for signal discrimination normalized.	149
156	6.6	Input variables to the BDT for signal discrimination not normalized.	151
157	6.7	BDT inputs as seen by TMVA against $t\bar{t}$ .	152
158	6.8	BDT inputs as seen by TMVA against $t\bar{t}V$ .	153
159	6.9	Correlation matrices for the input variables in the TMVA.	154
160	6.10	MVA classifiers performance.	154
161	6.11	Additional discriminating variables distributions.	156

# <sup>162</sup> List of Tables

163	2.1	Fermions of the SM. . . . .	5
164	2.2	Fermion masses. . . . .	6
165	2.3	Lepton properties. . . . .	8
166	2.4	Quark properties. . . . .	9
167	2.5	Fermion weak isospin and weak hypercharge multiplets. . . . .	11
168	2.6	Fundamental interactions features. . . . .	15
169	2.7	SM gauge bosons. . . . .	20
170	2.8	Higgs boson properties. . . . .	38
171	2.9	Predicted branching ratios for a SM Higgs boson with $m_H = 125 \text{ GeV}/c^2$ . . . . .	42
172	2.10	Predicted SM cross sections for $tH$ production at $\sqrt{s} = 13 \text{ TeV}$ . . . . .	44
173	2.11	Predicted enhancement of the $tHq$ and $tHW$ cross sections at LHC . . . . .	48
174	6.1	Signal samples and their cross section and branching fraction. . . . .	129
175	6.2	$\kappa_V$ and $\kappa_t$ combinations. . . . .	130
176	6.3	List of background samples used in this analysis (CMSSW 80X). . . . .	131
177	6.4	Leading-order $t\bar{t}W$ and $t\bar{t}Z$ samples used in the signal BDT training. . . . .	131
178	6.5	Table of high-level triggers that we consider in the analysis. . . . .	132
179	6.6	Trigger efficiency scale factors and associated uncertainties. . . . .	133
180	6.7	Effective areas, for electrons and muons. . . . .	139

181	6.8 Requirements on each of the three muon selections. . . . .	142
182	6.9 Criteria for each of the three electron selections. . . . .	142
183	6.10 MVA input discriminating variables . . . . .	150
184	6.11 TMVA input variables ranking for BDTA_GRAD method . . . . .	155
185	6.12 TMVA configuration used in the BDT training. . . . .	155
186	6.13 ROC-integral for all the testing cases. . . . .	157

<sup>187</sup> Chapter 1

<sup>188</sup> INTRODUCTION

<sup>189</sup> **Chapter 2**

<sup>190</sup> **Theoretical approach**

<sup>191</sup> **2.1 Introduction**

<sup>192</sup> The physical description of the universe is a challenge that physicists have faced by  
<sup>193</sup> making theories that refine existing principles and proposing new ones in an attempt  
<sup>194</sup> to embrace emerging facts and phenomena.

<sup>195</sup> At the end of 1940s Julian Schwinger [1] and Richard P. Feynman [2], based on  
<sup>196</sup> the work of Sin-Itiro Tomonaga [3], developed an electromagnetic theory consistent  
<sup>197</sup> with special relativity and quantum mechanics that describes how matter and light  
<sup>198</sup> interact; the so-called “quantum eletrodynamics” (QED) was born.

<sup>199</sup> QED has become the guide in the development of theories that describe the uni-  
<sup>200</sup> verse. It was the first example of a quantum field theory (QFT), which is the theore-  
<sup>201</sup> tical framework for building quantum mechanical models that describes particles and  
<sup>202</sup> their interactions. QFT is composed of a set of mathematical tools that combines  
<sup>203</sup> classical fields, special relativity and quantum mechanics, while keeping the quantum  
<sup>204</sup> point particles and locality ideas.

<sup>205</sup> This chapter gives an overview of the standard model of particle physics, starting

206 with a description of the particles and interactions that compose it, followed by a  
 207 description of the electroweak interaction, the Higgs boson and the associated pro-  
 208 duction of Higgs boson and a single top quark ( $tH$ ). The description contained in  
 209 this chapter is based on References [4–6].

## 210 2.2 Standard model of particle physics

211 Particle physics at the fundamental level is modeled in terms of a collection of in-  
 212 teracting particles and fields in a theory known as the “standard model of particle  
 213 physics (SM)”. The full picture of the SM is composed of three fields<sup>1</sup> whose excita-  
 214 tions are interpreted as particles called mediators or force-carriers, a set of fields whose  
 215 excitations are interpreted as elementary particles interacting through the exchange  
 216 of those mediators, and a field that gives the mass to elementary particles. Figure  
 217 2.1 shows the scheme of the SM particles’ organization. In addition, for each of the  
 218 particles in the scheme there exists an antiparticle with the same mass and opposite  
 219 quantum numbers. The existence of antiparticles is a prediction of the relativistic  
 220 quantum mechanics from the solution of the dirac equation for which a negative en-  
 221 ergy solution is also possible. In some cases a particle is its own anti-particle, like  
 222 photon or Higgs boson.

223 The mathematical formulation of the SM is based on group theory and the use of  
 224 Noether’s theorem [8] which states that for a physical system modeled by a Lagrangian  
 225 that is invariant under a group of transformations a conservation law is expected. For  
 226 instance, a system described by a time-independent Lagrangian is invariant (symmet-  
 227 ric) under time changes (transformations) with the total energy conservation law as

---

<sup>1</sup> The formal and complete treatment of the SM is out of the scope of this document, however a plenty of textbooks describing it at several levels are available in the literature. The treatment in References [5, 6] is quite comprehensive and detailed. Note that gravitational field is not included in the standard model formulation

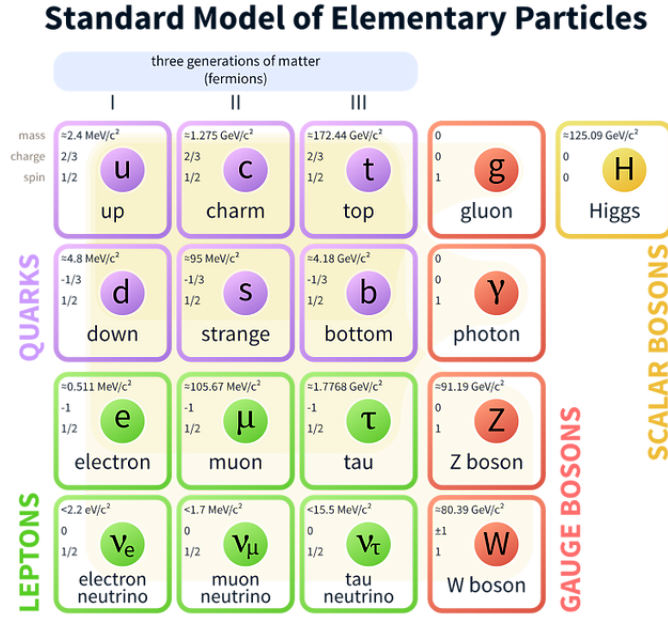


**Figure 2.1:** Schematic representation of the Standard Model of particle physics. The SM is a theoretical model intended to describe three of the four fundamental forces of the universe in terms of a set of particles and their interactions. [7].

228 the expected conservation law. In QED, the charge operator ( $Q$ ) is the generator of  
 229 the  $U(1)$  symmetry which according to the Noether's theorem means that there is a  
 230 conserved quantity; this conserved quantity is the electric charge and thus the law  
 231 conservation of electric charge is established.

232 In the SM, the symmetry group  $SU(3)_C \otimes SU(2)_L \otimes U(1)_Y$  describes three of the  
 233 four fundamental interactions in nature (see Section 2.2.2): strong interaction (SI),  
 234 weak interaction (WI) and electromagnetic interactions (EI) in terms of symmetries  
 235 associated to physical quantities:

- 236     • Strong:  $SU(3)_C$  associated to color charge
- 237     • Weak:  $SU(2)_L$  associated to weak isospin and chirality
- 238     • Electromagnetic:  $U(1)_Y$  associated to weak hypercharge and electric charge

239 It will be shown that the electromagnetic and weak interactions are combined in  
 240 the so-called electroweak interaction where chirality, hypercharge, weak isospin and  
 241 electric charge are the central concepts.

242 **2.2.1 Fermions**

243 The basic constituents of the ordinary matter at the lowest level, which form the set  
 244 of elementary particles in the SM formulation, are quarks and leptons. All of them  
 245 have spin 1/2, therefore they are classified as fermions since they obey Fermi-Dirac  
 246 statistics. There are six “flavors” of quarks and three of leptons organized in three  
 247 generations, or families, as shown in Table 2.1.

248

		Generation		
		1st	2nd	3rd
Leptons	Charged	Electron (e)	Moun( $\mu$ )	Tau ( $\tau$ )
	Neutral	Electron neutrino ( $\nu_e$ )	Muon neutrino ( $\nu_\mu$ )	Tau neutrino ( $\nu_\tau$ )
Quarks	Up-type	Up (u)	Charm (c)	Top (t)
	Down-type	Down (d)	Strange (s)	Bottom (b)

**Table 2.1:** Fermions of the SM. There are six flavors of quarks and three of leptons, organized in three generations, or families, composed of two pairs of closely related particles. The close relationship is motivated by the fact that each pair of particles is a member of an  $SU(2)_L$  doublet that has an associated invariance under isospin transformations. WI between leptons is limited to the members of the same generation; WI between quarks is not limited but greatly favored, to same generation members.

249

250 There is a mass hierarchy between generations (see Table 2.2), where the higher  
 251 generation particles decays to the lower one, which can explain why the ordinary  
 252 matter is made of particles from the first generation. In the SM, neutrinos are modeled  
 253 as massless particles so they are not subject to this mass hierarchy; however, today it  
 254 is known that neutrinos are massive so the hierarchy could be restated. The reason

255 behind this mass hierarchy is one of the most important open questions in particle  
 256 physics, and it becomes more puzzling when noticing that the mass difference between  
 257 first and second generation fermions is small compared to the mass difference with  
 258 respect to the third generation.

Lepton	Mass (MeV/c <sup>2</sup> )	Quark	Mass (MeV/c <sup>2</sup> )
e	0.51	u	2.2
$\mu$	105.65	c	$1.28 \times 10^3$
$\tau$	1776.86	t	$173.1 \times 10^3$
$\nu_e$	Unknown	d	4.7
$\nu_\mu$	Unknown	s	96
$\nu_\tau$	Unknown	b	$4.18 \times 10^3$

**Table 2.2:** Fermion masses [9]. Generations differ by mass in a way that has been interpreted as a masss hierarchy. Approximate values with no uncertainties are used, for comparison purpose.

259

260 Usually, the second and third generation fermions are produced in high energy  
 261 processes, like the ones recreated in particle accelerators.

### 262 2.2.1.1 Leptons

263 A lepton is an elementary particle that is not subject to the SI. As seen in Table 2.1,  
 264 there are two types of leptons, the charged ones (electron, muon and tau) and the  
 265 neutral ones (the three neutrinos). The electric charge (Q) is the property that gives  
 266 leptons the ability to participate in the EI. From the classical point of view, Q plays  
 267 a central role determining, among others, the strength of the electric field through  
 268 which the electromagnetic force is exerted. It is clear that neutrinos are not affected  
 269 by EI because they don't carry electric charge.

270 Another feature of the leptons that is fundamental in the mathematical description  
 271 of the SM is the chirality, which is closely related to spin and helicity. Helicity

272 defines the handedness of a particle by relating its spin and momentum such that  
 273 if they are parallel then the particle is right-handed; if spin and momentum are  
 274 antiparallel the particle is said to be left-handed. The study of parity conservation  
 275 (or violation) in  $\beta$ -decay has shown that only left-handed electrons/neutrinos or right-  
 276 handed positrons/anti-neutrinos are created [10]; the inclusion of that feature in the  
 277 theory was achieved by using projection operators for helicity, however, helicity is  
 278 frame dependent for massive particles which makes it not Lorentz invariant and then  
 279 another related attribute has to be used: *chirality*.

280 Chirality is a purely quantum attribute which makes it not so easy to describe in  
 281 graphical terms but it defines how the wave function of a particle transforms under  
 282 certain rotations. As with helicity, there are two chiral states, left-handed chiral (L)  
 283 and right-handed chiral (R). In the highly relativistic limit where  $E \approx p \gg m$  helicity  
 284 and chirality converge, becoming exactly the same for massless particles.

285 In the following, when referring to left-handed (right-handed) it will mean left-  
 286 handed chiral (right-handed chiral). The fundamental fact about chirality is that  
 287 while EI and SI are not sensitive to chirality, in WI left-handed and right-handed  
 288 fermions are treated asymmetrically, such that only left-handed fermions and right-  
 289 handed anti-fermions are allowed to couple to WI mediators, which is a violation of  
 290 parity. The way to translate this statement in a formal mathematical formulation is  
 291 based on the isospin symmetry group  $SU(2)_L$ .

292 Each generation of leptons is seen as a weak isospin doublet.<sup>2</sup> The left-handed  
 293 charged lepton and its associated left-handed neutrino are arranged in doublets of  
 294 weak isospin  $T=1/2$  while their right-handed partners are singlets:

---

<sup>2</sup> The weak isospin is an analogy of the isospin symmetry in strong interaction where neutron and proton are affected equally by strong force but differ in their charge.

$$\begin{pmatrix} \nu_l \\ l \end{pmatrix}_L, l_R := \begin{pmatrix} \nu_e \\ e \end{pmatrix}_L, \begin{pmatrix} \nu_\mu \\ \mu \end{pmatrix}_L, \begin{pmatrix} \nu_\tau \\ \tau \end{pmatrix}_L, e_R, \mu_R, \tau_R, \nu_{eR}, \nu_{\mu R}, \nu_{\tau R} \quad (2.1)$$

295     The isospin third component refers to the eigenvalues of the weak isospin operator  
 296    which for doublets is  $T_3 = \pm 1/2$ , while for singlets it is  $T_3 = 0$ . The physical meaning  
 297    of this doublet-singlet arrangement falls in that the WI couples the two particles in  
 298    the doublet by exchanging the interaction mediator while the singlet member is not  
 299    involved in WI. The main properties of the leptons are summarized in Table 2.3.

300       Altough all three flavor neutrinos have been observed, their masses remain un-  
 301    known and only some estimations have been made [11]. The main reason is that  
 302    the flavor eigenstates are not the same as the mass eigenstates which implies that  
 303    when a neutrino is created its mass state is a linear combination of the three mass  
 304    eigenstates and experiments can only probe the squared difference of the masses. The  
 305    Pontecorvo-Maki-Nakagawa-Sakata (PMNS) mixing matrix encodes the relationship  
 306    between flavor and mass eigenstates.

Lepton	Q(e)	$T_3$	$L_e$	$L_\mu$	$L_\tau$	Lifetime (s)
Electron (e)	-1	-1/2	1	0	0	Stable
Electron neutrino( $\nu_e$ )	0	1/2	1	0	0	Unknown
Muon ( $\mu$ )	-1	-1/2	0	1	0	$2.19 \times 10^{-6}$
Muon neutrino ( $\nu_\mu$ )	0	1/2	0	1	0	Unknown
Tau ( $\tau$ )	-1	-1/2	0	0	1	$290.3 \times 10^{-15}$
Tau neutrino ( $\nu_\tau$ )	0	1/2	0	0	1	Unknown

**Table 2.3:** Lepton properties [9]. Q: electric charge,  $T_3$ : weak isospin. Only left-handed leptons and right-handed anti-leptons participate in the WI. Anti-particles with inverted  $T_3$ , Q and lepton number complete the leptons set but are not listed. Right-handed leptons and left-handed anti-leptons, neither listed, form weak isospin singlets with  $T_3 = 0$  and do not take part in the weak interaction.

308    **2.2.1.2 Quarks**

309    Quarks are the basic constituents of protons and neutrons. The way quarks join to  
 310   form bound states, called “hadrons”, is through the SI. Quarks are affected by all the  
 311   fundamental interactions which means that they carry all the four types of charges:  
 312   color, electric charge, weak isospin and mass.

Flavor	$Q(e)$	$I_3$	$T_3$	B	C	S	T	$B'$	Y	Color
Up (u)	2/3	1/2	1/2	1/3	0	0	0	0	1/3	r,b,g
Charm (c)	2/3	0	1/2	1/3	1	0	0	0	4/3	r,b,g
Top(t)	2/3	0	1/2	1/3	0	0	1	0	4/3	r,b,g
Down(d)	-1/3	-1/2	-1/2	1/3	0	0	0	0	1/3	r,b,g
Strange(s)	-1/3	0	-1/2	1/3	0	-1	0	0	-2/3	r,b,g
Bottom(b)	-1/3	0	-1/2	1/3	0	0	0	-1	-2/3	r,b,g

**Table 2.4:** Quark properties [9]. Q: electric charge,  $I_3$ : isospin,  $T_3$ : weak isospin, B: baryon number, C: charmness, S: strangeness, T: topness,  $B'$ : bottomness, Y: hypercharge. Anti-quarks posses the same mass and spin as quarks but all charges (color, flavor numbers) have opposite sign.

313

314    Table 2.4 summarizes the features of quarks, among which the most remarkable  
 315   is their fractional electric charge. Note that fractional charge is not a problem, given  
 316   that quarks are not found isolated, but serves to explain how composed particles are  
 317   formed out of two or more valence quarks<sup>3</sup>.

318    Color charge is responsible for the SI between quarks and is the symmetry ( $SU(3)_C$ )  
 319   that defines the formalism to describe SI. There are three colors: red (r), blue (b)  
 320   and green (g) and their corresponding three anti-colors; thus each quark carries one  
 321   color unit while anti-quarks carries one anti-color unit. As explained in Section 2.2.2,  
 322   quarks are not allowed to be isolated due to the color confinement effect, hence, their  
 323   features have been studied indirectly by observing their bound states created when

---

<sup>3</sup> Hadrons can contain an indefinite number of virtual quarks and gluons, known as the quark and gluon sea, but only the valence quarks determine hadrons’ quantum numbers.

324       • one quark with a color charge is attracted by an anti-quark with the correspond-  
 325       ing anti-color charge forming a colorless particle called a “meson.”

326       • three quarks (anti-quarks) with different color (anti-color) charges are attracted  
 327       among them forming a colorless particle called a “baryon (anti-baryon).”

328       In practice, when a quark is left alone isolated a process called “hadronization”  
 329       occurs where the quark emits gluons (see Section 2.2.3) which eventually will generate  
 330       new quark-antiquark pairs and so on; those quarks will recombine to form hadrons  
 331       that will decay into leptons. This proliferation of particles looks like a “jet” com-  
 332       ing from the isolated quark. More details about the hadronization process and jet  
 333       structure will be given in chapter4.

334       In the first version of the quark model (1964), M. Gell-Mann [12] and G. Zweig  
 335       [13, 14] developed a consistent way to classify hadrons according to their properties.  
 336       Only three quarks (u, d, s) were involved in a scheme in which all baryons have baryon  
 337       number  $B=1$  and therefore quarks have  $B=1/3$ ; non-baryons have  $B=0$ . Baryon  
 338       number is conserved in SI and EI which means that single quarks cannot be created  
 339       but in pairs  $q - \bar{q}$ .

340       The scheme organizes baryons in a two-dimensional space ( $I_3$  - Y); Y (hyper-  
 341       charge) and  $I_3$  (isospin) are quantum numbers related by the Gell-Mann-Nishijima  
 342       formula [15, 16]:

$$Q = I_3 + \frac{Y}{2} \quad (2.2)$$

343       where  $Y = B + S + C + T + B'$  are the quantum numbers listed in Table 2.4.

344       There are six quark flavors organized in three generations (see Table 2.1) fol-  
 345       lowing a mass hierarchy which, again, implies that higher generations decay to first  
 346       generation quarks.

	Quarks			$T_3$	$Y_W$	Leptons			$T_3$	$Y_W$
Doublets	$(\frac{u}{d'})_L$	$(\frac{c}{s'})_L$	$(\frac{t}{b'})_L$	$(\frac{1/2}{-1/2})$	$1/3$	$(\nu_e)_L$	$(\nu_\mu)_L$	$(\nu_\tau)_L$	$(\frac{1/2}{-1/2})$	-1
Singlets	$u_R$	$c_R$	$t_R$	0	$4/3$	$\nu_{eR}$	$\nu_{\mu R}$	$\nu_{\tau R}$		
	$d'_R$	$s'_R$	$b'_R$	0	$-2/3$	$e_R$	$\mu_R$	$\tau_R$	0	-2

**Table 2.5:** Fermion weak isospin and weak hypercharge multiplets. Weak hypercharge is calculated through the Gell-Mann-Nishijima formula 2.2 but using the weak isospin and charge for quarks.

347

Isospin doublets of quarks are also defined (see Table 2.5), and same as for neutrinos, the WI eigenstates are not the same as the mass eigenstates which means that members of different quark generations are connected by the WI mediator; thus, up-type quarks are coupled not to down-type quarks (the mass eigenstates) directly but to a superposition of down-type quarks ( $q'_d$ ; *the weak eigenstates*) via WI according to:

354

$$q'_d = V_{CKM} q_d$$

$$\begin{pmatrix} d' \\ s' \\ b' \end{pmatrix} = \begin{pmatrix} V_{ud} & V_{us} & V_{ub} \\ V_{cd} & V_{cs} & V_{cb} \\ V_{td} & V_{ts} & V_{tb} \end{pmatrix} \begin{pmatrix} d \\ s \\ b \end{pmatrix} \quad (2.3)$$

where  $V_{CKM}$  is known as Cabibbo-Kobayashi-Maskawa (CKM) mixing matrix [17,18] given by

$$\begin{pmatrix} |V_{ud}| & |V_{us}| & |V_{ub}| \\ |V_{cd}| & |V_{cs}| & |V_{cb}| \\ |V_{td}| & |V_{ts}| & |V_{tb}| \end{pmatrix} = \begin{pmatrix} 0.97427 \pm 0.00015 & 0.22534 \pm 0.00065 & 0.00351^{+0.00015}_{-0.00014} \\ 0.22520 \pm 0.00065 & 0.97344 \pm 0.00016 & 0.0412^{+0.0011}_{-0.0005} \\ 0.00867^{+0.00029}_{-0.00031} & 0.0404^{+0.0011}_{-0.0005} & 0.999146^{+0.000021}_{-0.000046} \end{pmatrix}. \quad (2.4)$$

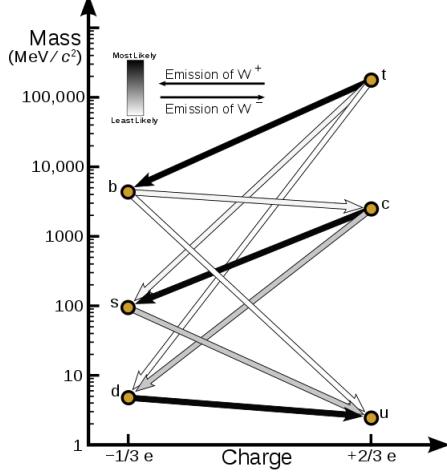


**Figure 2.2:** Transformations between quarks through the exchange of a WI. Higher generations quarks decay to first generation quarks by emitting a W boson. The arrow color indicates the likelihood of the transition according to the grey scale in the top left side which represent the CKM matrix parameters [19].

357        The weak decays of quarks are represented in the diagram of Figure 2.2; again  
 358        the CKM matrix plays a central role since it contains the probabilities for the differ-  
 359        ent quark decay channels, in particular, note that quark decays are greatly favored  
 360        between generation members.

361

362        CKM matrix is a  $3 \times 3$  unitary matrix parametrized by three mixing angles and  
 363        the *CP-mixing phase*; the latter is the parameter responsible for the Charge-Parity  
 364        symmetry violation (CP-violation) in the SM. The fact that the top quark decays  
 365        almost all the time to a bottom quark is exploited in this thesis when making the  
 366        selection of the signal events by requiring the presence of a jet tagged as a jet coming  
 367        from a  $b$  quark in the final state. The effect of the *CP-mixing phase* on the cross section  
 368        of associated production of Higgs boson and a single top process is also explored in  
 369        this thesis.

370 2.2.2 Fundamental interactions

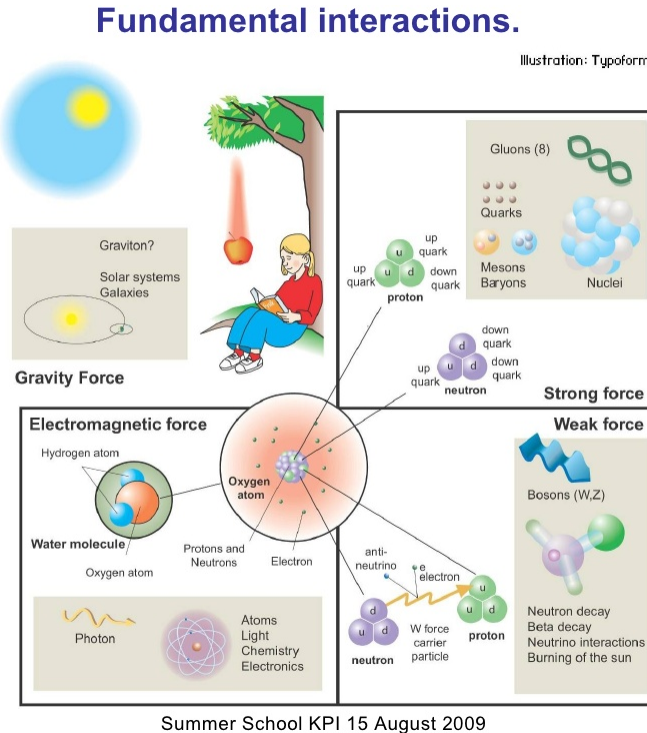


**Figure 2.3:** Fundamental interactions in nature. Despite the many manifestations of forces in nature, we can track all of them back to one of the fundamental interactions. The most common forces are gravity and electromagnetic given that all of us are subject and experience them in everyday life.

371 Even though there are many manifestations of force in nature, like the ones rep-  
 372 resented in Figure 2.3, we can classify all of them into one of four fundamental inter-  
 373 actions:

- 374 • *Electromagnetic interaction (EI)* affects particles that are “electrically charged,”  
 375 like electrons and protons. It is described by QED combining quantum mechan-  
 376 ics, special relativity and electromagnetism in order to explain how particles  
 377 with electric charge interact through the exchange of photons, therefore, one  
 378 says that “Electromagnetic Force” is mediated by “photons”. Figure 2.4a. shows

379 a graphical representation, known as “feynman diagram”, of electron-electron  
 380 scattering.

- 381 • *Strong interaction (SI)* described by Quantum Chromodynamics (QCD). Hadrons  
 382 like proton and neutron have internal structure given that they are composed  
 383 of two or more valence quarks<sup>4</sup>. Quarks have fractional electric charge which  
 384 means that they are subject to electromagnetic interaction and in the case of the  
 385 proton they should break apart due to electrostatic repulsion; however, quarks  
 386 are held together inside the hadrons against their electrostatic repulsion by the  
 387 “Strong Force” through the exchange of “gluons.” The analog to the electric  
 388 charge is the “color charge”. Electrons and photons are elementary particles as  
 389 quarks but they don’t carry color charge, therefore they are not subject to SI.  
 390 The feynman diagram for gluon exchange between quarks is shown in Figure  
 391 2.4b.

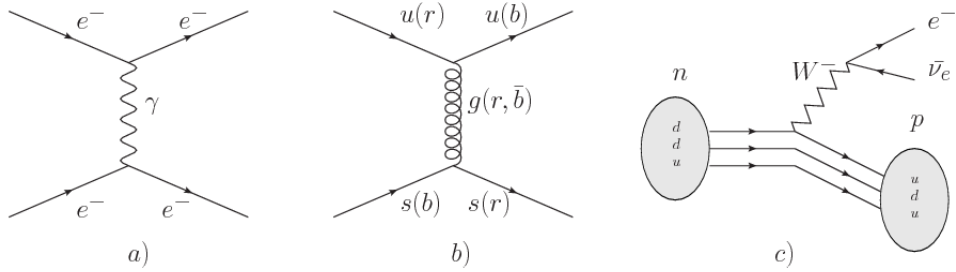


**Figure 2.4:** Feynman diagrams representing the interactions in SM; a) EI: e-e scattering; b) SI: gluon exchange between quarks ; c) WI:  $\beta$ -decay

- 392 • *Weak interaction (WI)* described by the weak theory (WT), is responsible, for  
 393 instance, for the radioactive decay in atoms and proton-proton (pp) fusion  
 394 within the sun. Quarks and leptons are the particles affected by the weak  
 395 interaction; they possess a property called “flavor charge” (see 2.2.1) which can  
 396 be changed by emitting or absorbing one weak force mediator. There are three

<sup>4</sup> particles made of four and five quarks are exotic states not so common.

397 mediators of the “weak force” known as “Z” boson in the case of electrically  
 398 neutral changes and “ $W^\pm$ ” bosons in the case of electrically charged changes.  
 399 The “weak isospin” is the WI analog to electric charge in EI, and color charge  
 400 in SI, and defines how quarks and leptons are affected by the weak force. Figure  
 401 2.4c. shows the feynman diagram of  $\beta$ -decay where a newtron (n) is transformed  
 402 in a proton (p) by emmiting a  $W^-$  particle. Since this thesis is in the frame  
 403 of the electroweak interaction, a more detailed description of it will be given in  
 404 Section 2.3

405 • *Gravitational interaction (GI)* described by General Theory of Relativity (GR).  
 406 It is responsible for the structure of galaxies and black holes as well as the  
 407 expansion of the universe. As a classical theory, in the sense that it can be for-  
 408 mulated without even appeal to the concept of quantization, it implies that the  
 409 spacetime is a continuum and predictions can be made without limitation to the  
 410 precision of the measurement tools. The latter represent a direct contradiction  
 411 of the quantum mechanics principles. Gravity is deterministic while quantum  
 412 mechanics is probabilistic; despite that, efforts to develop a quantum theory of  
 413 gravity have predicted the “graviton” as mediator of the Gravitational force<sup>5</sup>.

Interaction	Acts on	Relative strength	Range (m)	Mediators
Electromagnetic (QED)	Electrically charged particles	$10^{-2}$	Infinite	Photon
Strong (QCD)	Quarks and gluons	1	$10^{-15}$	Gluon
Weak (WI)	Leptons and quarks	$10^{-6}$	$10^{-18}$	$W^\pm$ , Z
Gravitational (GI)	Massive particles	$10^{-39}$	Infinite	Graviton

**Table 2.6:** Fundamental interactions features [20].

414

---

<sup>5</sup> Actually a wide variety of theories have been developed in an attempt to describe gravity; some famous examples are string theory and supergravity.

415       Table 2.6 summarizes the main features of the fundamental interactions. The rel-  
 416 ative strength of the fundamental forces reveals the meaning of strong and weak; in  
 417 a context where the relative strength of the SI is 1, the EI is about hundred times  
 418 weaker and WI is about million times weaker than the SI. A good description on  
 419 how the relative strength and range of the fundamental interactions are calculated  
 420 can be found in References [20,21]. In the everyday life, only EI and GI are explicitly  
 421 experienced due to the range of these interactions; i.e., at the human scale distances  
 422 only EI and GI have appreciable effects, in contrast to SI which at distances greater  
 423 than  $10^{-15}$ m become negligible.

424

425       QED was built successfully on the basis of the classical electrodynamics theory  
 426 (CED) of Maxwell and Lorentz, following theoretical and experimental requirements  
 427 imposed by

- 428       • lorentz invariance: independence on the reference frame.
- 429       • locality: interacting fields are evaluated at the same space-time point to avoid  
 430           action at a distance.
- 431       • renormalizability: physical predictions are finite and well defined
- 432       • particle spectrum, symmetries and conservation laws already known must emerge  
 433           from the theory.
- 434       • gauge invariance.

435       The gauge invariance requirement reflects the fact that the fundamental fields  
 436 cannot be directly measured but associated fields which are the observables. Elec-  
 437 tric (“E”) and magnetic (“B”) fields in CED are associated with the electric scalar

438 potential “V” and the vector potential “A”. In particular,  $\mathbf{E}$  can be obtained by  
 439 measuring the change in the space of the scalar potential ( $\Delta V$ ); however, two scalar  
 440 potentials differing by a constant “f” correspond to the same electric field. The same  
 441 happens in the case of the vector potential “A”; thus, different configurations of the  
 442 associated fields result in the same set of values of the observables. The freedom in  
 443 choosing one particular configuration is known as “gauge freedom”; the transformation  
 444 law connecting two configurations is known as “gauge transformation” and the  
 445 fact that the observables are not affected by a gauge transformation is called “gauge  
 446 invariance”.

447

448 When the gauge transformation:

$$\begin{aligned} \mathbf{A} &\rightarrow \mathbf{A} - \Delta f \\ V &\rightarrow V - \frac{\partial f}{\partial t} \end{aligned} \quad (2.5)$$

449 is applied to Maxwell equations, they are still satisfied and the fields remain invariant.  
 450 Thus, CED is invariant under gauge transformations and is called a “gauge theory”.  
 451 The set of all gauge transformations form the “symmetry group” of the theory, which  
 452 according to the group theory, has a set of “group generators”. The number of group  
 453 generators determine the number of “gauge fields” of the theory.

454

455 As mentioned in the first lines of Section 2.2, QED has one symmetry group ( $U(1)$ )  
 456 with one group generator (the  $Q$  operator) and one gauge field (the electromagnetic  
 457 field  $A^\mu$ ). In CED there is not a clear definition, beyond the historical convention, of  
 458 which fields are the fundamental and which are the associated, but in QED it is clear

459 that the fundamental field is  $A^\mu$ . When a gauge theory is quantized, the gauge field  
460 is quantized and its quanta is called “gauge boson”. The word boson characterizes  
461 particles with integer spin which obvey Bose-einstein statistics.

462

463 As will be detailed in Section 2.3, interactions between particles in a system can  
464 be obtained by considering first the Lagrangian density of free particles in the sys-  
465 tem, which of course is incomplete because the interaction terms have been left out,  
466 and demanding global phase transformation invariance. Global phase transformation  
467 invariance means that a gauge transformation is performed identically to every point  
468 in the space<sup>6</sup> and the Lagrangian remains invariant. Then, the global transformation  
469 is promoted to a local phase transformation (this time the gauge transformation de-  
470 pends on the position in space) and again invariance is required.

471

472 Due to the space dependence of the local tranformation, the Lagrangian density is  
473 not invariant anymore. In order to restate the gauge invariance, the gauge covariant  
474 derivative is introduced in the Lagrangian and with it the gauge field responsible for  
475 the interaction between particles in the system. The new Lagrangian density is gauge  
476 invariant, includes the interaction terms needed to account for the interactions and  
477 provides a way to explain the interaction between particles through the exchange of  
478 the gauge boson.

479 This recipe was used to build QED and the theories that aim to explain the  
480 fundamental interactions.

---

<sup>6</sup> Here space corresponds to the 4-dimensional space i.e. space-time.

481 **2.2.3 Gauge bosons**

482 The importance of the gauge bosons comes from the fact that they are the force  
 483 mediators or force carriers. The features of the gauge bosons reflect those of the fields  
 484 they represent and they are extracted from the Lagrangian density used to describe  
 485 the interactions. In Section 2.3, it will be shown how the gauge bosons of the EI and  
 486 WI emerge from the electroweak Lagrangian. The SI gauge bosons features are also  
 487 extracted from the SI Lagrangian but it is not detailed in this document. The main  
 488 features of the SM gauge bosons will be briefly presented below and summarized in  
 489 Table 2.7.

490 • **Photon.** EI occurs when the photon couples to (is exchanged between) particles  
 491 carrying electric charge; however, the photon itself does not carry electric charge,  
 492 therefore, there is no coupling between photons. Given that the photon is  
 493 massless the EI is of infinite range, i.e., electrically charged particles interact  
 494 even if they are located far away one from each other; this also implies that  
 495 photons always move with the speed of light.

496 • **Gluon.** SI is mediated by gluons which, same as photons, are massless. They  
 497 carry one unit of color charge and one unit of anticolor charge which means that  
 498 gluons couple to other gluons. As a result, the range of the SI is not infinite  
 499 but very short due to the attraction between gluons, giving rise to the “color  
 500 confinement” which explains why color charged particles cannot be isolated but  
 501 live within composited particles, like quarks inside protons.

502 • **W, Z.** The WI mediators,  $W^\pm$  and Z, are massive which explains their short-  
 503 range. Given that the WI is the only interaction that can change the flavor  
 504 of the interacting particles, the W boson is the responsible for the nuclear

505 transmutation where a neutron is converted in a proton or vice versa with the  
 506 involvement of an electron and a neutrino (see Figure 2.4c). The Z boson is the  
 507 responsible of the neutral weak processes like neutrino elastic scattering where  
 508 no electric charge but momentum transference is involved. WI gauge bosons  
 509 carry isospin charge which makes possible the interaction between them.

Interaction	Mediator	Electric charge (e)	Color charge	Weak Isospin	mass (GeV/c <sup>2</sup> )
Electromagnetic	Photon ( $\gamma$ )	0	No	0	0
Strong	Gluon (g)	0	Yes -octet	No	0
Weak	$W^\pm$	$\pm 1$	No	$\pm 1$	$80.385 \pm 0.015$
	Z	0	No	0	$91.188 \pm 0.002$

**Table 2.7:** SM gauge bosons main features [9].

510

## 511 **2.3 Electroweak unification and the Higgs**

512 **mechanism**

513 Physicists dream of building a theory that contains all the interactions in one single  
 514 interaction, i.e., showing that at some scale in energy all the four fundamental in-  
 515 teractions are unified and only one interaction emerges in a “Theory of everything”.  
 516 The first sign of the feasibility of such unification comes from success in the con-  
 517 struction of the CED. Einstein spent years trying to reach that dream, which by  
 518 1920 only involved electromagnetism and gravity, with no success; however, a new  
 519 partial unification was achieved in the 1960’s, when S.Glashow [22], A.Salam [23] and  
 520 S.Weinberg [24] independently proposed that electromagnetic and weak interactions  
 521 are two manifestations of a more general interaction called “electroweak interaction  
 522 (EWT)”. Both, QCD and EWT, were developed in parallel and following the useful

523 prescription provided by QED and the gauge invariance principles.

524

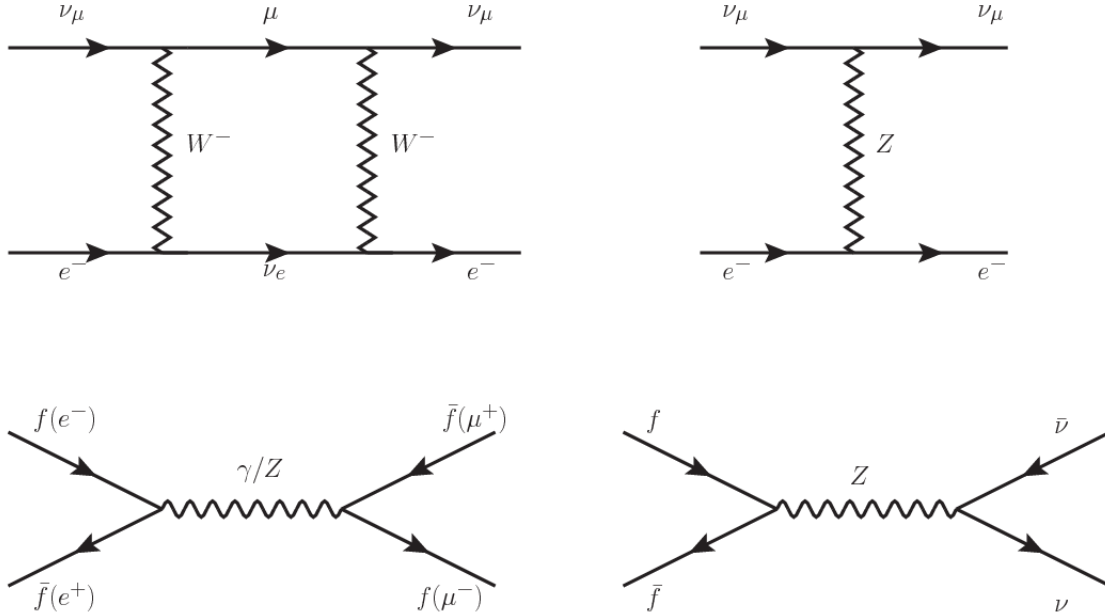


**Figure 2.5:** Top:  $\nu_\mu - e^-$  scattering going through charged currents (left) and neutral currents (right). Bottom: neutral current processes for charged fermions (left) and involving neutrinos (right). While neutral current processes involving only charged fermions can proceed through EI or WI, those involving neutrinos can only proceed via WI.

525 The theory of weak interactions was capable of explaining the  $\beta$ -decay and in  
 526 general the processes mediated by  $W^\pm$  bosons. However, there were some processes  
 527 like the “ $\nu_\mu - e$  scattering” which would require the exchange of two W bosons (see  
 528 Figure 2.5 top diagrams) giving rise to divergent loop integrals and then non finite  
 529 predictions. By including neutral currents involving fermions via the exchange of neu-  
 530 tral bosons Z, those divergences are compensated and the predictions become realistic.

531

532 Neutral weak interaction vertices conserve flavor in the same way as the electro-  
 533 magnetic vertices do, but additionally, the Z boson can couple to neutrinos which  
 534 implies that processes involving charged fermions can proceed through EI or WI but

535 processes involving neutrinos can proceed only through WI.

536

537 The prescription to build a gauge theory of the WI consists of proposing a free  
 538 field Lagrangian density that includes the particles involved; next, by requesting  
 539 invariance under global phase transformations first and generalizing to local phase  
 540 transformations invariance later, the conserved currents are identified and interactions  
 541 are generated by introducing gauge fields. Given that the goal is to include the EI  
 542 and WI in a single theory, the group symmetry considered should be a combination of  
 543  $SU(2)_L$  and  $U(1)_{em}$ , however the latter cannot be used directly because the EI treats  
 544 left and right-handed particles indistinctly in contrast to the former. Fortunately, the  
 545 weak hypercharge, which is a combination of the weak isospin and the electric charge  
 546 (eqn 2.2) is suitable to be used since it is conserved by the EI and WI. Thus, the  
 547 symmetry group to be considered is

$$G \equiv SU(2)_L \otimes U(1)_Y \quad (2.6)$$

548 The following treatment applies to any of the fermion generations, but for sim-  
 549 plicity the first generation of leptons will be considered [5, 6, 25, 26].

550

551 Given the first generation of leptons

$$\psi_1 = \begin{pmatrix} \nu_e \\ e^- \end{pmatrix}_L, \quad \psi_2 = \nu_{eR}, \quad \psi_3 = e_R^- \quad (2.7)$$

552 the charged fermionic currents are given by

$$J_\mu \equiv J_\mu^+ = \bar{\nu}_{eL} \gamma_\mu e_L, \quad J_\mu^\dagger \equiv J_\mu^- = \bar{e}_L \gamma_\mu \nu_{eL} \quad (2.8)$$

553 and the free Lagrangian is given by

$$\mathcal{L}_0 = \sum_{j=1}^3 i\bar{\psi}_j(x)\gamma^\mu\partial_\mu\psi_j(x). \quad (2.9)$$

554 Mass terms are included directly in the QED and QCD free Lagrangians since  
 555 they preserve the invariance under the symmetry transformations involved which  
 556 treat left-handed and right-handed similarly, however mass terms of the form

$$m_W^2 W_\mu^\dagger(x)W^\mu(x) + \frac{1}{2}m_Z^2 Z_\mu(x)Z^\mu(x) - m_e\bar{\psi}_e(x)\psi_e(x) \quad (2.10)$$

557 which represent the mass of  $W^\pm$ , Z and electrons, are not invariant under G trans-  
 558 formations, therefore the gauge fields described by the EWI are in principle massless.

559

560 Experiments have shown that the gauge fields are not massless; however, they  
 561 have to acquire mass through a mechanism compatible with the gauge invariance;  
 562 that mechanism is known as the “Higgs mechanism” and will be considered later in  
 563 this Section. The global transformations in the combined symmetry group G can be  
 564 written as

$$\begin{aligned} \psi_1(x) &\xrightarrow{G} \psi'_1(x) \equiv U_Y U_L \psi_1(x), \\ \psi_2(x) &\xrightarrow{G} \psi'_2(x) \equiv U_Y \psi_2(x), \\ \psi_3(x) &\xrightarrow{G} \psi'_3(x) \equiv U_Y \psi_3(x) \end{aligned} \quad (2.11)$$

565 where  $U_L$  represent the  $SU(2)_L$  transformation acting only on the weak isospin dou-  
 566 blet and  $U_Y$  represent the  $U(1)_Y$  transformation acting on all the weak isospin mul-

567 triplets. Explicitly

$$U_L \equiv \exp\left(i\frac{\sigma_i}{2}\alpha^i\right), \quad U_Y \equiv \exp(iy_i\beta) \quad (i = 1, 2, 3) \quad (2.12)$$

568 with  $\sigma_i$  the Pauli matrices and  $y_i$  the weak hypercharges. In order to promote the  
 569 transformations from global to local while keeping the invariance, it is required that  
 570  $\alpha^i = \alpha^i(x)$ ,  $\beta = \beta(x)$  and the replacement of the ordinary derivatives by the covariant  
 571 derivatives

$$\begin{aligned} D_\mu \psi_1(x) &\equiv \left[ \partial_\mu + ig\sigma_i W_\mu^i(x)/2 + ig'y_1 B_\mu(x) \right] \psi_1(x) \\ D_\mu \psi_2(x) &\equiv \left[ \partial_\mu + ig'y_2 B_\mu(x) \right] \psi_2(x) \\ D_\mu \psi_3(x) &\equiv \left[ \partial_\mu + ig'y_3 B_\mu(x) \right] \psi_3(x) \end{aligned} \quad (2.13)$$

572 introducing in this way four gauge fields,  $W_\mu^i(x)$  and  $B_\mu(x)$ , in the process. The  
 573 covariant derivatives (eqn 2.13) are required to transform in the same way as fermion  
 574 fields  $\psi_i(x)$  themselves, therefore, the gauge fields transform as:

$$\begin{aligned} B_\mu(x) &\xrightarrow{G} B'_\mu(x) \equiv B_\mu(x) - \frac{1}{g'} \partial_\mu \beta(x) \\ W_\mu^i(x) &\xrightarrow{G} W_\mu^{i\prime}(x) \equiv W_\mu^i(x) - \frac{i}{g} \partial_\mu \alpha_i(x) - \varepsilon_{ijk} \alpha_i(x) W_\mu^j(x). \end{aligned} \quad (2.14)$$

575 The G invariant version of the Lagrangian density 2.9 can be written as

$$\mathcal{L}_0 = \sum_{j=1}^3 i\bar{\psi}_j(x) \gamma^\mu D_\mu \psi_j(x) \quad (2.15)$$

576 where free massless fermion and gauge fields and fermion-gauge boson interactions

577 are included. The EWI Lagrangian density must additionally include kinetic terms  
 578 for the gauge fields ( $\mathcal{L}_G$ ) which are built from the field strengths, according to

$$B_{\mu\nu}(x) \equiv \partial_\mu B_\nu - \partial_\nu B_\mu \quad (2.16)$$

$$W_{\mu\nu}^i(x) \equiv \partial_\mu W_\nu^i(x) - \partial_\nu W_\mu^i(x) - g\varepsilon^{ijk}W_\mu^j W_\nu^k \quad (2.17)$$

579 the last term in eqn. 2.17 is added in order to hold the gauge invariance; therefore,

$$\mathcal{L}_G = -\frac{1}{4}B_{\mu\nu}(x)B^{\mu\nu}(x) - \frac{1}{4}W_{\mu\nu}^i(x)W_i^{\mu\nu}(x) \quad (2.18)$$

580 which contains not only the free gauge fields contributions, but also the gauge fields  
 581 self-interactions and interactions among them.

582

583 The three weak isospin conserved currents resulting from the  $SU(2)_L$  symmetry  
 584 are given by

$$J_\mu^i(x) = \frac{1}{2}\bar{\psi}_1(x)\gamma_\mu\sigma^i\psi_1(x) \quad (2.19)$$

585 while the weak hypercharge conserved current resulting from the  $U(1)_Y$  symmetry is  
 586 given by

$$J_\mu^Y = \sum_{j=1}^3 \bar{\psi}_j(x)\gamma_\mu y_j\psi_j(x) \quad (2.20)$$

587 In order to evaluate the electroweak interactions modeled by an isos triplet field  
 588  $W_\mu^i$  which couples to isospin currents  $J_\mu^i$  with strength  $g$  and additionally the singlet  
 589 field  $B_\mu$  which couples to the weak hypercharge current  $J_\mu^Y$  with strength  $g'/2$ . The  
 590 interaction Lagrangian density to be considered is

$$\mathcal{L}_I = -g J^{i\mu}(x) W_\mu^i(x) - \frac{g'}{2} J^{Y\mu}(x) B_\mu(x) \quad (2.21)$$

591 Note that the weak isospin currents are not the same as the charged fermionic  
 592 currents that were used to describe the WI (eqn 2.8), since the weak isospin eigenstates  
 593 are not the same as the mass eigenstates, but they are closely related

$$J_\mu = \frac{1}{2}(J_\mu^1 + iJ_\mu^2), \quad J_\mu^\dagger = \frac{1}{2}(J_\mu^1 - iJ_\mu^2). \quad (2.22)$$

594 The same happens with the gauge fields  $W_\mu^i$  which are related to the mass eigen-  
 595 states  $W^\pm$  by

$$W_\mu^+ = \frac{1}{\sqrt{2}}(W_\mu^1 - iW_\mu^2), \quad W_\mu^- = \frac{1}{\sqrt{2}}(W_\mu^1 + iW_\mu^2). \quad (2.23)$$

596 The fact that there are three weak isospin conserved currents is an indication that  
 597 in addition to the charged fermionic currents, which couple charged to neutral leptons,  
 598 there should be a neutral fermionic current that does not involve electric charge  
 599 exchange; therefore, it couples neutral fermions or fermions of the same electric charge.  
 600 The third weak isospin current contains a term that is similar to the electromagnetic  
 601 current ( $j_\mu^{em}$ ), indicating that there is a relation between them and resembling the  
 602 Gell-Mann-Nishijima formula 2.2 adapted to electroweak interactions

$$Q = T_3 + \frac{Y_W}{2}. \quad (2.24)$$

603 Just as  $Q$  generates the  $U(1)_{em}$  symmetry, the weak hypercharge generates the  
 604  $U(1)_Y$  symmetry as said before. It is possible to write the relationship in terms of  
 605 the currents as

$$j_\mu^{em} = J_\mu^3 + \frac{1}{2} J_\mu^Y. \quad (2.25)$$

606        The neutral gauge fields  $W_\mu^3$  and  $B_\mu$  cannot be directly identified with the  $Z$   
 607   and the photon fields since the photon interacts similarly with left and right-handed  
 608   fermions; however, they are related through a linear combination given by

$$\begin{aligned} A_\mu &= B_\mu \cos \theta_W + W_\mu^3 \sin \theta_W \\ Z_\mu &= -B_\mu \sin \theta_W + W_\mu^3 \cos \theta_W \end{aligned} \quad (2.26)$$

609   where  $\theta_W$  is known as the “Weinberg angle.” The interaction Lagrangian is now given  
 610   by

$$\mathcal{L}_I = -\frac{g}{\sqrt{2}}(J^\mu W_\mu^+ + J^{\mu\dagger} W_\mu^-) - \left(g \sin \theta_W J_\mu^3 + g' \cos \theta_W \frac{J_\mu^Y}{2}\right) A^\mu - \left(g \cos \theta_W J_\mu^3 - g' \sin \theta_W \frac{J_\mu^Y}{2}\right) Z^\mu \quad (2.27)$$

611   the first term is the weak charged current interaction, while the second term is the  
 612   electromagnetic interaction under the condition

$$g \sin \theta_W = g' \cos \theta_W = e, \quad \frac{g'}{g} = \tan \theta_W \quad (2.28)$$

613   contained in the eqn.2.25; the third term is the neutral weak current.

614

615   Note that the neutral fields transformation given by the eqn. 2.26 can be written  
 616   in terms of the coupling constants  $g$  and  $g'$  as:

$$A_\mu = \frac{g' W_\mu^3 + g B_\mu}{\sqrt{g^2 + g'^2}}, \quad Z_\mu = \frac{g W_\mu^3 - g' B_\mu}{\sqrt{g^2 + g'^2}} \quad (2.29)$$

617 So far, the Lagrangian density describing the non-massive EWI is:

$$\mathcal{L}_{nmEWI} = \mathcal{L}_0 + \mathcal{L}_G \quad (2.30)$$

618 where fermion and gauge fields have been considered massless because their regular  
 619 mass terms are manifestly non invariant under  $G$  transformations; therefore, masses  
 620 have to be generated in a gauge invariant way. The mechanism by which this goal is  
 621 achieved is known as the “Higgs mechanism” and is closely connected to the concept  
 622 of “spontaneous symmetry breaking.”

### 623 2.3.1 Spontaneous symmetry breaking (SSB)

624 Figure 2.6 left shows a steel nail (top) which is subject to an external force; the form  
 625 of the potential energy is also shown (bottom).

626

627 Before reaching the critical force value, the system has rotational symmetry with  
 628 respect to the nail axis; however, after the critical force value is reached the nail buckles (top right). The form of the potential energy (bottom right) changes, preserving  
 629 its rotational symmetry although its minima does not exhibit that rotational symme-  
 630 try any longer. Right before the nail buckles there is no indication of the direction the  
 631 nail will bend because any of the directions are equivalent, but once the nail bends,  
 632 choosing a direction, an arbitrary minimal energy state (ground state) is selected and  
 633 it does not share the system’s rotational symmetry. This mechanism for reaching an  
 634 asymmetric ground state is known as “*spontaneous symmetry breaking*”.

636 The lesson from this analysis is that the way to introduce the SSB mechanism  
 637 into a system is by adding the appropriate potential to it.

638

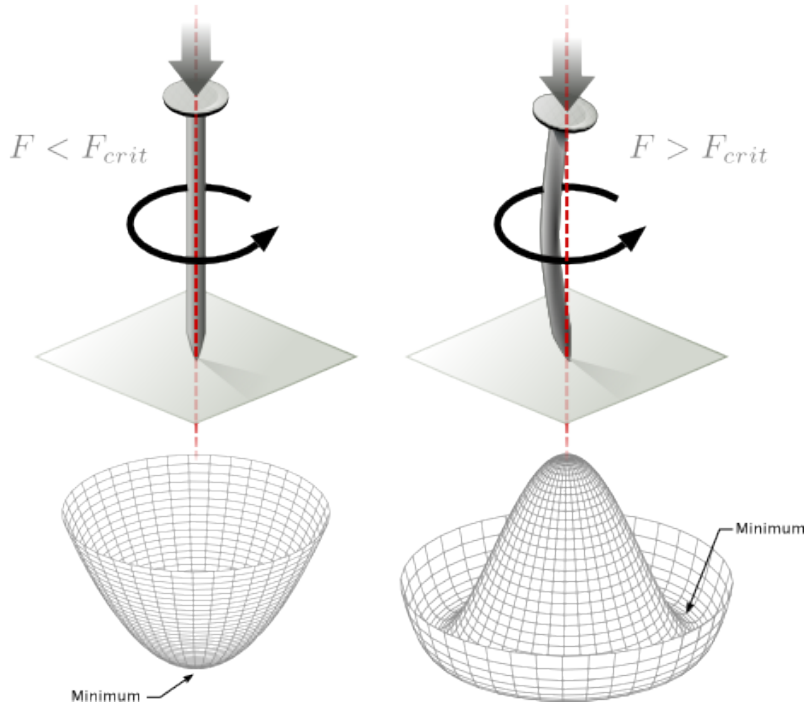


**Figure 2.6:** Spontaneous symmetry breaking mechanism. The steel nail, subject to an external force (top left), has rotational symmetry with respect to its axis. When the external force overcomes a critical value the nail buckles (top right) choosing a minimal energy state (ground state) and thus “*breaking spontaneously the rotational symmetry*”. The potential energy (bottom) changes but holds the rotational symmetry; however, an infinite number of asymmetric ground states are generated and circularly distributed in the bottom of the potential [27].

639        Figure 2.7 shows a plot of the potential  $V(\phi)$  in the case of a scalar field  $\phi$

$$V(\phi) = \mu^2 \phi^\dagger \phi + \lambda (\phi^\dagger \phi)^2 \quad (2.31)$$

640        If  $\mu^2 > 0$  the potential has only one minimum at  $\phi = 0$  and describes a scalar field  
 641        with mass  $\mu$ . If  $\mu^2 < 0$  the potential has a local maximum at  $\phi = 0$  and two minima  
 642        at  $\phi = \pm\sqrt{-\mu^2/\lambda}$  which enables the SSB mechanism to work.

643

644        In the case of a complex scalar field  $\phi(x)$

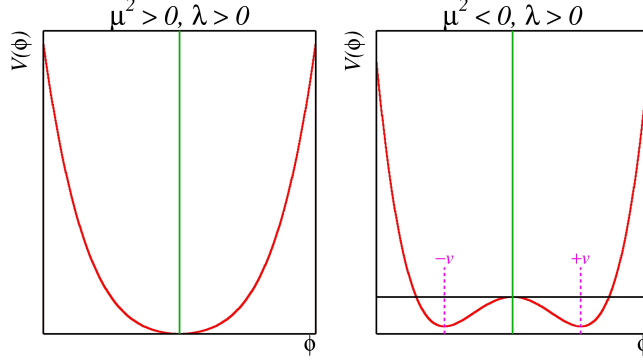


**Figure 2.7:** Shape of the potential  $V(\phi)$  for  $\lambda > 0$  and:  $\mu^2 > 0$  (left) and  $\mu^2 < 0$  (right). The case  $\mu^2 < 0$  corresponds to the potential suitable for introducing the SSB mechanism by choosing one of the two ground states which are connected via reflection symmetry. [27].

$$\phi(x) = \frac{1}{\sqrt{2}}(\phi_1 + i\phi_2) \quad (2.32)$$

645 the Lagrangian (invariant under global  $U(1)$  transformations) is given by

$$\mathcal{L} = (\partial_\mu \phi)^\dagger (\partial^\mu \phi) - V(\phi), \quad V(\phi) = \mu^2 \phi^\dagger \phi + \lambda (\phi^\dagger \phi)^2 \quad (2.33)$$

646 where an appropriate potential has been added in order to introduce the SSB.

647

648 As seen in Figure 2.8, the potential has now an infinite number of minima circularly  
 649 distributed along the  $\xi$ -direction which makes possible the occurrence of the SSB by  
 650 choosing an arbitrary ground state; for instance,  $\xi = 0$ , i.e.  $\phi_1 = v, \phi_2 = 0$

$$\phi_0 = \frac{v}{\sqrt{2}} \exp(i\xi) \xrightarrow{SSB} \phi_0 = \frac{v}{\sqrt{2}} \quad (2.34)$$

651 As usual, excitations over the ground state are studied by making an expansion

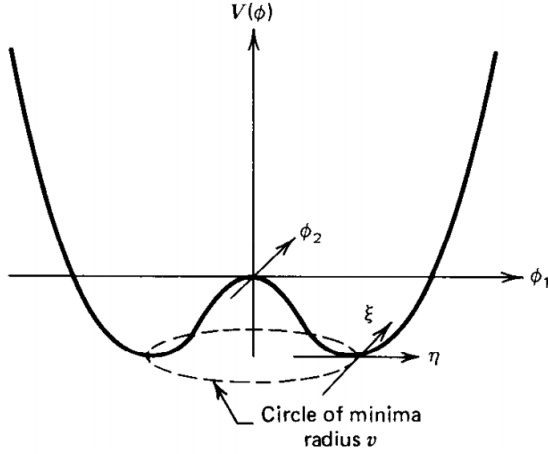


**Figure 2.8:** Potential for complex scalar field. There is a circle of minima of radius  $v$  along the  $\xi$ -direction [6].

652 about it; thus, the excitation can be parametrized as:

$$\phi(x) = \frac{1}{\sqrt{2}}(v + \eta(x) + i\xi(x)) \quad (2.35)$$

653 which when substituted into eqn. 2.33 produces a Lagrangian in terms of the new  
654 fields  $\eta$  and  $\xi$

$$\mathcal{L}' = \frac{1}{2}(\partial_\mu \xi)^2 + \frac{1}{2}(\partial_\mu \eta)^2 + \mu^2 \eta^2 - V(\phi_0) - \lambda v \eta (\eta^2 + \xi^2) - \frac{\lambda}{4}(\eta^2 + \xi^2)^2 \quad (2.36)$$

655 where the last two terms represent the interactions and self-interaction between the  
656 two fields  $\eta$  and  $\xi$ . The particular feature of the SSB mechanism is revealed when  
657 looking to the first three terms of  $\mathcal{L}'$ . Before the SSB, only the massless  $\phi$  field is  
658 present in the system; after the SSB there are two fields of which the  $\eta$ -field has  
659 acquired mass  $m_\eta = \sqrt{-2\mu^2}$  while the  $\xi$ -field is still massless (see Figure 2.9).

660

661 Thus, the SSB mechanism serves as a method to generate mass but as a side ef-

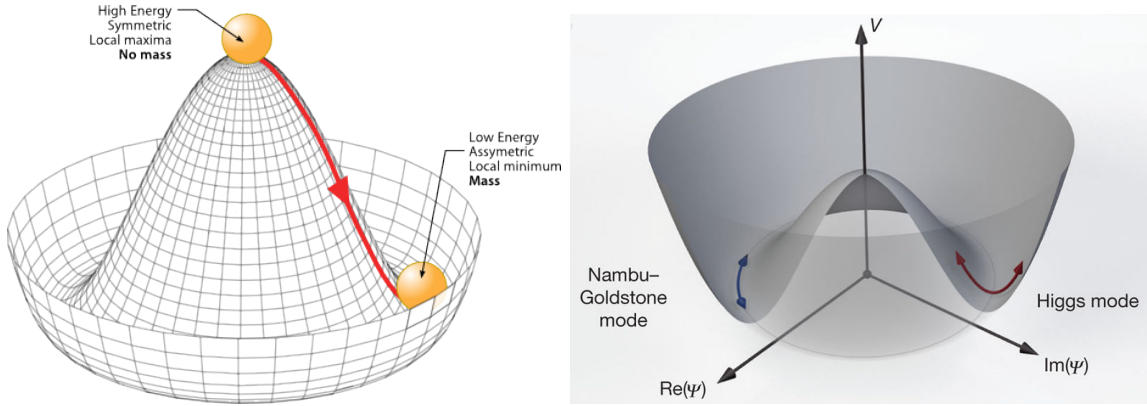


**Figure 2.9:** SSB mechanism for a complex scalar field [27, 28].

662 *fect a massless field is introduced in the system.* This fact is known as the Goldstone  
 663 theorem and states that a massless scalar field appears in the system for each con-  
 664 tinuous symmetry spontaneously broken. Another version of the Goldstone theorem  
 665 states that “*if a Lagrangian is invariant under a continuous symmetry group  $G$ , but*  
 666 *the vacuum is only invariant under a subgroup  $H \subset G$ , then there must exist as many*  
 667 *massless spin-0 particles (Nambu-Goldstone bosons) as broken generators.*” [26] The  
 668 Nambu-Goldstone boson can be understood considering that the potential in the  $\xi$ -  
 669 direction is flat so excitations in that direction are not energy consuming and thus  
 670 represent a massless state.

### 671 2.3.2 Higgs mechanism

672 When the SSB mechanism is introduced in the formulation of the EWI in an attempt  
 673 to generate the mass of the so far massless gauge bosons and fermions, an interesting  
 674 effect is revealed. In order to keep the  $G$  symmetry group invariance and generate  
 675 the mass of the EW gauge bosons, a  $G$  invariant Lagrangian density ( $\mathcal{L}_S$ ) has to be  
 676 added to the non massive EWI Lagrangian (eqn. 2.30)

$$\mathcal{L}_S = (D_\mu \phi)^\dagger (D^\mu \phi) - \mu^2 \phi^\dagger \phi - \lambda (\phi^\dagger \phi)^2, \quad \lambda > 0, \mu^2 < 0 \quad (2.37)$$

$$D_\mu \phi = \left( i\partial_\mu - g \frac{\sigma_i}{2} W_\mu^i - g' \frac{Y}{2} B_\mu \right) \phi \quad (2.38)$$

677  $\phi$  has to be an isospin doublet of complex scalar fields so it preserves the G invariance;  
 678 thus  $\phi$  can be defined as:

$$\phi = \begin{pmatrix} \phi^+ \\ \phi^0 \end{pmatrix} \equiv \frac{1}{\sqrt{2}} \begin{pmatrix} \phi_1 + i\phi_2 \\ \phi_3 + i\phi_4 \end{pmatrix}. \quad (2.39)$$

679 The minima of the potential are defined by

$$\phi^\dagger \phi = \frac{1}{2} (\phi_1^2 + \phi_2^2 + \phi_3^2 + \phi_4^2) = -\frac{\mu^2}{2\lambda}. \quad (2.40)$$

680 The choice of the ground state is critical. By choosing a ground state, invariant  
 681 under  $U(1)_{em}$  gauge symmetry, the photon will remain massless and the  $W^\pm$  and  $Z$   
 682 bosons masses will be generated which is exactly what is needed. In that sense, the  
 683 best choice corresponds to a weak isospin doublet with  $T_3 = -1/2$ ,  $Y_W = 1$  and  $Q = 0$   
 684 which defines a ground state with  $\phi_1 = \phi_2 = \phi_4$  and  $\phi_3 = v$ :

$$\phi_0 \equiv \frac{1}{\sqrt{2}} \begin{pmatrix} 0 \\ v \end{pmatrix}, \quad v^2 \equiv -\frac{\mu^2}{\lambda}. \quad (2.41)$$

685 where the vacuum expectation value  $v$  is fixed by the Fermi coupling  $G_F$  according  
 686 to  $v = (\sqrt{2}G_F)^{1/2} \approx 246$  GeV.

687

688 The G symmetry has been broken and three Nambu-Goldstone bosons will appear.

689 The next step is to expand  $\phi$  about the chosen ground state as:

$$\phi(x) = \frac{1}{\sqrt{2}} \exp\left(\frac{i}{v} \sigma_i \theta^i(x)\right) \begin{pmatrix} 0 \\ v + H(x) \end{pmatrix} \approx \frac{1}{\sqrt{2}} \begin{pmatrix} \theta_1(x) + i\theta_2(x) \\ v + H(x) - i\theta_3(x) \end{pmatrix} \quad (2.42)$$

690 to describe fluctuations from the ground state  $\phi_0$ . The fields  $\theta_i(x)$  represent the  
 691 Nambu-Goldstone bosons while  $H(x)$  is known as “higgs field.” The fundamental  
 692 feature of the parametrization used is that the dependence on the  $\theta_i(x)$  fields is  
 693 factored out in a global phase that can be eliminated by taking the physical “unitary  
 694 gauge”  $\theta_i(x) = 0$ . Therefore the expansion about the ground state is given by:

$$\phi(x) \frac{1}{\sqrt{2}} \begin{pmatrix} 0 \\ v + H(x) \end{pmatrix} \quad (2.43)$$

695 which when substituted into  $\mathcal{L}_S$  (eqn. 2.37) results in a Lagrangian containing the now  
 696 massive three gauge bosons  $W^\pm, Z$ , one massless gauge boson (photon) and the new  
 697 Higgs field ( $H$ ). The three degrees of freedom corresponding to the Nambu-Goldstone  
 698 bosons are now integrated into the massive gauge bosons as their longitudinal po-  
 699 larizations which were not available when they were massless particles. The effect  
 700 by which vector boson fields acquire mass after an spontaneous symmetry breaking,  
 701 but without an explicit gauge invariance breaking is known as the “*Higgs mechanism*”.

702

703 The mechanism was proposed by three independent groups: F.Englert and R.Brout  
 704 in August 1964 [29], P.Higgs in October 1964 [30] and G.Guralnik, C.Hagen and  
 705 T.Kibble in November 1964 [31]; however, its importance was not realized until  
 706 S.Glashow [22], A.Salam [23] and S.Weinberg [24], independently, proposed that elec-  
 707 tromagnetic and weak interactions are two manifestations of a more general interac-  
 708 tion called “electroweak interaction” in 1967.

709 **2.3.3 Masses of the gauge bosons**

710 The mass of the gauge bosons is extracted by evaluating the kinetic part of Lagrangian

711  $\mathcal{L}_S$  in the ground state (known also as the vacuum expectation value), i.e.,

$$\left| \left( \partial_\mu - ig \frac{\sigma_i}{2} W_\mu^i - i \frac{g'}{2} B_\mu \right) \phi_0 \right|^2 = \left( \frac{1}{2} v g \right)^2 W_\mu^+ W^{-\mu} + \frac{1}{8} v^2 (W_\mu^3, B_\mu) \begin{pmatrix} g^2 & -gg' \\ -gg' & g'^2 \end{pmatrix} \begin{pmatrix} W^{3\mu} \\ B^\mu \end{pmatrix} \quad (2.44)$$

712 comparing with the typical mass term for a charged boson  $M_W^2 W^+ W^-$

$$M_W = \frac{1}{2} v g. \quad (2.45)$$

The second term in the right side of the eqn.2.44 comprises the masses of the neutral bosons, but it needs to be written in terms of the gauge fields  $Z_\mu$  and  $A_\mu$  in order to be compared to the typical mass terms for neutral bosons, therefore using eqn. 2.29

$$\begin{aligned} \frac{1}{8} v^2 [g^2 (W_\mu^3)^2 - 2gg' W_\mu^3 B^\mu + g'^2 B_\mu^2] &= \frac{1}{8} v^2 [g W_\mu^3 - g' B_\mu]^2 + 0[g' W_\mu^3 + g B_\mu]^2 \quad (2.46) \\ &= \frac{1}{8} v^2 [\sqrt{g^2 + g'^2} Z_\mu]^2 + 0[\sqrt{g^2 + g'^2} A_\mu]^2 \end{aligned}$$

713 and then

$$M_Z = \frac{1}{2} v \sqrt{g^2 + g'^2}, \quad M_A = 0 \quad (2.47)$$

714 **2.3.4 Masses of the fermions**

715 The lepton mass terms can be generated by introducing a gauge invariant Lagrangian  
 716 term describing the Yukawa coupling between the lepton field and the Higgs field

$$\mathcal{L}_{Yl} = -G_l \left[ (\bar{\nu}_l, \bar{l})_L \begin{pmatrix} \phi^+ \\ \phi^0 \end{pmatrix} l_R + \bar{l}_R (\phi^-, \bar{\phi}^0) \begin{pmatrix} \nu_l \\ l \end{pmatrix}_L \right], \quad l = e, \mu, \tau. \quad (2.48)$$

717 After the SSB and replacing the usual field expansion about the ground state  
 718 (eqn.2.41) into  $\mathcal{L}_{Yl}$ , the mass term arises

$$\mathcal{L}_{Yl} = -m_l (\bar{l}_L l_R + \bar{l}_R l_L) - \frac{m_l}{v} (\bar{l}_L l_R + \bar{l}_R l_L) H = -m_l \bar{l} l \left( 1 + \frac{H}{v} \right) \quad (2.49)$$

719

$$m_l = \frac{G_l}{\sqrt{2}} v \quad (2.50)$$

720 where the additional term represents the lepton-Higgs interaction. The quark masses  
 721 are generated in a similar way as lepton masses but for the upper member of the  
 722 quark doublet a different Higgs doublet is needed:

$$\phi_c = -i\sigma_2 \phi^* = \begin{pmatrix} -\bar{\phi}^0 \\ \phi^- \end{pmatrix}. \quad (2.51)$$

723 Additionally, given that the quark isospin doublets are not constructed in terms of  
 724 the mass eigenstates but in terms of the flavor eigenstates, as shown in Table2.5, the  
 725 coupling parameters will be related to the CKM matrix elements; thus the quark  
 726 Lagrangian is given by:

$$\mathcal{L}_{Yq} = -G_d^{i,j} (\bar{u}_i, \bar{d}'_i)_L \begin{pmatrix} \phi^+ \\ \phi^0 \end{pmatrix} d_{jR} - G_u^{i,j} (\bar{u}_i, \bar{d}'_i)_L \begin{pmatrix} -\bar{\phi}^0 \\ \phi^- \end{pmatrix} u_{jR} + h.c. \quad (2.52)$$

727 with  $i,j=1,2,3$ . After SSB and expansion about the ground state, the diagonal form

728 of  $\mathcal{L}_{Yq}$  is:

$$\mathcal{L}_{Yq} = -m_d^i \bar{d}_i d_i \left(1 + \frac{H}{v}\right) - m_u^i \bar{u}_i u_i \left(1 + \frac{H}{v}\right) \quad (2.53)$$

729 Fermion masses depend on arbitrary couplings  $G_l$  and  $G_{u,d}$  and are not predicted  
730 by the theory.

### 731 2.3.5 The Higgs field

732 After the characterization of the fermions and gauge bosons as well as their interac-  
733 tions, it is necessary to characterize the Higgs field itself. The Lagrangian  $\mathcal{L}_S$  in eqn.  
734 2.37 written in terms of the gauge bosons is given by

$$\mathcal{L}_S = \frac{1}{4} \lambda v^4 + \mathcal{L}_H + \mathcal{L}_{HV} \quad (2.54)$$

735

$$\mathcal{L}_H = \frac{1}{2} \partial_\mu H \partial^\mu H - \frac{1}{2} m_H^2 H^2 - \frac{1}{2v} m_H^2 H^3 - \frac{1}{8v^2} m_H^2 H^4 \quad (2.55)$$

736

$$\mathcal{L}_{HV} = m_H^2 W_\mu^+ W^{\mu-} \left(1 + \frac{2}{v} H + \frac{2}{v^2} H^2\right) + \frac{1}{2} m_Z^2 Z_\mu Z^\mu \left(1 + \frac{2}{v} H + \frac{2}{v^2} H^2\right) \quad (2.56)$$

737 The mass of the Higgs boson is deduced as usual from the mass term in the Lagrangian  
738 resulting in:

$$m_H = \sqrt{-2\mu^2} = \sqrt{2\lambda}v \quad (2.57)$$

739 however, it is not predicted by the theory either. The experimental efforts to find  
740 the Higgs boson, carried out by the “Compact Muon Solenoid (CMS)” experiment  
741 and the “A Toroidal LHC AppartuS (ATLAS)” experiments at the “Large Hadron  
742 Collider(LHC)”, gave great results by July of 2012 when the discovery of a new  
743 particle compatible with the Higgs boson predicted by the electroweak theory [32, 33]  
744 was announced. Although at the announcement time there were some reservations  
745 about calling the new particle the “Higgs boson”, today this name is widely accepted.

746 The Higgs mass measurement, reported by both experiments [34], is in Table 2.8.

Property	Value
Electric charge	0
Colour charge	0
Spin	0
Weak isospin	-1/2
Weak hypercharge	1
Parity	1
Mass ( $\text{GeV}/c^2$ )	$125.09 \pm 0.21 \text{ (stat.)} \pm 0.11 \text{ (syst.)}$

**Table 2.8:** Higgs boson properties. Higgs mass is not predicted by the theory and the value here corresponds to the experimental measurement.

747

### 748 2.3.6 Production of Higgs bosons at LHC

749 At LHC, Higgs boson is produced as a result of the collision of two counter-rotating  
 750 protons beams. A detailed description of the LHC machine will be presented in  
 751 chapter 3. “The total cross section” is a parameter that quantifies the number of pp  
 752 collisions that happen when a number of protons are fired at each other. Different  
 753 results can be obtained after a pp collision and for each one the “cross section” is  
 754 defined as the number of pp collisions that conclude in that particular result with  
 755 respect to the number of protons fired at each other.

756 Protons are composed of quarks and these quarks are bound by gluons; however,  
 757 what is commonly called the quark content of the proton makes reference to the  
 758 valence quarks. A sea of quarks and gluons is also present inside the proton as rep-  
 759 resented in Figure 2.10. In a proton-proton (pp) collision, the constituents (quarks  
 760 and gluons) are those who collide. The pp cross section depends on the momentum  
 761 of the colliding particles, reason for which it is needed to know how the momentum is  
 762 distributed inside the proton. Quarks and gluons are known as partons and the func-  
 763 tions that describe how the proton momentum is distributed among partons inside it

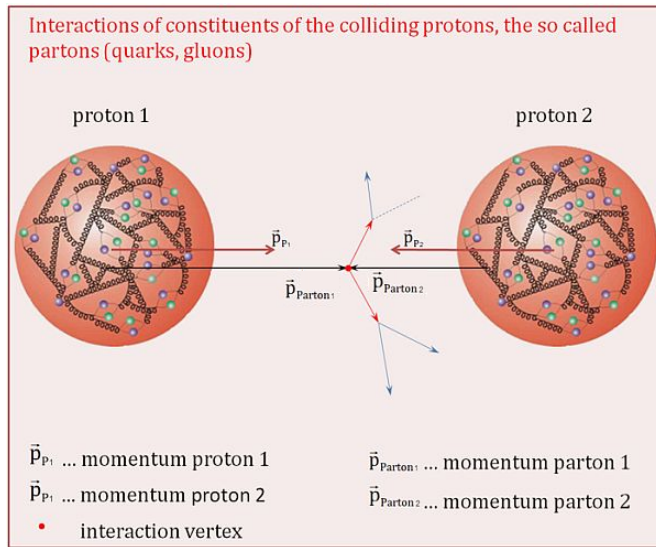


**Figure 2.10:** Proton-proton collision. Protons are composed of 3 valence quarks, a sea of quarks and gluons; therefore in a proton-proton collision, quarks and gluons are those who collide. [35].

764 are called “parton distribution functions (PDFs)”; PDFs are determined from experi-  
765 mental data obtained in experiments where the internal structure of hadrons is tested.

766

In addition, in physics, a common approach to study complex systems consists in starting with a simpler version of them, for which a well known description is available, and add an additional “perturbation” which represents a small deviation from the known behavior. If the perturbation is small enough, the physical quantities associated with the perturbed system are expressed as a series of corrections to those of the simpler system; therefore, the more terms are considered in the series (the higher order in the perturbation series), the more precise is the the description of the complex system.

775

This thesis explores the Higgs production at LHC; therefore the overview presented here will be oriented specifically to the production mechanisms after pp collisions at

778 LHC.

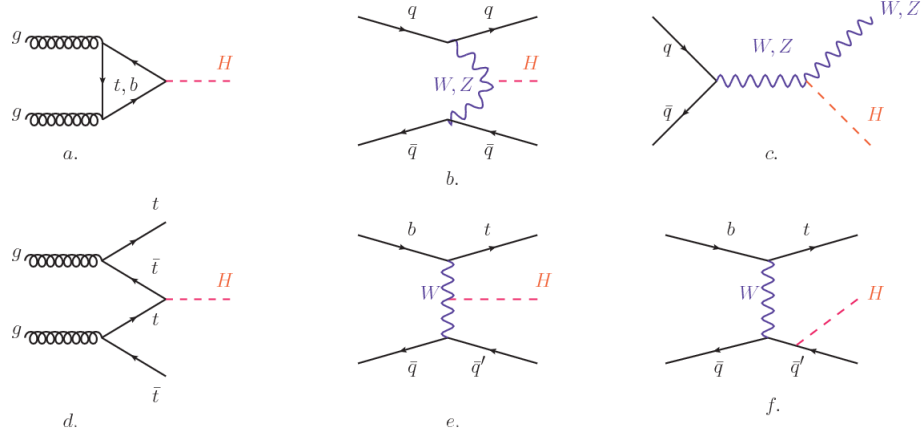


**Figure 2.11:** Main Higgs boson production mechanism Feynman diagrams. a. gluon-gluon fusion, b. vector boson fusion (VBF), c. Higgs-strahlung, d. Associated production with a top or bottom quark pair, e-f. associated production with a single top quark.

779 Figure 2.11 shows the Feynman diagrams for the leading order (first order) Higgs  
 780 production processes at LHC, while the cross section for Higgs production as a func-  
 781 tion of the center of mass-energy ( $\sqrt{s}$ ) for pp collisions is showed in Figure 2.12 left.  
 782 The tags NLO (next to leading order), NNLO (next to next to leading order) and  
 783 N3LO (next to next to next to leading order) make reference to the order at which  
 784 the perturbation series have been considered.

785 As shown in eqns 2.48, 2.52 and 2.56, the strength of the Higgs-fermion interaction  
 786 is proportional to the fermion mass while the strength of the Higgs-gauge boson  
 787 interaction is proportional to the square of the gauge boson mass, which implies  
 788 that the Higgs production and decay mechanisms are dominated by couplings  $H -$   
 789  $(W, Z, t, b, \tau)$ .

790 The main production mechanism is the gluon fusion (Figure 2.11a and  $pp \rightarrow H$  in  
 791 Figure 2.12) given that gluons carry the highest fraction of momentum of the protons  
 792 in pp colliders. Since the Higgs boson does not couple to gluons, the mechanism pro-  
 793 ceeds through the exchange of a virtual top-quark loop given that for it the coupling

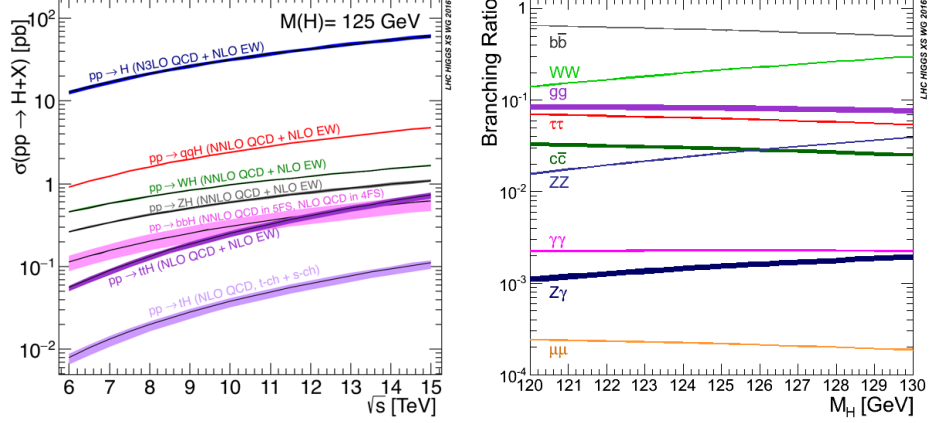


**Figure 2.12:** Higgs boson production cross sections (left) and decay branching ratios (right) for the main mechanisms. The VBF is indicated as  $qqH$  [36].

is the biggest. Note that in this process, the Higgs boson is produced alone, which makes this mechanism experimentally clean when combined with the two-photon or the four-lepton decay channels (see Section 2.3.7).

Vector boson fusion (Figure 2.11b and  $pp \rightarrow qqH$  in Figure 2.12) has the second largest production cross section. The scattering of two fermions is mediated by a weak gauge boson which later emits a Higgs boson. In the final state, the two fermions tend to be located in a particular region of the detector which is used as a signature when analyzing the datasets provided by the experiments. More details about how to identify events of interest in an analysis will be given in chapter 6.

The next production mechanism is Higgs-strahlung (Figure 2.11c and  $pp \rightarrow WH, pp \rightarrow ZH$  in Figure 2.12) where two fermions annihilate to form a weak gauge boson. If the initial fermions have enough energy, the emergent boson eventually will emit a Higgs boson.

The associated production with a top or bottom quark pair and the associated production with a single top quark (Figure 2.11d-f and  $pp \rightarrow bbH, pp \rightarrow t\bar{t}H, pp \rightarrow tH$  in Figure 2.12) have a smaller cross section than the main three mechanisms above,

810 but they provide a good opportunity to test the Higgs-top coupling. The analysis  
 811 reported in this thesis is developed using these production mechanisms. A detailed  
 812 description of the  $tH$  mechanism will be given in Section 2.4.

### 813 2.3.7 Higgs boson decay channels

814 When a particle can decay through several modes, also known as channels, the  
 815 probability of decaying through a given channel is quantified by the “branching ratio  
 816 (BR)” of the decay channel; thus, the BR is defined as the ratio of number of decays  
 817 going through that given channel to the total number of decays. In regard to the  
 818 Higgs boson decay, the BR can be predicted with accuracy once the Higgs mass is  
 819 known [37, 38]. In Figure 2.12 right, a plot of the BR as a function of the Higgs mass  
 820 is presented. The largest predicted BR corresponds to the  $b\bar{b}$  pair decay channel (see  
 821 Table 2.9).

Decay channel	Branching ratio	Rel. uncertainty
$H \rightarrow b\bar{b}$	$5.84 \times 10^{-1}$	$+3.2\% - 3.3\%$
$H \rightarrow W^+W^-$	$2.14 \times 10^{-1}$	$+4.3\% - 4.2\%$
$H \rightarrow \tau^+\tau^-$	$6.27 \times 10^{-2}$	$+5.7\% - 5.7\%$
$H \rightarrow ZZ$	$2.62 \times 10^{-2}$	$+4.3\% - 4.1\%$
$H \rightarrow \gamma\gamma$	$2.27 \times 10^{-3}$	$+5.0\% - 4.9\%$
$H \rightarrow Z\gamma$	$1.53 \times 10^{-3}$	$+9.0\% - 8.9\%$
$H \rightarrow \mu^+\mu^-$	$2.18 \times 10^{-4}$	$+6.0\% - 5.9\%$

**Table 2.9:** Predicted branching ratios and the relative uncertainty for a SM Higgs boson with  $m_H = 125 GeV/c^2$ . [9]

823 **2.4 Associated production of a Higgs boson and a  
824 single Top quark.**

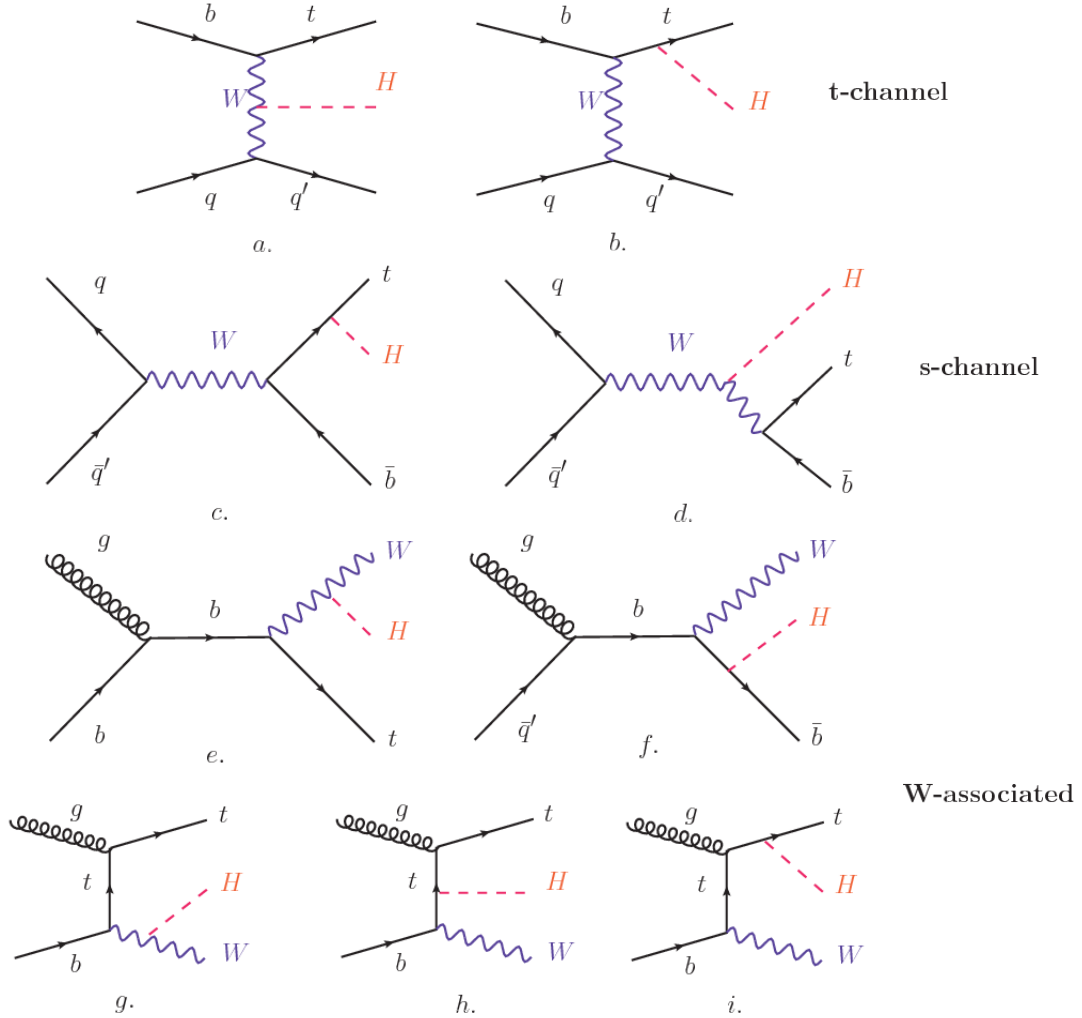


**Figure 2.13:** Associated Higgs boson production mechanism Feynman diagrams. a.,b. t-channel (tHq), c.,d. s-channel (tHb), e-i. W-associated.

825      Associated production of Higgs boson has been extensively studied [39–43]. While  
826      measurements of the main Higgs production mechanisms rates are sensitive to the  
827      strength of the Higgs coupling to W boson or top quark, they are not sensitive to the  
828      relative sign between the two couplings. In this thesis, the Higgs boson production

mechanism explored is the associated production with a single top quark ( $tH$ ) which offers sensitiveness to the relative sign of the Higgs couplings to W boson and to top quark. The description given here is based on the Reference [41]

832

833 A process where two incoming particles interact and produce a final state with two  
 834 particles can proceed in three ways also called channels (see, for instance, Figure 2.13  
 835 ommiting the red line). The t-channel represents processes where an intermediate  
 836 particle is emitted by one of the incoming particles and absorbed by the other. The  
 837 s-channel represents processes where the two incoming particles merge into an inter-  
 838 mediate particle which eventually will split into the particles in the final state. The  
 839 third channel, u-channel, is similar to the t-channel but the two outgoing particles  
 840 interchange their roles.

841

842 The  $tH$  production, where Higgs boson can be radiated either from the top quark  
 843 or from the W boson, is represented by the leading order Feynman diagrams in  
 844 Figure ???. The cross section for the  $tH$  process is calculated, as usual, summing over  
 845 the contributions from the different feynman diagrams; therefore it depends on the  
 846 interference between the contributions. In the SM, the interference for t-channel ( $tHq$   
 847 process) and W-associated ( $tHW$  process) production is destructive [39] resulting in  
 848 the small cross sections presented in Table 2.10.

tH production channel	Cross section (fb)
t-channel ( $pp \rightarrow tHq$ )	$70.79^{+2.99}_{-4.80}$
W-associated ( $pp \rightarrow tHW$ )	$15.61^{+0.83}_{-1.04}$
s-channel( $pp \rightarrow tHb$ )	$2.87^{+0.09}_{-0.08}$

**Table 2.10:** Predicted SM cross sections for  $tH$  production at  $\sqrt{s} = 13$  TeV [44, 45].

849

850 While the s-channel contribution can be neglected, it will be shown that a de-  
 851 viation from the SM destructive interference would result in an enhancement of the  
 852  $tH$  cross section compared to that in SM, which could be used to get information  
 853 about the sign of the Higgs-top coupling [41, 42]. In order to describe  $tH$  production  
 854 processes, Feynman diagram 2.13b will be considered; there, the W boson is radiated  
 855 by a quark in the proton and eventually it will interact with the b quark. In the  
 856 high energy regime, the effective W approximation [46] allows to describe the process  
 857 as the emmision of an approximately on-shell W and its hard scattering with the b  
 858 quark; i.e.  $Wb \rightarrow th$ . The scattering amplitude for the process is given by

$$\mathcal{A} = \frac{g}{\sqrt{2}} \left[ (\kappa_t - \kappa_V) \frac{m_t \sqrt{s}}{m_W v} A \left( \frac{t}{s}, \varphi; \xi_t, \xi_b \right) + \left( \kappa_V \frac{2m_W s}{v} \frac{1}{t} + (2\kappa_t - \kappa_V) \frac{m_t^2}{m_W v} \right) B \left( \frac{t}{s}, \varphi; \xi_t, \xi_b \right) \right], \quad (2.58)$$

859 where  $\kappa_V \equiv g_{HVV}/g_{HVV}^{SM}$  and  $\kappa_t \equiv g_{Ht}/g_{Ht}^{SM} = y_t/y_t^{SM}$  are scaling factors that quan-  
 860 tify possible deviations of the couplings, Higgs-Vector boson (H-W) and Higgs-top  
 861 (H-t) respectively, from the SM couplings;  $s = (p_W + p_b)^2$ ,  $t = (p_W - p_H)^2$ ,  $\varphi$  is the  
 862 Higgs azimuthal angle around the  $z$  axis taken parallel to the direction of motion of  
 863 the incoming W; A and B are funtions describing the weak interaction in terms of  
 864 the chiral states of the quarks  $b$  and  $t$ . Terms that vanish in the high energy limit  
 865 have been neglected as well as the Higgs and  $b$  quark masses<sup>7</sup>.

866

867 The scattering amplitude grows with energy like  $\sqrt{s}$  for  $\kappa_V \neq \kappa_t$ , in contrast to  
 868 the SM ( $\kappa_t = \kappa_V = 1$ ), where the first term in 2.58 cancels out and the amplitude  
 869 is constant for large  $s$ ; therefore, a deviation from the SM predictions represents an  
 870 enhancement in the  $tHq$  cross section. In particular, for a SM H-W coupling and a

---

<sup>7</sup> A detailed explanation of the structure and approximations used to derive  $\mathcal{A}$  can be found in Reference [41]

871 H-t coupling of inverted sign with respect to the SM ( $\kappa_V = -\kappa_t = 1$ ) the  $tHq$  cross  
 872 section is enhanced by a factor greater 10 as seen in the Figure 2.14 taken from  
 873 Reference [41]; Reference [47] has reported similar enhancement results.

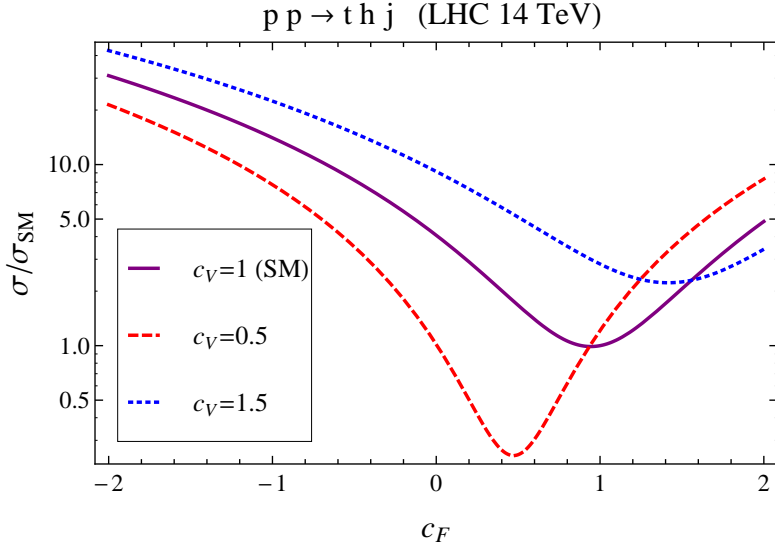


**Figure 2.14:** Cross section for  $tHq$  process as a function of  $\kappa_t$ , normalized to the SM, for three values of  $\kappa_V$ . In the plot  $c_f$  refers to the Higgs-fermion coupling which is dominated by the H-t coupling and represented here by  $\kappa_t$ . Solid, dashed and dotted lines correspond to  $c_V \rightarrow \kappa_V = 1, 0.5, 1.5$  respectively. Note that for the SM ( $\kappa_V = \kappa_t = 1$ ), the destructive effect of the interference is maximal.

874 A similar analysis is valid for the W-associated channel but, in that case, the in-  
 875 terference is more complicated since there are more than two contributions and an ad-  
 876 ditional interference with the production of Higgs boson and a top pair process( $t\bar{t}H$ ).  
 877 The calculations are made using the so-called Diagram Removal (DR) technique where  
 878 interfering diagrams are removed (or added) from the calculations in order to evaluate  
 879 the impact of the removed contributions. DR1 was defined to neglect  $t\bar{t}H$  interference  
 880 while DR2 was defined to take  $t\bar{t}H$  interference into account [48]. As shown in Figure  
 881 2.15, the  $tHW$  cross section is enhanced from about 15 fb (SM:  $\kappa_{Htt} = 1$ ) to about  
 882 150 fb ( $\kappa_{Htt} = -1$ ). Differences between curves for DR1 and DR2 help to gauge the  
 883 impact of the interference with  $t\bar{t}H$ .

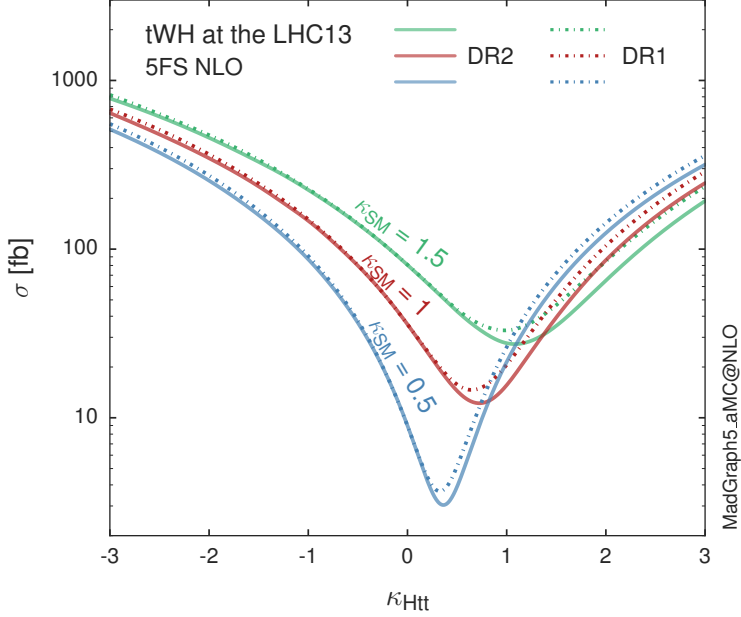


**Figure 2.15:** Cross section for  $tHW$  process as a function of  $\kappa_{Htt}$ , for three values of  $\kappa_{SM}$  at  $\sqrt{s} = 13$  TeV.  $\kappa_{Htt}^2 = \sigma_{Htt}/\sigma_{Htt}^{SM}$  is a simple rescaling of the SM Higgs interactions.

884 Results of the calculations of the  $tHq$  and  $tHW$  cross sections at  $\sqrt{s} = 13$  TeV can be  
 885 found in Reference [49] and a summary of the results is presented in Table 2.11.

886

## 887 2.5 The CP-mixing in tH processes

888 In addition to the sensitivity to sign of the H-t coupling,  $tHq$  and  $tHW$  processes have  
 889 been proposed as a tool to investigate the possibility of a H-t coupling that does not  
 890 conserve CP [43, 48, 50]. Current experimental results are consistent with SM H-V  
 891 and H-t couplings; however, negative H-t coupling is not excluded completely [53].

892

893 In this thesis, the sensitivity of  $tH$  processes to CP-mixing is also studied in the  
 894 effective field theory framework and based in References [43, 48]; a generic particle

	$\sqrt{s}$ TeV	$\kappa_t = 1$	$\kappa_t = -1$
$\sigma^{LO}(tHq)(\text{fb})$ [41]	8	$\approx 17.4$	$\approx 252.7$
	14	$\approx 80.4$	$\approx 1042$
$\sigma^{NLO}(tHq)(\text{fb})$ [41]	8	$18.28^{+0.42}_{-0.38}$	$233.8^{+4.6}_{-0.0}$
	14	$88.2^{+1.7}_{-0.0}$	$982.8^{+28}_{-0.0}$
$\sigma^{LO}(tHq)(\text{fb})$ [47]	14	$\approx 71.8$	$\approx 893$
$\sigma^{LO}(tHW)(\text{fb})$ [47]	14	$\approx 16.0$	$\approx 139$
$\sigma^{NLO}(tHq)(\text{fb})$ [49]	8	$18.69^{+8.62\%}_{-17.13\%}$	-
	13	$74.25^{+7.48\%}_{-15.35\%}$	$848^{+7.37\%}_{-13.70\%}$
	14	$90.10^{+7.34\%}_{-15.13\%}$	$1011^{+7.24\%}_{-13.39\%}$
$\sigma^{LO}(tHW)(\text{fb})$ [48]	13	$15.77^{+15.91\%}_{-15.76\%}$	-
$\sigma^{NLO}DR1(tHW)(\text{fb})$ [48]	13	$21.72^{+6.52\%}_{-5.24\%}$	$\approx 150$
$\sigma^{NLO}DR2(tHW)(\text{fb})$ [48]	13	$16.28^{+7.34\%}_{-15.13\%}$	$\approx 150$

**Table 2.11:** Predicted enhancement of the  $tHq$  and  $tHW$  cross sections at LHC for  $\kappa_V = 1$  and  $\kappa_t = \pm 1$  at LO and NLO; the cross section enhancement of more than a factor of 10 is due to the flippling in the sign of the H-t coupling with respect to the SM one.

895 ( $X_0$ ) of spin-0 and a general CP violating interaction with the top quark, can couple  
 896 to scalar and pseudoscalar fermionic densities. The H-W interaction is assumed to  
 897 be SM-like. The Lagrangian modeling the H-t interaction is given by

$$\mathcal{L}_0^t = -\bar{\psi}_t (c_\alpha \kappa_{Htt} g_{Htt} + i s_\alpha \kappa_{Att} g_{Att} \gamma_5) \psi_t X_0, \quad (2.59)$$

898 where  $\alpha$  is the CP-mixing phase,  $c_\alpha \equiv \cos \alpha$  and  $s_\alpha \equiv \sin \alpha$ ,  $\kappa_{Htt}$  and  $\kappa_{Att}$  are real  
 899 dimensionless rescaling parameters<sup>8</sup>,  $g_{Htt} = g_{Att} = m_t/v = y_t/\sqrt{2}$  and  $v \sim 246$  GeV is  
 900 the Higgs vacuum expectation value. In this parametrization, it is easy to recover  
 901 three special cases

902 • CP-even coupling  $\rightarrow \alpha = 0^\circ$

903 • CP-odd coupling  $\rightarrow \alpha = 90^\circ$

904 • SM coupling  $\rightarrow \alpha = 0^\circ$  and  $\kappa_{Htt} = 1$

---

<sup>8</sup> analog to  $\kappa_t$  and  $\kappa_V$

905        The loop induced  $X_0$  coupling to gluons can also be described in terms of the  
 906        parametrization above, according to

$$\mathcal{L}_0^g = -\frac{1}{4} \left( c_\alpha \kappa_{Hgg} g_{Hgg} G_{\mu\nu}^a G^{a,\mu\nu} + s_\alpha \kappa_{Agg} g_{Agg} G_{\mu\nu}^a \tilde{G}^{a,\mu\nu} \right) X_0. \quad (2.60)$$

907        where  $g_{Hgg} = -\alpha_s/3\pi v$  and  $g_{Agg} = \alpha_s/2\pi v$ . Under the assumption that the top quark  
 908        dominates the gluon-fusion process at LHC energies,  $\kappa_{Hgg} \rightarrow \kappa_{Htt}$  and  $\kappa_{Agg} \rightarrow \kappa_{Att}$ ,  
 909        so that the ratio between the gluon-gluon fusion cross section for  $X_0$  and for the SM  
 910        Higgs prediction can be written as

$$\frac{\sigma_{NLO}^{gg \rightarrow X_0}}{\sigma_{NLO,SM}^{gg \rightarrow H}} = c_\alpha^2 \kappa_{Htt}^2 + s_\alpha^2 \left( \kappa_{Att} \frac{g_{Agg}}{g_{Hgg}} \right)^2. \quad (2.61)$$

911        If the rescaling parameters are set to

$$\kappa_{Htt} = 1, \quad \kappa_{Att} = \left| \frac{g_{Hgg}}{g_{Agg}} \right| = \frac{2}{3}. \quad (2.62)$$

912        the gluon-fusion SM cross section is reproduced for every value of the CP-mixing  
 913        angle  $\alpha$ ; therefore, by imposing that condition to the Lagrangian density 2.59, the  
 914        CP-mixing angle is not constrained by current data. Figure 2.16 shows the NLO cross  
 915        sections for t-channel  $tX_0$  (blue) and  $t\bar{t}X_0$  (red) associated production processes as  
 916        a function of the CP-mixing angle  $\alpha$ .  $X_0$  is a generic spin-0 particle with top quark  
 917        CP-violating coupling. Rescaling factors  $\kappa_{Htt}$  and  $\kappa_{Att}$  have been set to reproduce  
 918        the SM gluon-fusion cross sections.

919        It is interesting to notice that the  $tX_0$  cross section is enhanced, by a factor of  
 920        about 10, when a continuous rotation in the scalar-pseudoscalar plane is applied; this  
 921        enhancement is similar to the enhancement produced when the H-t coupling is flipped  
 922        in sign with respect to the SM ( $y_t = -y_{t,SM}$  in the plot), as showed in Section 2.4. In

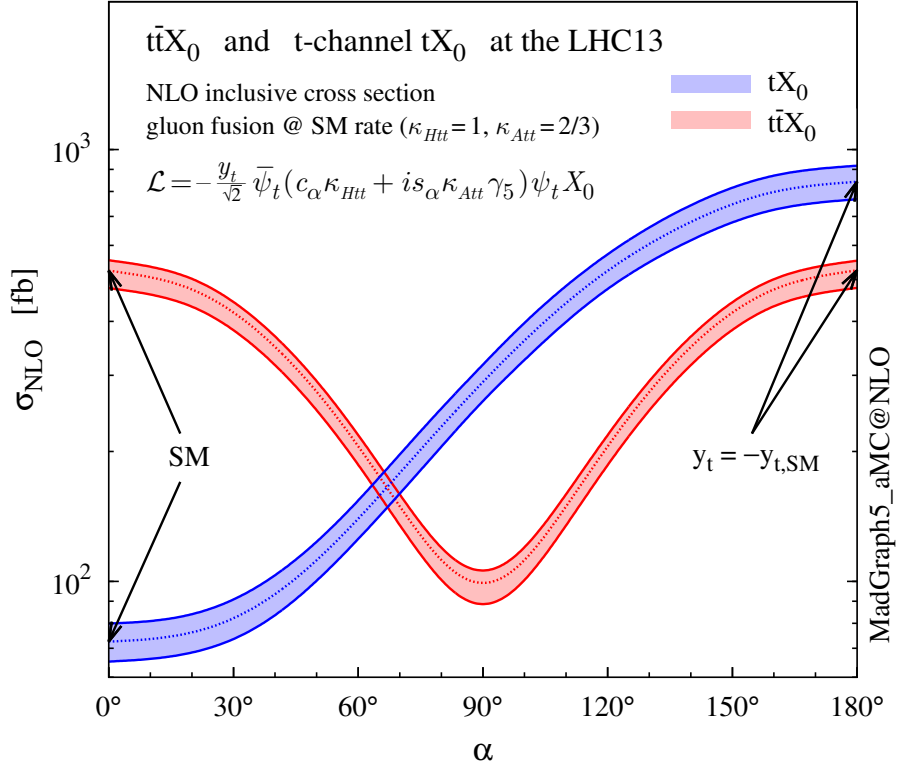


**Figure 2.16:** NLO cross sections for t-channel  $tX_0$ (blue) and  $t\bar{t}X_0$  (red) associated production processses as a function of the CP-mixing angle  $\alpha$ .  $X_0$  is a generic spin-0 particle with top quark CP-violating coupling [43].

contrast, the degeneracy in the  $t\bar{t}X_0$  cross section is still present given that it depends quadratically on the H-t coupling, but more insteresting is to notice that  $t\bar{t}X_0$  cross section is exceeded by  $tX_0$  cross section after  $\alpha \sim 60^\circ$ .

A similar parametrization can be used to investigate the  $tHW$ process sensitivity to CP-violating H-t coupling. As said in 2.4, the interference in the W-associated channel is more complicated because there are more than two contributions and also there is interference with the  $t\bar{t}H$  production process.

930

931 Figure 2.17 shows the NLO cross sections for t-channel  $tX_0$ (blue),  $t\bar{t}X_0$  (red)  
932 associated production and for the combined  $tWX_0 + t\bar{t}X_0 +$  interference (orange) as

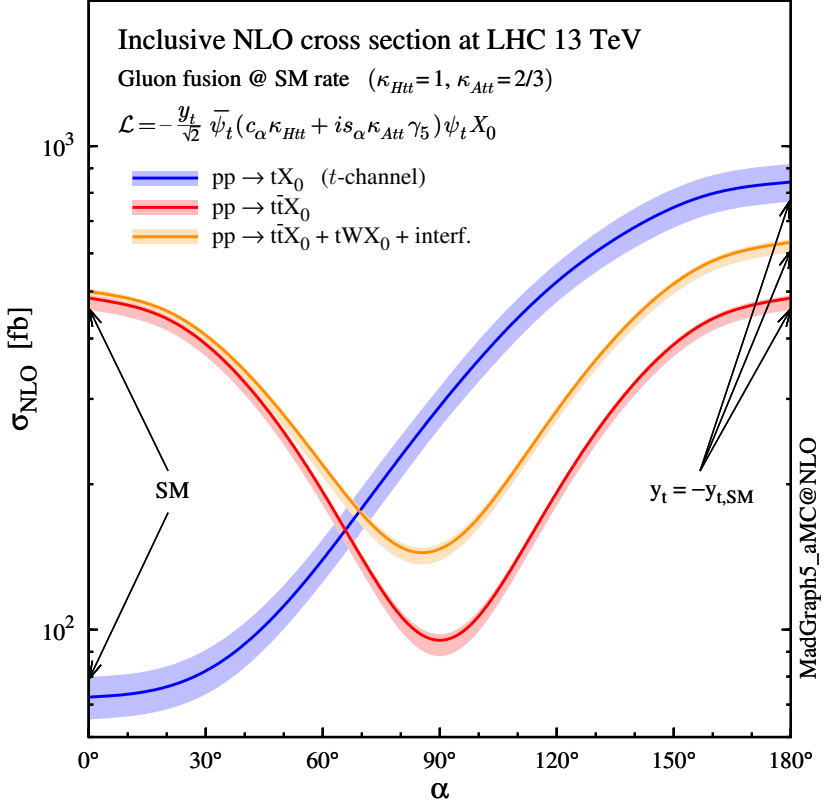


**Figure 2.17:** NLO cross sections for t-channel  $tX_0$  (blue),  $t\bar{t}X_0$  (red) associated production processes and combined  $tWX_0 + t\bar{t}X_0$  (including interference) production as a function of the CP-mixing angle  $\alpha$  [43].

933 a function of the CP-mixing angle. It is clear that the effect of the interference in the  
934 combined case is the lifting of the degeneracy present in the  $t\bar{t}X_0$  production. The  
935 constructive interference enhances the cross section from about 500 fb at SM ( $\alpha = 0$ )  
936 to about 600 fb ( $\alpha = 180^\circ \rightarrow y_t = -y_{t,SM}$ ).

937 An analysis combining  $tHq$  and  $tHW$  processes will be made in this thesis taking  
938 advantage of the sensitivity improvement.

939 **2.6 Experimantal status of the anomalous**  
 940 **Higg-fermion coupling.**

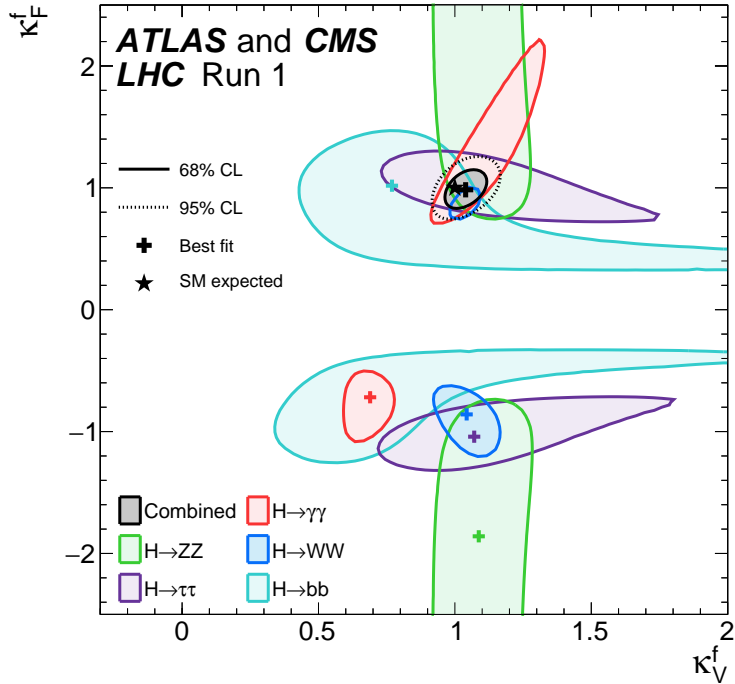


**Figure 2.18:** Combination of the ATLAS and CMS fits for coupling modifiers  $\kappa_t$ - $\kappa_V$ ; also shown the individual decay channels combination and their global combination. No assumptions have been made on the sign of the coupling modifiers [53].

941       ATLAS and CMS have performed analysis of the anomalous H-f coupling by mak-  
 942       ing likelihood scans for the two coupling modifiers,  $\kappa_t$  and  $\kappa_V$ , under the assumption  
 943       that  $\kappa_Z = \kappa_W = \kappa_V$  and  $\kappa_t = \kappa_\tau = \kappa_b = \kappa_f$ . Figure 2.18 shows the result of the combi-  
 944       nation of ATLAS and CMS fits; also the individual decay channels combination and  
 945       the global combination results are shown.

946       While all the channels are compatible for positive values of the modifiers, for negative  
 947       values of  $\kappa_t$  there is no compatibility. The best fit for individual channels is compatible  
 948       with negative values of  $\kappa_t$  except for the  $H \rightarrow bb$  channel which is expected to be the

949 most sensitive channel; therefore, the best fit for the global fit yields  $\kappa_t \geq 0$ . Thus,  
950 the anomalous H-t coupling cannot be excluded completely.

# 951 Chapter 3

## 952 The CMS experiment at the LHC

### 953 3.1 Introduction

954 Located on the Swiss-French border, the European Council for Nuclear Research  
955 (CERN) is the largest scientific organization leading the particle physics research.  
956 About 13000 people in a broad range of fields including users, students, scientists,  
957 engineers, among others, contribute to the data taking and analysis, with the goal  
958 of unveiling the secrets of nature and revealing the fundamental structure of the  
959 universe. CERN is also the home of the Large Hadron Collider (LHC), the largest  
960 circular particle accelerator around the world, where protons (or heavy ions) traveling  
961 close to the speed of light, are made to collide. These collisions open a window  
962 to investigate how particles (and their constituents if they are composite) interact  
963 with each other, providing clues about the laws of nature. This chapter presents an  
964 overview of the LHC structure and operation. A detailed description of the CMS  
965 detector is offered, given that the data used in this thesis have been taken with this  
966 detector.

## 967 3.2 The LHC

968 With 27 km of circumference, the LHC is currently the largest and most powerful  
 969 circular accelerator in the world. It is installed in the same tunnel where the Large  
 970 Electron-Positron (LEP) collider was located, taking advantage of the existing infras-  
 971 tructure. The LHC is also the larger accelerator in the CERN's accelerator complex  
 972 and is assisted by several successive accelerating stages before the particles are in-  
 973 jected into the LHC ring where they reach their maximum energy (see Figure 3.1).

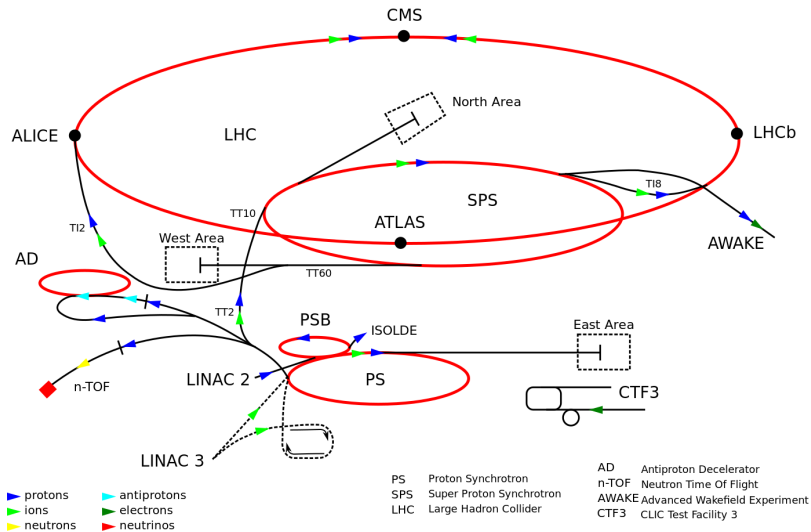


**Figure 3.1:** CERN accelerator complex. Blue arrows show the path followed by protons along the acceleration process [54].

974 LHC runs in three modes depending on the particles being accelerated

- 975     • Proton-Proton collisions ( $pp$ ) for multiple physics experiments.
- 976     • Lead-Lead collisions ( $Pb-Pb$ ) for heavy ion experiments.
- 977     • Proton-Lead collisions ( $p-Pb$ ) for quark-gluon plasma experiments.

978 In this thesis only  $pp$  collisions will be considered.

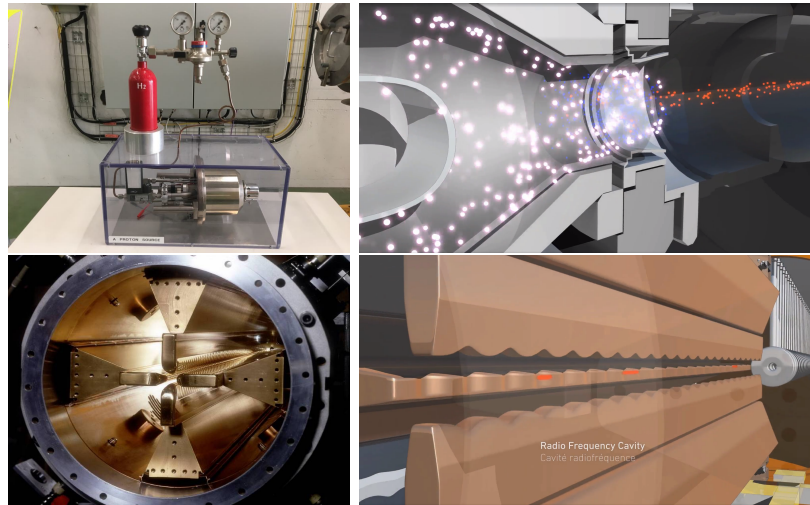


**Figure 3.2:** LHC protons source and the first acceleration stage. Top: the bottle contains hydrogen gas (white dots) which is injected into the metal cylinder to be broken down into electrons (blue dots) and protons (red dots); Bottom: the obtained protons are directed towards the radio frequency quadrupole which perform the first acceleration, focus the beam and create the bunches of protons. [58, 59]

980 Collection of protons starts with hydrogen atoms taken from a bottle, containing hy-  
 981 drogen gas, and injecting them in a metal cylinder; hydrogen atoms are broken down  
 982 into electrons and protons by an intense electric field (see Figure 3.2 top). The re-  
 983 sulting protons leave the metal cylinder towards a radio frequency quadrupole (RFQ)  
 984 that focus the beam, accelerates the protons and creates the packets of protons called  
 985 bunches. In the RFQ, an electric field is generated by a RF wave at a frequency that  
 986 matches the resonance frequency of the cavity where the electrodes are contained.  
 987 The beam of protons traveling on the RFQ axis experiences an alternating electric  
 988 field gradient that generates the focusing forces.

989

990 In order to accelerate the protons, a longitudinal time-varying electric field component  
 991 is added to the system; it is done by giving the electrodes a sinus-like profile as shown  
 992 in Figure 3.2 bottom. By matching the speed and phase of the protons with the  
 993 longitudinal electric field the bunching is performed; protons synchronized with the

994 RFQ (synchronous proton) do not feel an accelerating force, but those protons in the  
 995 beam that have more (or less) energy than the synchronous proton (asynchronous  
 996 protons) will feel a decelerating (accelerating) force; therefore, asynchronous protons  
 997 will oscillate around the synchronous ones forming bunches of protons [56]. From the  
 998 RFQ protons emerge with energy 750 keV in bunches of about  $1.15 \times 10^{11}$  protons [57].

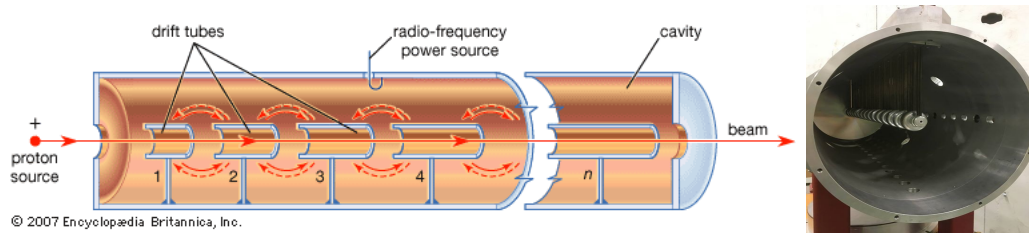


**Figure 3.3:** The LINAC2 accelerating system at CERN. Electric fields generated by radio frequency (RF) create acceleration and deceleration zones inside the cavity; deceleration zones are blocked by drift tubes where quadrupole magnets focus the proton beam. [60]

999 Proton bunches coming from the RFQ go to the linear accelerator 2 (LINAC2) where  
 1000 they are accelerated to reach 50 MeV energy. In the LINAC2 stage, acceleration  
 1001 is performed using electric fields generated by radio frequency which create zones  
 1002 of acceleration and deceleration as shown in Figure 3.3. In the deceleration zones,  
 1003 the electric field is blocked using drift tubes where protons are free to drift while  
 1004 quadrupole magnets focus the beam.

1005

1006 The beam coming from LINAC2 is injected into the proton synchrotron booster  
 1007 (PSB) to reach 1.4 GeV in energy. The next acceleration is provided at the pro-  
 1008 ton synchrotron (PS) up to 26 GeV, followed by the injection into the super proton  
 1009 synchrotron (SPS) where protons are accelerated to 450 GeV. Finally, protons are  
 1010 injected into the LHC where they are accelerated to the target energy of 6.5 TeV.  
 1011 PSB, PS, SPS and LHC accelerate protons using the same RF acceleration technique  
 1012 described before.

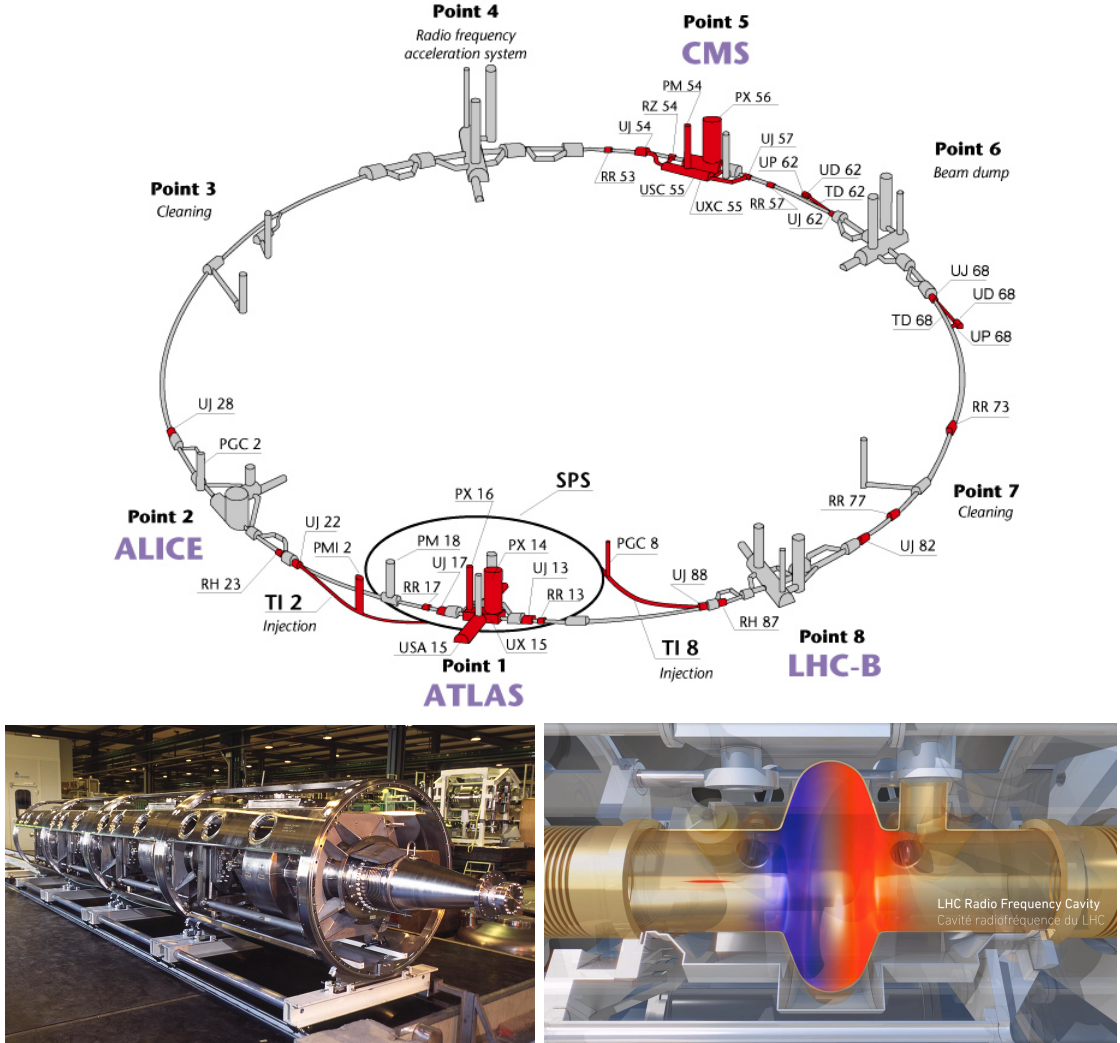


**Figure 3.4:** Top: LHC layout. The red zones indicate the infrastructure additions to the LEP installations, built to accommodate the ATLAS and CMS experiments which exceed the size of the former experiments located there [55]. Bottom: LHC RF cavities. A module accommodates 4 cavities that accelerate protons and preserve the bunch structure of the beam. [59, 61]

1013 LHC has a system of 16 RF cavities located in the so-called point 4, as shown in  
 1014 Figure 3.4 top, tuned at a frequency of 400 MHz and the protons are carefully timed,  
 1015 so in addition to the acceleration effect the bunch structure of the beam is preserved.  
 1016 Bottom side of Figure 3.4 shows a picture of a RF module composed of 4 RF cavities  
 1017 working in a superconducting state at 4.5 K; also is showed a representation of the

1018 accelerating electric field that accelerates the protons in the bunch.

1019

1020 While protons are accelerated in one section of the LHC ring, where the RF cavities  
 1021 are located, in the rest of their path they have to be kept in the curved trajectory  
 1022 defined by the LHC ring. Technically, LHC is not a perfect circle; RF, injection, beam  
 1023 dumping, beam cleaning and sections before and after the experimental points where  
 1024 protons collide are all straight sections. In total, there are 8 arcs 2.45 Km long each  
 1025 and 8 straight sections 545 m long each. In order to curve the proton's trajectory in  
 1026 the arc sections, superconducting dipole magnets are used.

1027

1028 Inside the LHC ring, there are two proton beams traveling in opposite directions in  
 1029 two separated beam pipes; the beam pipes are kept at ultra-high vacuum ( $\sim 10^{-9}$   
 1030 Pa) to ensure that there are no particles that interact with the proton beams. The  
 1031 superconducting dipole magnets used in LHC are made of a NbTi alloy, capable of  
 1032 transporting currents of about 12000 A when cooled at a temperature below 2K using  
 1033 liquid helium (see Figure 3.5).

1034

1035 Protons in the arc sections of LHC feel a centripetal force exerted by the dipole  
 1036 magnets which is perpendicular to the beam trajectory; The magnitude of magnetic  
 1037 field needed can be found assuming that protons travel at  $v \approx c$ , using the standard  
 1038 values for proton mass and charge and the LHC radius, as

$$F_m = \frac{mv^2}{r} = qBv \quad \rightarrow B = 8.33T \quad (3.1)$$

1039 which is about 100000 times the Earth's magnetic field. A representation of the mag-  
 1040 netic field generated by the dipole magnets is shown on the bottom left side of Figure

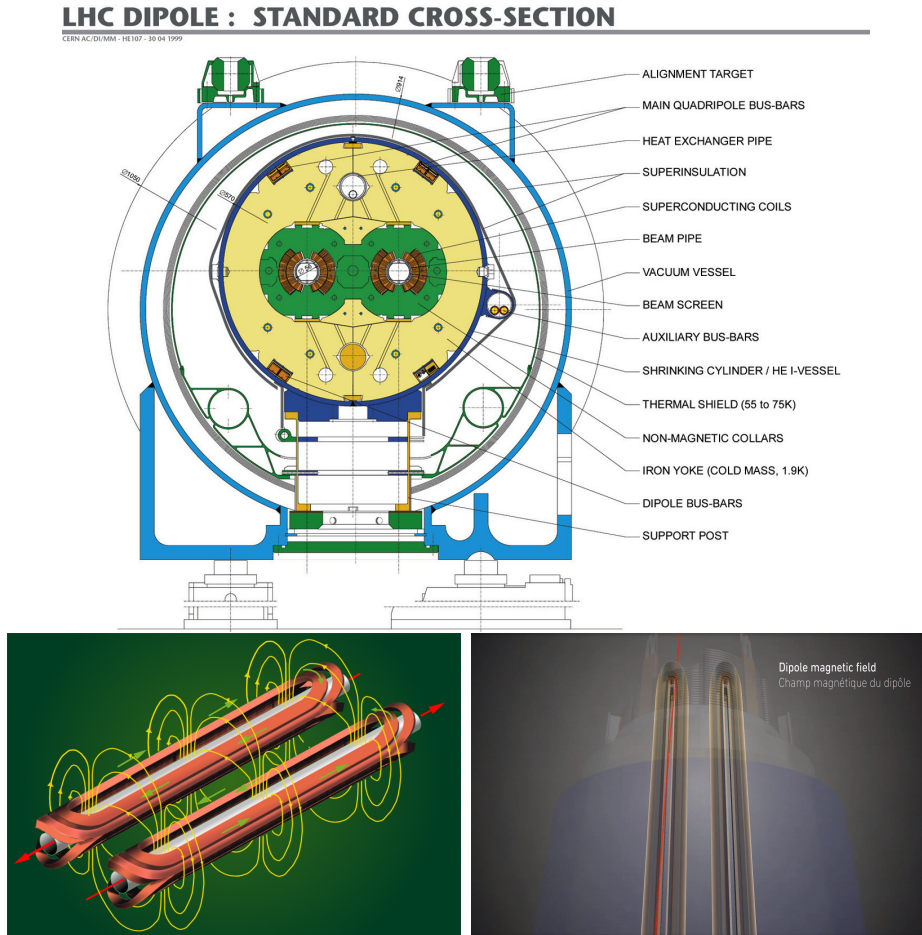


**Figure 3.5:** Top: LHC dipole magnet transverse view; cooling, shielding and mechanical support are indicated. Bottom left: Magnetic field generated by the dipole magnets; note that the direction of the field inside one beam pipe is opposite with respect to the other beam pipe which guarantee that both proton beams are curved in the same direction towards the center of the ring. The effect of the dipole magnetic field on the proton beam is represented on the bottom right side [59, 62, 63].

- 1041 3.5. The bending effect of the magnetic field on the proton beam is shown on the  
 1042 bottom right side of Figure 3.5. Note that the dipole magnets are not curved; the  
 1043 arc section of the LHC ring is composed of straight dipole magnets of about 15 m.  
 1044 In total there are 1232 dipole magnets along the LHC ring.
- 1045
- 1046 In addition to bending the beam trajectory, the beam has to be focused so it stays

1047 inside the beam pipe. The focusing is performed by quadrupole magnets installed in  
 1048 a different straight section; in total 858 quadrupole magnets are installed along the  
 1049 LHC ring. Other effects like electromagnetic interaction among bunches, interaction  
 1050 with electron clouds from the beam pipe, the gravitational force on the protons, dif-  
 1051 ferences in energy among protons in the same bunch, among others, are corrected  
 1052 using sextupole and other magnetic multipoles.

1053

1054 The two proton beams inside the LHC ring are made of bunches with a cylindrical  
 1055 shape of about 7.5 cm long and about 1 mm in diameter; when bunches are close  
 1056 to the collision point (CP), the beam is focused up to a diameter of about 16  $\mu\text{m}$  in  
 1057 order to maximize the number of collisions per unit area and per second, known as  
 1058 luminosity ( $L$ ). Luminosity can be calculated using

$$L = fn \frac{N_1 N_2}{4\pi\sigma_x\sigma_y} \quad (3.2)$$

1059 where  $f$  is the revolution frequency,  $n$  is the number of bunches per beam,  $N_1$  and  
 1060  $N_2$  are the numbers of protons per bunch ( $1.5 \times 10^{11}$ ),  $\sigma_x$  and  $\sigma_y$  are the gaussian  
 1061 transverse sizes of the bunches. The expected luminosity is about

$$f = \frac{v}{2\pi r_{LHC}} \approx \frac{3 \times 10^8 \text{ m/s}}{27 \text{ km}} \approx 11.1 \text{ kHz},$$

$$n = 2808$$

$$N_1 = N_2 = 1.5 \times 10^{11}$$

$$\sigma_x = \sigma_y = 16 \mu\text{m}$$

1062

$$L = 1.28 \times 10^{34} \text{ cm}^{-2} \text{ s}^{-1} = 1.28 \times 10^{-5} \text{ fb}^{-1} \text{ s}^{-1} \quad (3.3)$$

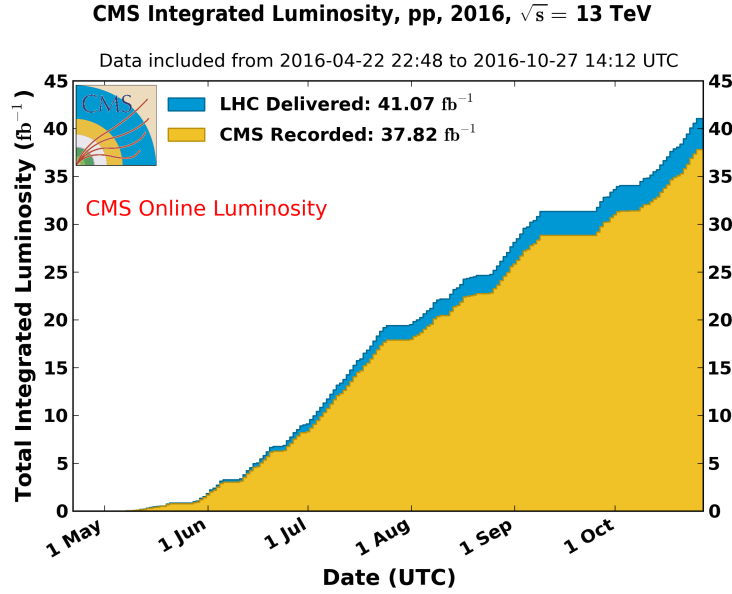


**Figure 3.6:** Integrated luminosity delivered by LHC and recorded by CMS during 2016. The difference between the delivered and the recorded luminosity is due to fails and issues occurred during the data taking in the CMS experiment [64].

1063 Luminosity is a fundamental aspect of LHC given that the bigger luminosity the  
 1064 bigger number of collisions, which means that for processes with a very small cross  
 1065 section the number of expected occurrences is increased and so the chances of being  
 1066 detected. The integrated luminosity, i.e., the total luminosity, collected by the CMS  
 1067 experiment during 2016 is shown in Figure 3.6; the data analyzed in this thesis cor-  
 1068 responds to an integrated luminosity of  $35.9 \text{ fb}^{-1}$  at a center of mass-energy  $\sqrt{s} = 13$   
 1069 TeV.

1070

1071 A way to increase  $L$  is increasing the number of bunches in the beam. Currently, the  
 1072 separation between two consecutive bunches in the beam is 7.5 m which corresponds  
 1073 to a time separation of 25 ns. In the full LHC ring the allowed number of bunches is  
 1074  $n = 27\text{km}/7.5\text{m} = 3600$ ; however, there are some gaps in the bunch pattern intended  
 1075 for preparing the dumping and injection of the beam, thus, the proton beams are

1076 composed of 2808 bunches.

1077

1078 Once the proton beams reach the desired energy, they are brought to cross each other  
 1079 producing proton-proton collisions. The bunch crossing happens in precise places  
 1080 where the four LHC experiments are located, as seen in the top of Figure 3.7. In  
 1081 2008, the first set of collisions involved protons with  $\sqrt{s} = 7$  TeV; the energy was  
 1082 increased to 8 TeV in 2012 and to 13 TeV in 2015.

1083

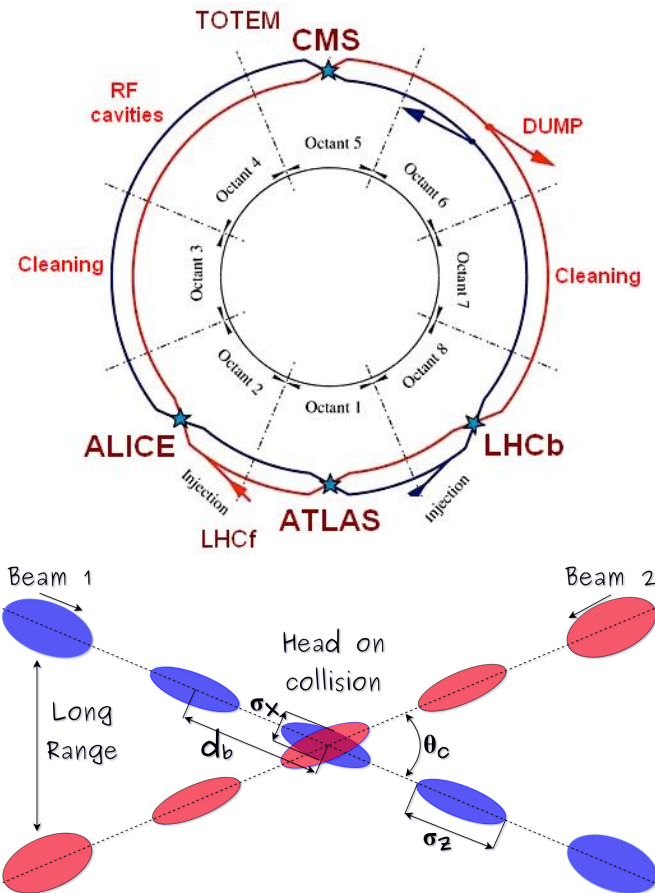


**Figure 3.7:** Top: LHC interaction points. Bunch crossing occurs where the LHC experiments are located [65]. Sections indicated as cleaning are dedicated to collimate the beam in order to protect the LHC ring from collisions with protons in very spreaded bunches. Bottom: bunch crossing scheme. Since the bunch crossing is not perfectly head-on, the luminosity is reduced in a factor of 17%; adapted from Reference [77].

1084 CMS and ATLAS experiments, which are multi-purpose experiments, are enabled  
 1085 to explore physics in any of the collision modes. LHCb experiment is optimized  
 1086 to explore bottom quark physics, while ALICE is optimized for heavy ion collisions  
 1087 searches; TOTEM and LHCf are dedicated to forward physics studies; MoEDAL (not  
 1088 indicated in the Figure) is intended for monopoles or massive pseudo stable particles  
 1089 searches.

1090

1091 At the CP there are two interesting details that need to be addressed. The first one  
 1092 is that the bunch crossing does not occur head-on but at a small crossing angle  $\theta_c$   
 1093 (280  $\mu$ rad in CMS and ATLAS) as shown in the bottom side of Figure 3.7, affecting  
 1094 the overlapping between bunches; the consequence is a reduction of about 17% in  
 1095 the luminosity (represented by a factor not included in eqn. 3.2). The second one  
 1096 is the occurrence of multiple  $pp$  collisions in the same bunch crossing; this effect is  
 1097 called pile-up (PU). A fairly simple estimation of the PU follows from estimating the  
 1098 probability of collision between two protons, one from each of the bunches in course  
 1099 of collision; it depends roughly on the ratio of proton size and the cross section of the  
 1100 bunch in the interaction point, i.e.,

$$P(pp\text{-}collision) \sim \frac{d_{proton}^2}{\sigma_x \sigma_y} = \frac{(1\text{fm})^2}{(16\mu\text{m})^2} \sim 4 \times 10^{-21} \quad (3.4)$$

1101 however, there are  $N = 1.15 \times 10^{11}$  protons in a bunch, thus the estimated number of  
 1102 collisions in a bunch crossing is

$$PU = N^2 * P(pp\text{-}collision) \sim 50 \text{ } pp\text{-}collision \text{ per bunch crossing}, \quad (3.5)$$

1103 about 20 of those  $pp$  collisions are inelastic. Each collision generates a vertex, but  
 1104 only the most energetic is considered as a primary vertex; the rest are considered

as PU vertices. A multiple  $pp$  collision event in a bunch crossing at CMS is showed in Figure 3.8. Unstable particles outgoing from the primary vertex will eventually decay; this decay vertex is known as a secondary vertex.

1108

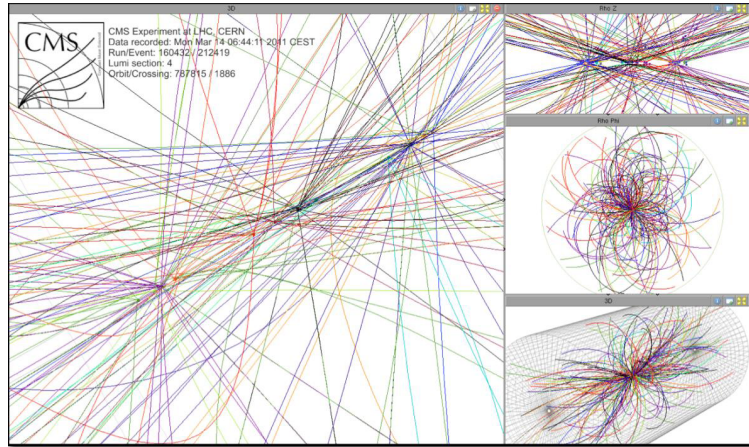


**Figure 3.8:** Multiple  $pp$  collision bunch crossing at CMS. Only the most energetic vertex is considered and the rest are cataloged as PU vertices [66].

1109 Next section presents a description of the CMS detector which it is the detector used  
1110 to collect the data used in this thesis.

### 1111 3.3 The CMS experiment

1112 CMS is a general-purpose detector designed to conduct research in a wide range  
1113 of physics from the standard model to new physics like extra dimensions and dark  
1114 matter. Located at the point 5 in the LHC layout as shown in Figure 3.4, CMS is  
1115 composed of several detection systems distributed in a cylindrical structure; in total,  
1116 CMS weights about 12500 tons in a very compact 21.6 m long and 14.6 m diameter  
1117 cylinder. It was built in 15 separate sections at the ground level and lowered to the  
1118 cavern individually to be assembled. A complete and detailed description of the CMS  
1119 detector and its components is given in Reference [67] on which this section is based

1120 on.

1121

1122 Figure 3.9 shows the layout of the CMS detector. The design is driven by the require-  
 1123 ments on the identification, momentum resolution and unambiguous charge determi-  
 1124 nation of the muons; therefore, a large bending power is provided by the solenoid  
 1125 magnet made of superconducting cable capable to generate a 3.8 T magnetic field.  
 1126 The detection system is composed of (from the innermost to the outermost)

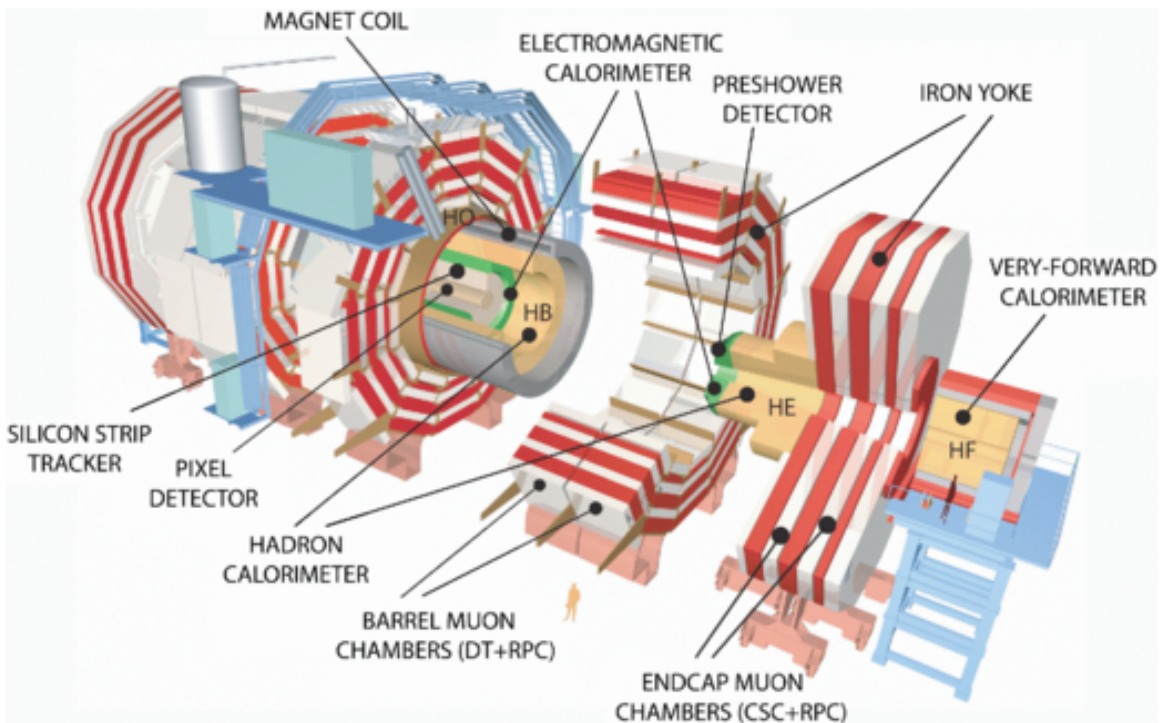


**Figure 3.9:** Layout of the CMS detector. The several subdetectors are indicated. The central region of the detector is referred as the Barrel section while the endcaps are referred as the forward sections. [68].

1127 • Pixel detector.

1128 • Silicon strip tracker.

1129 • Preshower detector.

1130 • Electromagnetic calorimeter.

1131 • Hadronic calorimeter.

1132 • Muon chambers (Barrel and endcap)

1133 The central region of the detector is commonly referred as the barrel section while the  
 1134 endcaps are referred as the forward sections of the detector; thus, each subdetector  
 1135 is composed of a barrel section and a forward section.

### 1136 3.3.1 Coordinate system

1137 The coordinate system used by CMS is centered in the geometrical center of the  
 1138 detector which is the same as the CP as shown in Figure 3.10. The  $z$ -axis is parallel  
 1139 to the beam direction, while the  $Y$ -axis pointing vertically upward, and the  $X$ -axis  
 1140 pointing radially inward toward the center of the LHC.

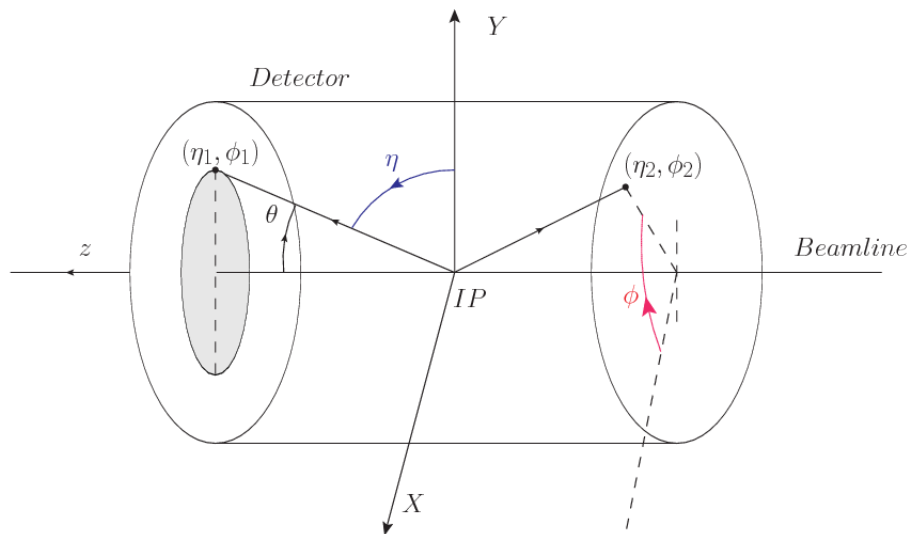


**Figure 3.10:** CMS detector coordinate system.

1141 In addition to the common cartesian and cylindrical coordinate systems, two coor-  
 1142 dinates are of particular utility in particle physics: rapidity ( $y$ ) and pseudorapidity

1143  $(\eta)$ , defined in connection to the polar angle  $\theta$ , energy and longitudinal momentum  
 1144 component (momentum along the  $z$ -axis) according to

$$y = \frac{1}{2} \ln \frac{E + p_z}{E - p_z} \quad \eta = -\ln \left( \tan \frac{\theta}{2} \right) \quad (3.6)$$

1145 Rapidity is related to the angle between the  $XY$ -plane and the direction in which the  
 1146 products of a collision are emitted; it has the nice property that the difference between  
 1147 the rapidities of two particles is invariant with respect to Lorentz boosts along the  $z$ -  
 1148 axis. Thus, data analysis becomes more simple when based on rapidity; however, it is  
 1149 not simple to measure the rapidity of highly relativistic particles, as those produced  
 1150 after  $pp$  collisions. Under the highly relativistic motion approximation,  $y$  can be  
 1151 rewritten in terms of the polar angle, concluding that rapidity is approximately equal  
 1152 to the pseudorapidity defined above, i.e.,  $y \approx \eta$ . Note that  $\eta$  is easier to measure than  $y$   
 1153 given the direct relationship between the former and the polar angle. Angular distance  
 1154 between two objects in the detector ( $\Delta R$ ) is defined in terms of their coordinates  
 1155  $(\eta_1, \phi_1), (\eta_2, \phi_2)$  as

$$\Delta R = \sqrt{(\Delta\eta)^2 - (\Delta\phi)^2} \quad (3.7)$$

### 1156 3.3.2 Pixels detector

1157 The CMS tracking system is designed to provide a precise measurement of the tra-  
 1158 jectory (*track*) followed by the charged particles created after the  $pp$  collisions; also,  
 1159 the precise reconstruction of the primary and secondary origins (*vertices*) is expected  
 1160 in an environment where, each 25 ns, the bunch crossing produce about 20 inelastic  
 1161 collisions and about 1000 particles. An increment in the luminosity is ongoing which  
 1162 implies that the PU will increase accordingly.

1164 The pixel detector was replaced during the 2016-2017 extended year-end technical  
1165 stop, due to the increasingly challenging operating conditions like the higher particle  
1166 flow and more radiation harsh environment, among others. The new one is responding  
1167 as expected, reinforcing its crucial role in the successful way to fulfill the new LHC  
1168 physics objectives after the discovery of the Higgs boson. The last chapter of this  
1169 thesis is dedicated to describe my contribution to the *Forward Pixel Phase 1 upgrade*.

1170

1171 The current pixel detector is composed of 1856 silicon pixel detector modules orga-  
1172 nized in four-barrel layers in the central region and three disks in the forward region;  
1173 it is designed to record efficiently and with high precision, up to  $10\mu\text{m}$  in the  $XY$ -  
1174 plane and  $20\mu\text{m}$  in the  $z$ -direction, the first four space-points (*hits*) near to the CP  
1175 region (see Figure 3.11 left side) in the range  $|\eta| \leq 2.5$ . The first barrel layer is located  
1176 at a radius of 30 mm from the beamline, while the fourth layer is located at a radius  
1177 of 160 mm closer to the strip tracker inner barrel layer (see Section 3.3.3) in order to  
1178 reduce the rate of fake tracks. The high granularity of the detector is represented in  
1179 its about 123 Mpixels, each of size  $100 \times 150\mu\text{m}^2$ , which is almost twice the channels  
1180 of the old detector. The transverse momentum resolution of tracks can be measured  
1181 with a resolution of 1-2% for muons of  $p_T = 100$  GeV.

1182

1183 Some of the improvements with respect to the previous pixel detector include a higher  
1184 average tracking efficiency and lower average fake rate as well as higher track impact  
1185 parameter resolution which is fundamental in order to increase the efficiency in the  
1186 identification of jets originating from b quarks (b-tagging). A significant source of  
1187 improvement comes from the overall reduction in the material budget of the detector  
1188 which results in fewer photon conversions and less multiple scattering from charged  
1189 particles.

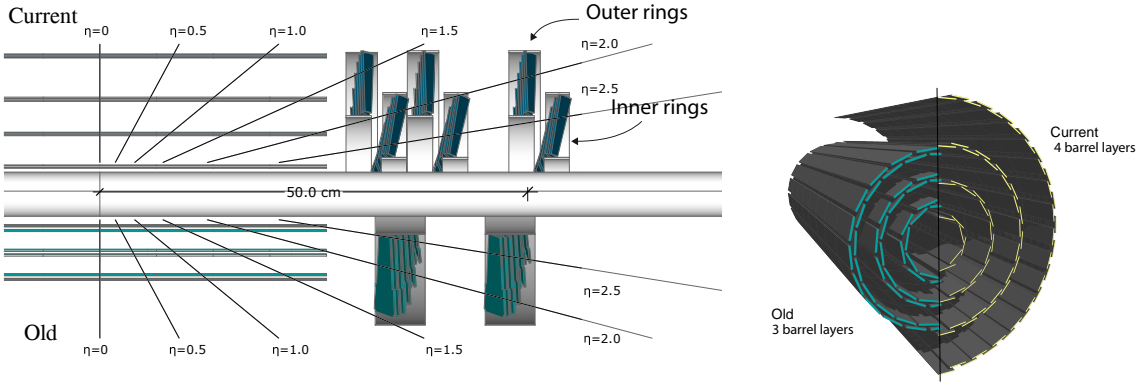


**Figure 3.11:** CMS pixel detector schematic view. Left: layout comparing the layers and disks in the old and current pixel detectors. Right: Transverse-oblique view comparing the pixel barrel layers in the two [70].

### 1190 3.3.3 Silicon strip tracker

1191 The silicon strip tracker (SST) is the second stage in the CMS tracking system. The  
 1192 top side of Figure 3.12 shows a schematic of the SST. The inner tracker region is com-  
 1193 posed of the tracker inner barrel (TIB) and the tracker inner disks (TID) covering the  
 1194 region  $r < 55$  cm and  $|z| < 118$  cm. The TIB is composed of 4 layers while the TID  
 1195 is composed of 3 disks at each end. The silicon sensors in the inner tracker are 320  
 1196  $\mu\text{m}$  thick, providing a resolution of about 13-38  $\mu\text{m}$  in the  $r\phi$  position measurement.  
 1197

1198 The modules indicated in blue in the schematic view of Figure 3.12 are two modules  
 1199 mounted back-to-back and rotated in the plane of the module by a *stereo* angle of  
 1200 100 mrad; the hits from these two modules, known as *stereo hits*, are combined to  
 1201 provide a measurement of the second coordinate ( $z$  in the barrel and  $r$  on the disks)  
 1202 allowing the reconstruction of hit positions in 3-D.  
 1203

1204 The outer tracker region is composed of the tracker outer barrel (TOB) and the  
 1205 tracker endcaps (TEC). The six layers of the TOB offer coverage in the region  $r > 55$

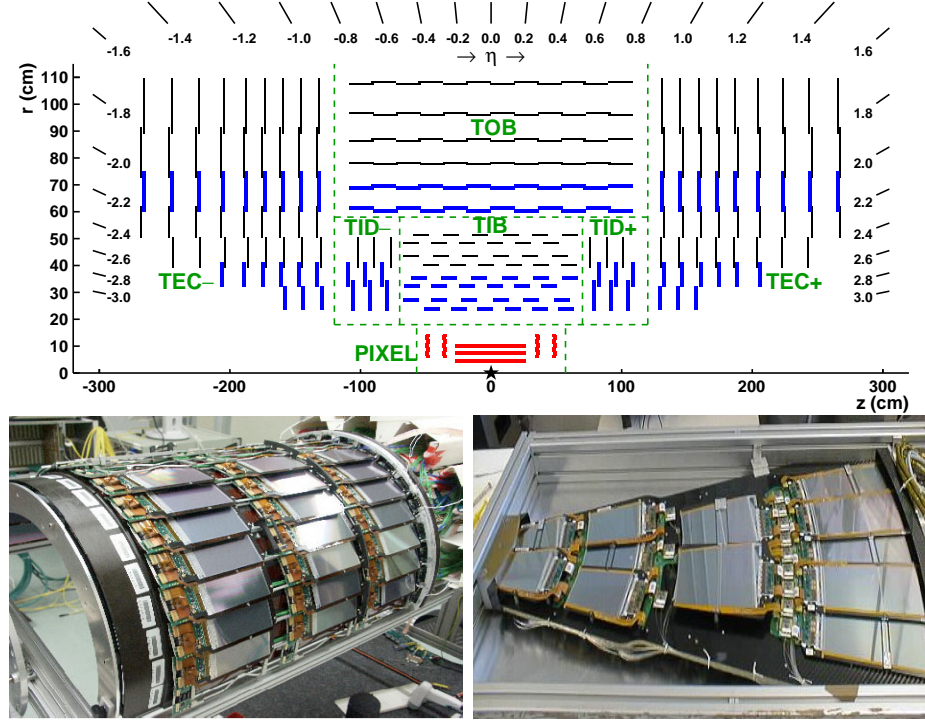


**Figure 3.12:** Top: CMS Silicon Strip Tracker (SST) schematic view. The SST is composed of the tracker inner barrel (TIB), the tracker inner disks (TID), the tracker outer barrel (TOB) and the tracker endcaps (TEC). Each part is made of silicon strip modules; the modules in blue represent two modules mounted back-to-back and rotated in the plane of the module by a stereo angle of 120 mrad in order to provide a 3-D reconstruction of the hit positions. Bottom: pictures of the TIB (left) and TEC (right) modules [71–73].

1206 cm and  $|z| < 118$  cm, while the 9 disks of the TEC cover the region  $124 < |z| < 282$   
 1207 cm. The resolution offered by the outer tracker is about  $13\text{--}38 \mu\text{m}$  in the  $r\phi$  position  
 1208 measurement. The inner four TEC disks use silicon sensors  $320 \mu\text{m}$  thick; those in  
 1209 the TOB and the outer three TEC disks use silicon sensors of  $500 \mu\text{m}$  thickness. The  
 1210 silicon strips run parallel to the  $z$ -axis and the distance between strips varies from 80  
 1211  $\mu\text{m}$  in the inner TIB layers to  $183 \mu\text{m}$  in the inner TOB layers; in the endcaps the  
 1212 wedge-shaped sensors with radial strips, whose pitch range between  $81 \mu\text{m}$  at small  
 1213 radii and  $205 \mu\text{m}$  at large radii.

1214

1215 The whole SST has 15148 silicon modules, 9.3 million silicon strips and cover a total

1216 active area of about  $198 \text{ m}^2$ .

### 1217 3.3.4 Electromagnetic calorimeter

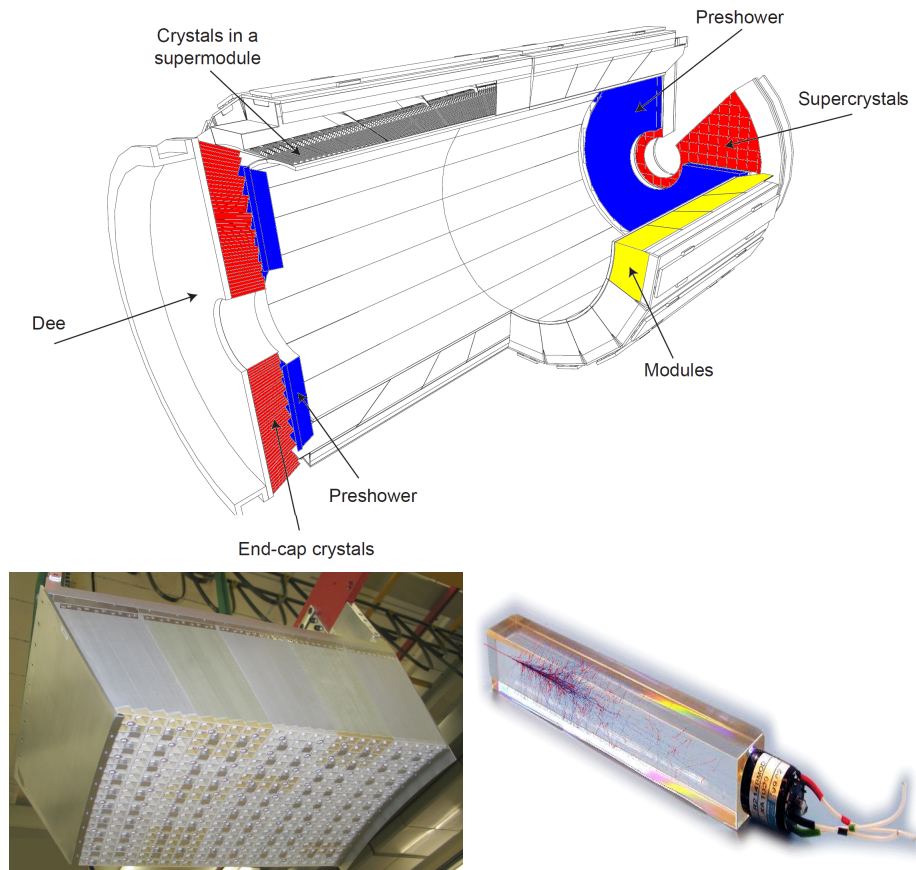


**Figure 3.13:** Top: CMS ECAL schematic view. Bottom: Module equipped with the crystals (left); ECAL crystal(right).

1218 The CMS electromagnetic calorimeter (ECAL) is designed to measure the energy of  
1219 electrons and photons. It is composed of 75848 lead tungstate crystals which have a  
1220 short radiation length (0.89 cm) and fast response, since 80% of the light is emitted  
1221 within 25 ns; however, they are combined with Avalanche photodiodes (APDs) as  
1222 photodetectors given that crystals themselves have a low light yield ( $30\gamma/\text{MeV}$ ). A

1223 schematic view of the ECAL is shown in Figure 3.13.

1224

1225 Energy is measured when electrons and photons are absorbed by the crystals which  
 1226 generates an electromagnetic *shower*, as seen in bottom right picture of the Figure  
 1227 3.13; the shower is seen as a *cluster* of energy which depending on the amount of en-  
 1228 ergy deposited can involve several crystals. The ECAL barrel (EB) covers the region  
 1229  $|\eta| < 1.479$ , using crystals of depth of 23 cm and  $2.2 \times 2.2 \text{ cm}^2$  transverse section;  
 1230 the ECAL endcap (EE) covers the region  $1.479 < |\eta| < 3.0$  using crystals of depth  
 1231 22 cm and transverse section of  $2.86 \times 2.86 \text{ cm}^2$ ; the photodetectors used are vacuum  
 1232 phototriodes (VPTs). Each EE is divided in two structures called *Dees*.

1233

1234 In front of the EE, it is installed the preshower detector (ES) which covers the region  
 1235  $1.653 < |\eta| < 2.6$ . The ES provides a precise measurement of the position of electro-  
 1236 magnetic showers, which allows to distinguish electrons and photons signals from  $\pi^0$   
 1237 decay signals. The ES is composed of a layer of lead absorber followed by a layer of  
 1238 plastic scintillators

### 1239 3.3.5 Hadronic calorimeter

1240 Hadrons are not absorbed by the ECAL but by the hadron calorimeter (HCAL),  
 1241 which is made of a combination of alternating brass absorber layers and silicon photo-  
 1242 multiplier(SiPM) layers; therefore, particles passing through the scintillator material  
 1243 produce showers, as in the ECAL, as a result of the inelastic scattering of the hadrons  
 1244 with the detector material. Since the particles are not absorbed in the scintillator,  
 1245 their energy is sampled; therefore the total energy is not measured but estimated from  
 1246 the energy clusters, which reduce the resolution of the detector. Brass was chosen

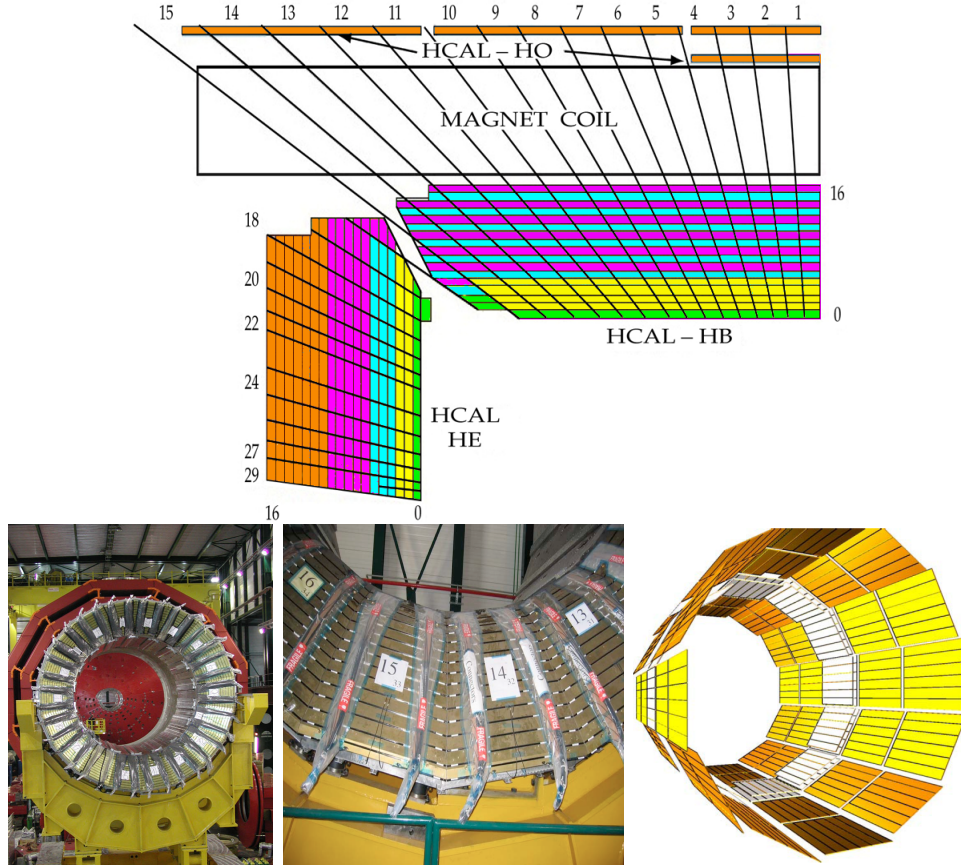


**Figure 3.14:** Top: CMS HCAL schematic view, the colors indicate the layers that are grouped into the same readout channels. Bottom: picture of a section of the HB; the absorber material is the golden region and scintillators are placed in between the absorber material (left and center). Schematic view of the HO (right). [74,75]

as the absorber material due to its short interaction length ( $\lambda_I = 16.42\text{cm}$ ) and its non-magnetivity. Figure 3.14 shows a schematic view of the CMS HCAL.

1249

1250 The HCAL is divided into four sections; the Hadron Barrel (HB), the Hadron Outer  
 1251 (HO), the Hadron Endcap (HE) and the Hadron Forward (HF) sections. The HB  
 1252 covers the region  $0 < |\eta| < 1.4$ , while the HE covers the region  $1.3 < |\eta| < 3.0$ . The HF,  
 1253 made of quartz fiber scintillator and steel as absorption material, covers the forward  
 1254 region  $3.0 < |\eta| < 5.2$ . Both the HB and HF are located inside the solenoid. The HO

is placed outside the magnet as an additional layer of scintillators with the purpose of measure the energy tails of particles passing through the HB and the magnet (see Figure 3.14 top and bottom right). The upgrades made to the HCAL during the technical stop 2016-2017 consisted in the replacement of the photo transducer, in order to improve the efficiency.

### 3.3.6 Superconducting solenoid magnet

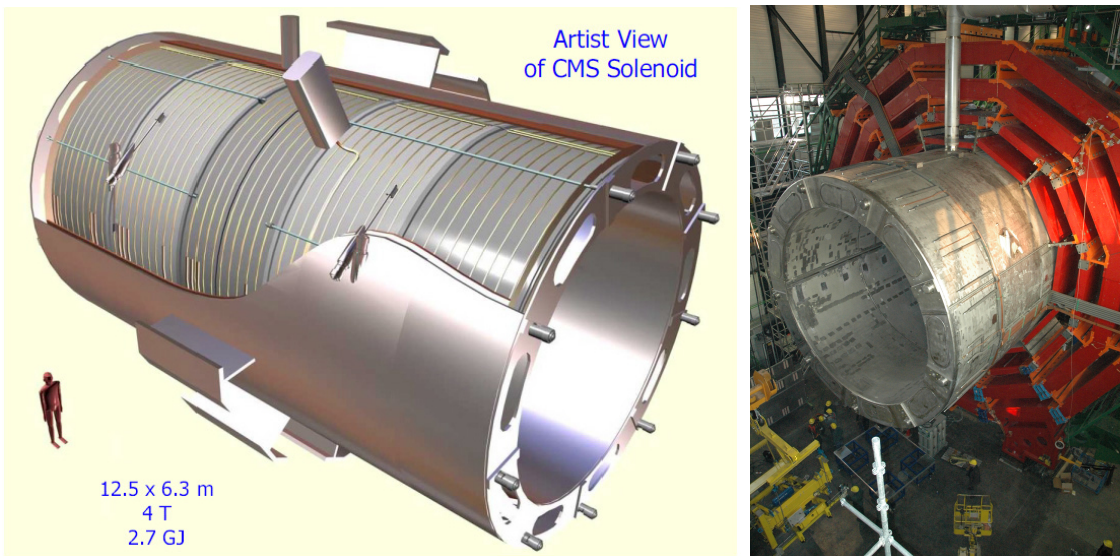


**Figure 3.15:** Artistic representation of the CMS solenoid magnet(left). The magnet is supported on an iron yoke (right) which also serves as the house of the muon detector and as mechanical support for the whole CMS detector [69].

The superconducting magnet installed in the CMS detector is designed to provide an intense and highly uniform magnetic field in the central part of the detector. In fact, the tracking system takes advantage of the bending power of the magnetic field to measure with precision the momentum of the particles that traverse it; the unambiguous determination of the sign for high momentum muons was a driven principle during the design of the magnet. The magnet has a diameter of 6.3 m, a length of 12.5 m and a cold mass of 220 t; the generated magnetic field reaches a strength of 3.8T.

1268 Since it is made of Ni-Tb superconducting cable it has to operate at a temperature  
 1269 of 4.7 K by using a helium cryogenic system; the current circulating in the cables  
 1270 reaches 18800 A under normal running conditions. The left side of Figure 3.15 shows  
 1271 an artistic view of the CMS magnet, while the right side shows a transverse view of  
 1272 the cold mass where the winding structure is visible.

1273

1274 The yoke (see Figure 3.15), composed of 5 barrel wheels and 6 endcap disks made  
 1275 of iron, serves not only as the media for magnetic flux return but also provides the  
 1276 house for the muon detector system and structural stability to the full detector.

### 1277 3.3.7 Muon system

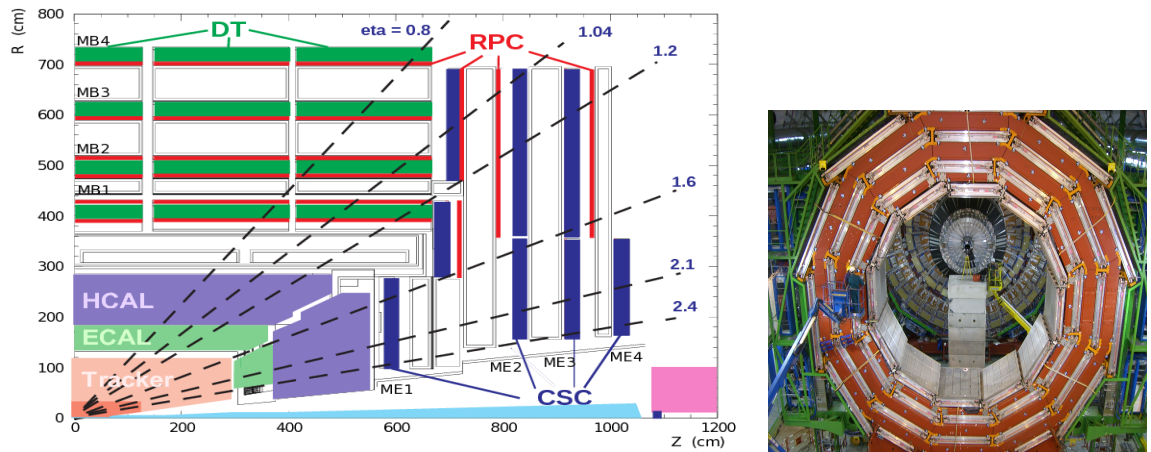


**Figure 3.16:** Left: CMS muon system schematic view; Right: one of the yoke rings with the muon DTs and RPCs installed; in the back it is possible to see the muon endcap [76].

1278 Muons are the only charged particles able to pass through all the CMS detector due  
 1279 to their low ionization energy loss; thus, muons can be separated easily from the  
 1280 high amount of particles produced in a  $pp$  collision. Also, muons are expected to be  
 1281 produced in the decay of several new particles; therefore, a good detection of muons

1282 was on the leading principles when designing the CMS detector.

1283

1284 The CMS muon detection system (muon spectrometer) is embedded in the return  
 1285 yoke as seen in Figure 3.16. It is composed of three different detector types, the drift  
 1286 tube chambers (DT), Cathode strip chambers (CSC), and resistive plate chambers  
 1287 (RPC); DT are located in the central region  $\eta < 1.2$  arranged in four layers of drift  
 1288 chambers filled with an Ar/CO<sub>2</sub> gas mixture.

1289

1290 The muon endcaps are made of CSCs covering the region  $\eta < 2.4$  and filled with a  
 1291 mixture of Ar/CO<sub>2</sub>/CF<sub>4</sub>. The reason behind using a different detector type lies on  
 1292 the different conditions in the forward region like the higher muon rate and higher  
 1293 residual magnetic field compared to the central region.

1294

1295 The third type of detector used in the muon system is a set of four disks of RPCs  
 1296 working in avalanche mode. The RPCs provide good spatial and time resolutions.  
 1297 The track of  $high - p_T$  muon candidates is built combining information from the  
 1298 tracking system and the signal from up to six RPCs and four DT chambers.

1299 The muon tracks are reconstructed from the hits in the several layers of the muon  
 1300 system.

### 1301 **3.3.8 CMS trigger system**

1302 Under normal conditions, CMS expects  $pp$  collisions every 25 ns, i.e., an interaction  
 1303 rate of 40 MHz for which it is not possible to store the recorded data in full. In order  
 1304 to handle this high event rate data, an online event selection, known as triggering, is  
 1305 performed; triggering reduce the event rate to 100 Hz for storage and further offline

1306 analysis.

1307

1308 The trigger system starts with a reduction of the event rate to 100 kHz in the so-  
 1309 called *level 1 trigger (L1)*. L1 is based on dedicated programmable hardware like  
 1310 Field Programmable Gate Arrays (FPGAs) and Application Specific Integrated Cir-  
 1311 cuits (ASICs), partly located in the detector itself; another portion is located in the  
 1312 CMS under-ground cavern. Hit patterns information from the muon chambers and  
 1313 the energy deposits in the calorimeter are used to decide if an event is accepted or  
 1314 rejected, according to selection requirements previously defined, which reflect the in-  
 1315 teresting physics processes. Figure 3.17 shows the L1 trigger architecture.

1316

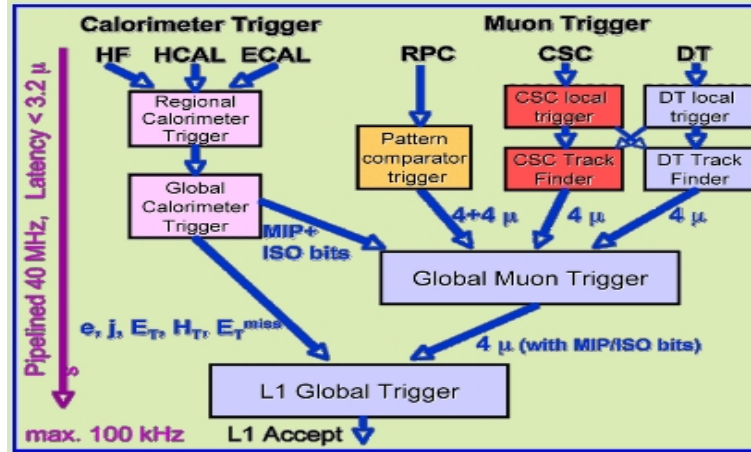


**Figure 3.17:** CMS Level-1 trigger architecture [77].

1317 The second stage in the trigger system is called *high-level trigger (HLT)*; events ac-  
 1318 cepted by L1 are passed to HLT in order to make an initial reconstruction of them.  
 1319 HLT is software based and runs on a dedicated server farm, using selection algo-  
 1320 rithms and high-level object definitions; the event rate at HLT is reduced to 100 Hz.  
 1321 The first HLT stage takes information from the muon detectors and the calorimeters  
 1322 to make the initial object reconstruction; in the next HLT stage, information from

1323 the pixel and strip detectors is used to do first fast-tracking and then full tracking  
1324 online. This initial object reconstruction is used in further steps of the trigger system.

1325

1326 Events and preliminary reconstructed physics objects from HLT are sent to be fully  
1327 reconstructed at the CERN computing center. Again, the pixel detector information  
1328 provides high-quality seeds for the track reconstruction algorithm offline, primary ver-  
1329 tex reconstruction, electron and photon identification, muon reconstruction,  $\tau$  iden-  
1330 tification, and b-tagging. After full reconstruction, data sets are made available for  
1331 offline analyses.

1332

1333 During the 2016-2017 technical stop, the L1 system was updated in order to improve  
1334 the physics object identification by improving the algorithms and accounting for the  
1335 increasing pile-up scenario.

### 1336 **3.3.9 CMS computing**

1337 After the data, coming from the experiment, are processed at several levels, they have  
1338 to be stored and made available for further analysis; in order to cope all the tasks  
1339 implied in the offline data processing, like transfer, simulation, reconstruction and  
1340 reprocessing, among others, a big computing power is required. The CMS computing  
1341 system is based on the distributed architecture concept, where users of the system  
1342 and physical computer centers are distributed worldwide and interconnected by high-  
1343 speed networks.

1344 The worldwide LHC computing grid (WLCG) is the mechanism used to provide that  
1345 distributed environment. WLCG is a tiered structure connecting computing centers  
1346 around the world, which provides the necessary storage and computing facilities. The

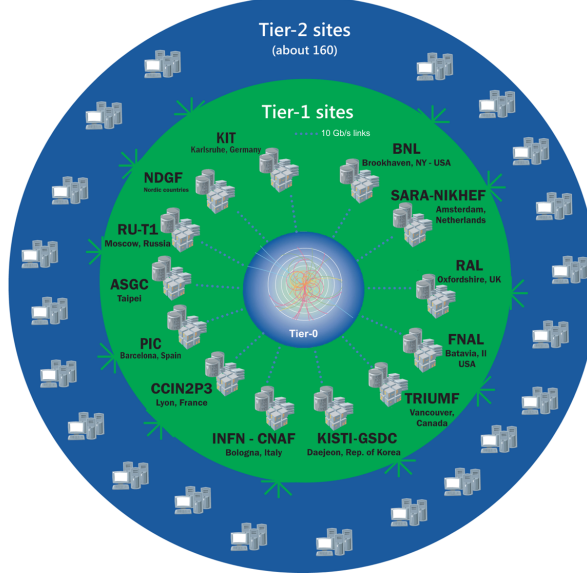


**Figure 3.18:** WLCG structure. The primary computer centers (Tier-0) are located at CERN (data center) and at the Wigner datacenter in Budapest. Tier-1 is composed of 13 centers and Tier-2 is composed of about 160 centers. [78].

1347 primary computing centers of the WLCG are located at the CERN and the Wigner  
 1348 datacenter in Budapest and are known as Tier-0 as shown in Figure 3.18. The main  
 1349 responsibilities for each tier level are [78]

- 1350     • **Tier-0:** initial reconstruction of recorded events and storage of the resulting  
       1351       datasets, the distribution of raw data to the Tier-1 centers.
- 1352     • **Tier-1:** provide storage capacity, support for the Grid, safe-keeping of a pro-  
       1353       portional share of raw and reconstructed data, large-scale reprocessing and safe-  
       1354       keeping of corresponding output, generation of simulated events, distribution  
       1355       of data to Tier 2s, safe-keeping of a share of simulated data produced at these  
       1356       Tier 2s.
- 1357     • **Tier-2:** store sufficient data and provide adequate computing power for specific  
       1358       analysis tasks, provide analysis requirements and proportional share of simu-  
       1359       lated event production and reconstruction.

1360 Aside from the general computing strategy to manage the huge amount of data pro-  
1361 duced by experiments, CMS uses a framework to perform a variety of processing,  
1362 selection and analysis tasks. The central concept of the CMS data model referred to  
1363 as *event data model* (EDM) is the *Event*; therefore, an event is the unit that contains  
1364 the information from a single bunch crossing as well as any data derived from that  
1365 information like the reconstructed objects, the details under which additional data  
1366 are derived.

1367

1368 Events are passed as the input to the *physics modules* that obtain information from  
1369 them and create new one; for instance, *event data producers* add new data into the  
1370 events, *analyzers* produce an information summary from an event set, *filters* perform  
1371 selection and triggering.

1372

1373 CMS uses several event formats with different levels of detail and precision

1374 • **Raw format:** events in this format contain the full recorded information from  
1375 the detector as well as trigger decision and other metadata. An extended version  
1376 of raw data is used to store information from the CMS Monte Carlo simulation  
1377 tools. Raw data are stored permanently, occupying about 2MB/event

1378 • **RECO format:** events in this format correspond to raw data that have been  
1379 submitted to reconstruction algorithms like primary and secondary vertex re-  
1380 construction, particle ID, track-finding. RECO events contain physical objects  
1381 and all the information used to reconstruct them; average size is about 0.5  
1382 MB/event.

1383 • **AOD format:** Analysis Object Data (AOD) is the data format used in the  
1384 physics analyses given that it contains the parameters describing the high-level

1385        physics objects in addition to enough information to allow a kinematic refitting if  
 1386        needed. AOD events are filtered versions of the RECO events to which skimming  
 1387        or other kind processes have been applied. Requires about 100 kB/event.

1388        • **Non-event data** are data needed to interpret and reconstruct events. Some  
 1389        of the non-event data used by CMS contains information about the detector  
 1390        contraction and condition data like calibrations, alignment, and detector status.

1391        Figure 3.19 shows the data flow scheme between CMS detector and hardware tiers.

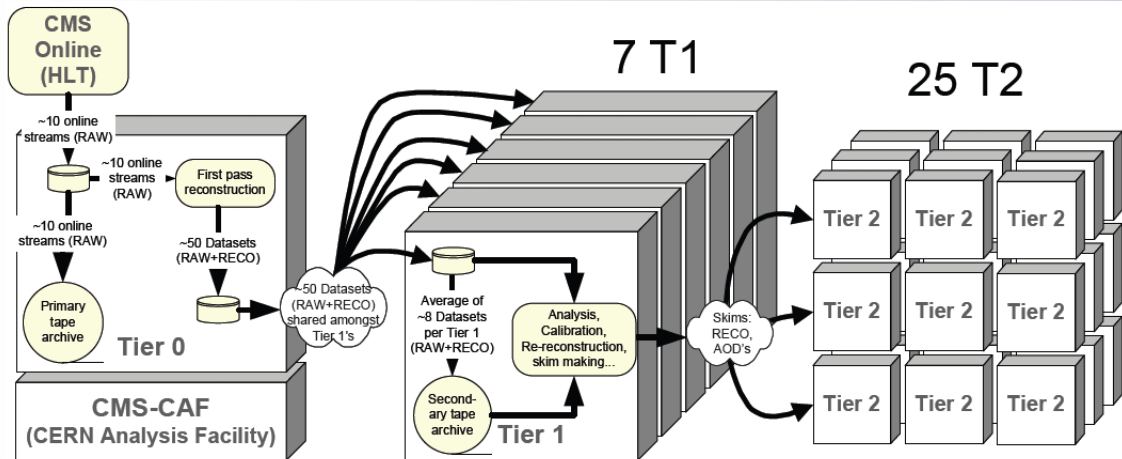


**Figure 3.19:** Data flow from CMS detector through hardware Tiers.

1392        The whole collection of software built as a framework is referred to as *CMSSW*. This  
 1393        framework provides the services needed by the simulation, calibration and alignment,  
 1394        and reconstruction modules that process event data, so that physicists can perform  
 1395        analysis. The CMSSW event processing model is composed of one executable, called  
 1396        cmsRun, and several plug-in modules which contains all the tools (calibration, recon-  
 1397        struction algorithms) needed to process an event. The same executable is used for  
 1398        both detector and Monte Carlo data [79].

1399 **Chapter 4**

1400 **Event generation, simulation and  
1401 reconstruction**

1402 The process of analyzing data recorded by the CMS experiment involves several stages  
1403 where the data are processed in order to interpret the information provided by all  
1404 the detection systems; in those stages, the particles produced after the  $pp$  collision  
1405 are identified by reconstructing their trajectories and measuring their features. In  
1406 addition, the SM provides a set of predictions that have to be compared with the  
1407 experimental results; however, in most of the cases, theoretical predictions are not  
1408 directly comparable to experimental results due to the diverse source of uncertainties  
1409 introduced by the experimental setup and theoretical approximations, among others.

1410

1411 The strategy to face these conditions consists in using statistical methods imple-  
1412 mented in computational algorithms to produce numerical results that can be con-  
1413 trasted with the experimental results. These computational algorithms are commonly  
1414 known as Monte Carlo (MC) methods and, in the case of particle physics, they are  
1415 designed to apply the SM rules and produce predictions about the physical observ-

ables measured in the experiments. Since particle physics is governed by quantum mechanics principles, predictions are not allowed from single events; therefore, a high number of events are *generated* and predictions are produced in the form of statistical distributions for the observables. Effects of the detector presence are included in the predictions by introducing simulations of the detector itself.

1421

1422 This chapter presents a description of the event generation strategy and the tools  
 1423 used to perform the detector simulation and physics objects reconstruction. A com-  
 1424 prehensive review of event generators for LHC physics can be found in Reference [80]  
 1425 on which this chapter is based.

## 1426 4.1 Event generation

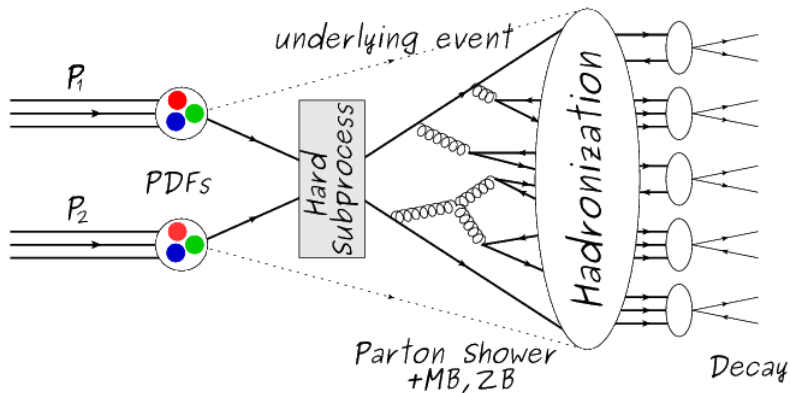


**Figure 4.1:** Event generation process. The actual interaction is generated in the hard subprocess. The parton shower describes the evolution of the partons from the hard subprocess. Modified from Reference [81].

1427 The event generation is intended to create events that mimic the behavior of actual  
 1428 events produced in collisions; they obey a sequence of steps from the particles collision  
 1429 hard process to the decay process into the final state. Figure 4.1 shows a schematic  
 1430 view of the event generation process; the fact that the full process can be treated as

1431 several independent steps is motivated by the QCD factorization theorem.

1432

1433 Generation starts by taking into account the PDFs of the incoming particles. Event  
 1434 generators offer the option to chose from several PDF sets depending on the particu-  
 1435 lar process under simulation<sup>1</sup>; in the following,  $pp$  collisions will be considered. The  
 1436 *hard subprocess* describes the actual interaction between partons from the incoming  
 1437 protons; it is represented by the matrix element connecting the initial and final states  
 1438 of the interaction. Normally, the matrix element can be written as a sum over Feyn-  
 1439 man diagrams and consider interferences between terms in the summation. During  
 1440 the generation of the hard subprocess, the production cross section is calculated.

1441

1442 The order to which the cross section is calculated depends on the order of the Feyn-  
 1443 man diagrams involved in the calculation; therefore, radiative corrections are included  
 1444 by considering a higher order Feynman diagrams where QCD radiation dominates.  
 1445 Currently, cross sections calculated to LO do not offer a satisfactory description of the  
 1446 processes, i.e., the results are only reliable for the shape of distributions; therefore,  
 1447 NLO calculations have to be performed with the implication that the computing time  
 1448 needed is highly increased.

1449

1450 The final parton content of the hard subprocess is subjected to the *parton shower*  
 1451 which generates the gluon radiation. Parton shower evolves the partons, i.e., glouns  
 1452 split into quark-antiquark pairs and quarks with enough energy radiate gluons giv-  
 1453 ing rise to further parton multiplication, following the DGLAP (Dokshitzer-Gribov-  
 1454 Lipatov-Altarelli-Parisi) equations. Showering continues until the energy scale is low  
 1455 enough to reach the non-perturbative limit.

---

<sup>1</sup> Tool in Reference [82] allows to plot different PDF sets under customizable conditions.

1456

1457 In the simulation of LHC processes that involve  $b$  quarks, like the single top quark  
 1458 or Higgs associated production, it is needed to consider that the  $b$  quark is heavier  
 1459 than the proton; hence, the QCD interaction description is made in two different  
 1460 schemes [83]

1461 • four-flavor (4F) scheme.  $b$  quarks appear only in the final state because they  
 1462 are heavier than the proton and therefore they can be produced only from the  
 1463 splitting of a gluon into pairs or singly in association with a  $t$  quark in high  
 1464 energy-scale interactions; furthermore, during the simulation, the  $b$ -PDFs are set  
 1465 to zero. Calculations in this scheme are more complicated due to the presence  
 1466 of the second  $b$  quark but the full kinematics is considered already at LO and  
 1467 therefore the accuracy of the description is better.

1468 • five-flavor (5F) scheme.  $b$  quarks are considered massless, therefore they can  
 1469 appear in both initial and final states since they can now be part of the proton;  
 1470 thus, during the simulation  $b$ -PDFs are not set to zero. In this scheme, calcu-  
 1471 lations are simpler than in the 4F scheme and possible logarithmic divergences  
 1472 are absorbed by the PDFs through the DGLAP evolution.

1473 In this thesis, the  $tHq$  events are generated using the 4F scheme in order to reduce  
 1474 uncertainties, while the  $tHW$  events are generated using the 5F scheme to eliminate  
 1475 LO interference with  $t\bar{t}H$  process [48].

1476

1477 Partons involved in the  $pp$  collision are the focus of the simulation, however, the rest  
 1478 of the partons inside the incoming protons are also affected because the remnants are  
 1479 colored objects; also, multiple parton interactions can occur. The hadronization of  
 1480 the remnants and multiple parton interactions are known as *underlying event* and it

1481 has to be included in the simulation. In addition, multiple  $pp$  collisions in the same  
 1482 bunch crossing (pile-up mentioned in 3.2) occurs, actually in two forms

1483 • *in-time PU* which refers to multiple  $pp$  collision in the bunch crossing but that  
 1484 are not considered as primary vertices.

1485 • *Out-of-time PU* which refers to overlapping  $pp$  collisions from consecutive bunch  
 1486 crossings; this can occur due to the time-delays in the detection systems where  
 1487 information from one bunch crossing is assigned to the next or previous one.

1488 While the underlying event effects are included in generation using generator-specific  
 1489 tools, PU effects are added to the generation by overlaying Minimum-bias (MB) and  
 1490 Zero-bias (ZB) events to the generated events. MB events are inelastic events se-  
 1491 lected by using a loose trigger with as little bias as possible, therefore accepting a  
 1492 large fraction of the overall inelastic event; ZB events correspond to random events  
 1493 recorded by the detector when collisions are likely. MB models in-time PU and ZB  
 1494 models out-of-time PU.

1495

1496 The next step in the generation process is called *hadronization*. Since particles with  
 1497 a net color charge are not allowed to exits isolated, they have to recombine to form  
 1498 bound states. This is precisely the process by which the partons resulting from the  
 1499 parton shower arrange themselves as color singlets to form hadrons. At this step, the  
 1500 energy-scale is low and the strong coupling constant is large, therefore hadronization  
 1501 process is non-perturbative and the evolution of the partons is described using phe-  
 1502 nomenological models. Most of the baryons and mesons produced in the hadronization  
 1503 are unstable and hence they will decay in the detector.

1504

1505 The last step in the generation process corresponds to the decay of the unstable  
 1506 particles generated during hadronization; it is also simulated in the hadronization  
 1507 step, based on the known branching ratios.

## 1508 4.2 Monte Carlo Event Generators.

1509 The event generation described in the previous section has been implemented in  
 1510 several software packages for which a brief description is given.

- 1511 • **PYTHIA 8.** It is a program designed to perform the generation of high energy  
 1512 physics events which describes the collisions between particles such as electrons  
 1513 and protons. Several theories and models are implemented in it, in order to  
 1514 describe physical aspects like hard and soft interaction, parton distributions,  
 1515 initial and final-state parton showers, multiple parton interactions, beam rem-  
 1516 nants, hadronization<sup>2</sup> and particle decay. Thanks to extensive testing, several  
 1517 optimized parametrizations, known as *tunings*, have been defined in order to  
 1518 improve the description of actual collisions to a high degree of precision; for  
 1519 analysis at  $\sqrt{s} = 13$  TeV, the underline event CUETP8M1 tune is employed [85].  
 1520 The calculation of the matrix element is performed at LO which is not enough  
 1521 for the current required level of precision; therefore, pythia is often used for  
 1522 parton shower, hadronization and decays, while other event generators are used  
 1523 to generate the matrix element at NLO.

- 1524 • **MadGraph5\_aMC@NLO.** MadGraph is a matrix element generator which  
 1525 calculates the amplitudes for all contributing Feynman diagrams of a given pro-  
 1526 cess but does not provide a parton shower while MC@NLO incorporates NLO

---

<sup>2</sup> based in the Lund string model [84]

1527 QCD matrix elements consistently into a parton shower framework; thus, Mad-  
 1528 Graph5\_aMC@NLO, as a merger of the two event generators MadGraph5 and  
 1529 aMC@NLO, is an event generator capable to calculate tree-level and NLO cross  
 1530 sections and perform the matching of those with the parton shower. It is one of  
 1531 the most frequently used matrix element generators; however, it has the partic-  
 1532 ular feature of the presence of negative event weights which reduce the number  
 1533 of events used to reproduce the properties of the objects generated [86].

1534

1535 • **POWHEG.** It is an NLO matrix element generator where the hardest emis-  
 1536 sion of color charged particles is generated in such a way that the negative event  
 1537 weights issue of MadGraph5\_aMC@NLO is overcome; however, the method re-  
 1538 quires an interface with  $p_T$ -ordered parton shower or a parton shower generator  
 1539 where this highest emission can be vetoed in order to avoid double counting of  
 1540 this highest-energetic emission. PYTHIA is a commonly matched to POWHEG  
 1541 event generator [87].

1542 Events resulting from the whole generation process are known as MC events.

### 1543 4.3 CMS detector simulation.

1544 After generation, MC events contain the physics of the collisions but they are not  
 1545 ready to be compared to the events recorded by the experiment since these recorded  
 1546 events correspond to the response of the detection systems to the interaction with  
 1547 the particles traversing them. The simulation of the CMS detector has to be applied  
 1548 on top of the event generation; it is simulated with a MC toolkit for the simulation  
 1549 of particles passing through matter called Geant4 which is also able to simulate the

1550 electronic signals that would be measured by all detectors inside CMS.

1551

1552 The simulation takes the generated particles contained in the MC events as input,  
1553 makes them pass through the simulated geometry, and models physics processes that  
1554 particles experience during their passage through matter. The full set of results from  
1555 particle-matter interactions corresponds to the simulated hit which contains informa-  
1556 tion about the energy loss, momentum and position. Particles of the input event are  
1557 called *primary*, while the particles originating from GEANT4-modeled interactions of  
1558 a primary particle with matter are called a *secondary*. Simulated hits are the input  
1559 of subsequent modules that emulate the response of the detector readout system and  
1560 triggers. The output from the emulated detection systems and triggers is known as  
1561 digitization [88,89].

1562

1563 The modeling of the CMS detector corresponds to the accurate modeling of the  
1564 interaction among particles, the detector material, and the magnetic field. This  
1565 simulation procedure includes the following standard steps

1566 • Modeling of the Interaction Region.

1567 • Modeling of the particle passage through the hierarchy of volumes that compose  
1568 CMS detector and of the accompanying physics processes.

1569 • Modeling of the effect of multiple interactions per beam crossing and/or the  
1570 effect of events overlay ( Pile-Up simulation).

1571 • Modeling of the detector's electronics response, signal shape, noise, calibration  
1572 constants (digitization).

1573 In addition to the full simulation, i.e., a detailed detector simulation, a faster simu-  
 1574 lation (FastSim) have been developed, that may be used where much larger statistics  
 1575 are required. In FastSim, detector material effects are parametrized and included in  
 1576 the hits; those hits are used as input of the same higher-level algorithms<sup>3</sup> used to an-  
 1577 alyze the recorded events. In this way, comparisons between fast and full simulations  
 1578 can be performed [91].

1579

1580 After the full detector simulation, the output events can be directly compared to  
 1581 events actually recorded in the CMS detector. The collection of MC events that  
 1582 reproduces the expected physics for a given process is known as MC sample.

## 1583 **4.4 Event reconstruction.**

1584 The CMS experiment use the *particle-flow event reconstruction algorithm (PF)* to do  
 1585 the reconstruction of particles produced in  $pp$  collisions. Next sections will present  
 1586 a basic description of the *Elements* used by PF (tracker tracks, energy clusters, and  
 1587 muon tracks), based in the References [92, 93] where more detailed descriptions can  
 1588 be found.

### 1589 **4.4.1 Particle-Flow Algorithm.**

1590 Each of the several sub detection systems of the CMS detector is dedicated to identify  
 1591 a specific type of particles, i.e., photons and electrons are absorbed by the ECAL  
 1592 and their reconstruction is based on ECAL information; hadrons are reconstructed  
 1593 from clusters in the HCAL while muons are reconstructed from hits in the muon

---

<sup>3</sup> track fitting, calorimeter clustering, b tagging, electron identification, jet reconstruction and calibration, trigger algorithms which will be considered in the next sections

1594 chambers. PF is designed to correlate signals from all the detector layers (tracks and  
 1595 energy clusters) in order to reconstruct and identify each final state particle and its  
 1596 properties as sketched in Figure 4.2.

1597

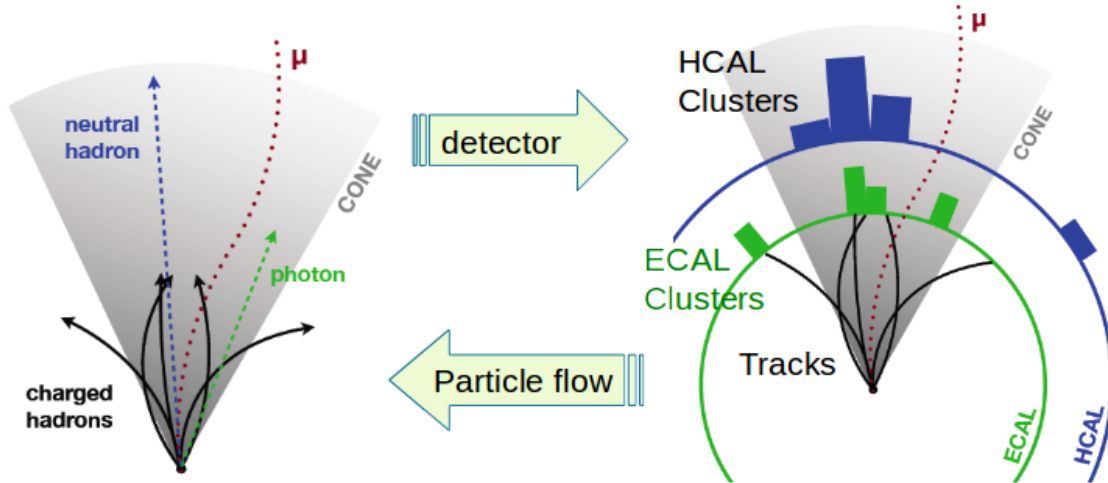


**Figure 4.2:** Particle flow algorithm. Information from the several CMS detection systems is provided as input to the algorithm which then combine it to identify and reconstruct all the particles in the final state and their properties. Reconstruction of simulated events is also performed by providing information from MC samples, detector and trigger simulation [94].

1598 For instance, a charged hadron is identified by a geometrical connection, known as  
 1599 *link*, between one or more calorimeter clusters and a track in the tracker, provided  
 1600 there are no hits in the muon system; combining several measurements allows a better  
 1601 determination of the energy and charge sign of the charged hadron.

### 1602 Charged-particle track reconstruction.

1603 The strategy used by PF in order to reconstruct tracks is called *Iterative Tracking*  
 1604 which occurs in four steps

- 1605 • Seed generation where initial track candidates are found by looking for a combi-  
 1606 nation of hits in the pixel detector, strip tracker, and muon chambers. In total

1607        ten iterations are performed, each one with a different seeding requirement.  
 1608        Seeds are used to estimate the trajectory parameters and uncertainties at the  
 1609        time of the full track reconstruction. Seeds are also considered track candidates.

- 1610        • Track finding using a tracking software known as Combinatorial Track Finder  
               (CTF) [95]. The seed trajectories are extrapolated along the expected flight  
               path of a charged particle, in agreement to the trajectory parameters obtained  
               in the first step, in an attempt to find additional hits that can be assigned to  
               the track candidates.
- 1615        • Track-fitting where the found tracks are passed as input to a module which  
               provides the best estimate of the parameters of each trajectory.
- 1617        • Track selection where track candidates are submitted to a selection which dis-  
               cards those that fail a set of defined quality criteria.

1619        Iterations differ in the seeding configuration and the final track selection as elaborated  
 1620        in References [92, 93]. In the first iteration, high  $p_T$  tracks and tracks produced near  
 1621        to the interaction region are identified and those hits are masked thereby reducing  
 1622        the combinatorial complexity. Next, iterations search for more complicated tracks,  
 1623        like low  $p_T$  tracks and tracks from b hadron decays, which tend to be displaced from  
 1624        the interaction region.

1625        **Vertex reconstruction.**

1626        During the track reconstruction, an extrapolation toward to the calorimeters is per-  
 1627        formed in order to match energy deposits; that extrapolation is performed also toward  
 1628        the beamline in order to find the origin of the track known as *vertex*. The vertex re-  
 1629        construction is performed by selecting from the available reconstructed tracks, those

1630 that are consistent with being originated in the interaction region where  $pp$  collisions  
 1631 are produced. The selection involves a requirement on the number of tracker (pixel  
 1632 and strip) hits and the goodness of the track fit.

1633

1634 Selected tracks are clustered using a *deterministic annealing algorithm* (DA)<sup>4</sup>. A set  
 1635 of candidate vertices and their associated tracks, resulting from the DA, are then fit-  
 1636 ted with an *adaptive vertex fitter* (AVF) to produce the best estimate of the vertices  
 1637 locations.

1638

1639 The  $p_T$  of the tracks associated to a reconstructed vertex is added, squared and used  
 1640 to organize the vertices; the vertex with the highest squared sum is designated as the  
 1641 *primary vertex* (PV) while the rest are designated as PU vertices.

#### 1642 **Calorimeter clustering.**

1643 After traversing the CMS tracker system, electrons, photons and hadrons deposit their  
 1644 energy in the ECAL and HCAL cells. The PF clustering algorithm aims to provide  
 1645 a high detection efficiency even for low-energy particles and an efficient distinction  
 1646 between close energy deposits. The clustering runs independently in the ECAL barrel  
 1647 and endcaps, HCAL barrel and endcaps, and the two preshower layers, following two  
 1648 steps

- 1649     • cells with an energy larger than a given seed threshold and larger than the energy  
   1650       of the neighboring cells are identified as cluster seeds. The neighbor cells are  
   1651       those that either share a side with the cluster seed candidate, or the eight closest  
   1652       cells including cells that only share a corner with the seed candidate.

---

<sup>4</sup> DA algorithm and AVF are described in detail in References [97, 98]

1653       • cells with at least a corner in common with a cell already in the cluster seed  
 1654           and with an energy above a cell threshold are grouped into topological clusters.

1655   Clusters formed in this way are known as *particle-flow clusters*. With this clustering  
 1656   strategy, it is possible to detect and measure the energy and direction of photons and  
 1657   neutral hadrons as well as differentiate these neutral particles from the charged hadron  
 1658   energy deposits. In cases involving charged hadrons for which the track parameters  
 1659   are not determined accurately, for instance, low-quality and high- $p_T$  tracks, clustering  
 1660   helps in the energy measurements.

1661 **Electron track reconstruction.**

1662   Although the charged-particle track reconstruction described above works for elec-  
 1663   trons, they lose a significant fraction of their energy via bremsstrahlung photon radi-  
 1664   ation before reaching the ECAL; thus, the reconstruction performance depends on the  
 1665   ability to measure also the radiated energy. The reconstruction strategy, in this case,  
 1666   requires information from the tracking system and from the ECAL. Bremsstrahlung  
 1667   photons are emitted at similar  $\eta$  values to that of the electron but at different values  
 1668   of  $\phi$ ; therefore, the radiated energy can be recovered by grouping ECAL clusters in a  
 1669    $\eta$  window over a range of  $\phi$  around the electron direction. The group is called ECAL  
 1670   supercluster.

1671

1672   Electron candidates from the track-seeding and ECAL super clustering are merged  
 1673   into a single collection which is submitted to a full electron tracking fit with a  
 1674   Gaussian-sum filter (GSF) [96]. The electron track and its associated ECAL su-  
 1675   percluster form a *particle-flow electron*.

1676 **Muon track reconstruction.**

1677 Given that the CMS detector is equipped with a muon spectrometer capable to iden-  
 1678 tify and measure the momentum of the muons traversing it, the muon reconstruction  
 1679 is not specific to PF; therefore, three different muon types are defined

- 1680     • *Standalone muon.* A clustering on the DTs or CSCs hits is performed to form  
           1681       track segments; those segments are used as seeds for the reconstruction in the  
           1682       muon spectrometer. All DTs, CSCs, and RPCs hits along the muon trajectory  
           1683       are combined and fitted to form the full track. The fitting output is called a  
           1684       *standalone-muon track*.
- 1685     • *Tracker muon.* Each track in the inner tracker with  $p_T$  larger than 0.5 GeV and  
           1686       a total momentum  $p$  larger than 2.5 GeV is extrapolated to the muon system.  
           1687       A *tracker muon track* corresponds to a extrapolated track that matches at least  
           1688       one muon segment.
- 1689     • *Global muon.* When tracks in the inner tracker (inner tracks) and standalone-  
           1690       muon tracks are matched and turn out being compatibles, their hits are com-  
           1691       bined and fitted to form a *global-muon track*.

1692 Global muons sharing the same inner track with tracker muons are merged into a  
 1693 single candidate. PF muon identification uses the muon energy deposits in ECAL,  
 1694 HCAL, and HO associated with the muon track to improve the muon identification.

1695 **Particle identification and reconstruction.**

1696 PF elements are connected by a linker algorithm that tests the connection between any  
 1697 pair of elements; if they are found to be linked, a geometrical distance that quantifies  
 1698 the quality of the link is assigned. Two elements may be linked indirectly through

1699 common elements. Linked elements form *PF blocks* and each PF block may contain  
 1700 elements originating in one or more particles. Links can be established between  
 1701 tracks, between calorimeter clusters, and between tracks and calorimeter clusters.  
 1702 The identification and reconstruction start with a PF block and proceed as follows

1703 • Muons. An *isolated global muon* is identified by evaluating the presence of  
 1704 inner track and energy deposits close to the global muon track in the  $(\eta, \phi)$   
 1705 plane, i.e., in a particular point of the global muon track, inner tracks and  
 1706 energy deposits are sought within a radius of  $\Delta R = 0.3$  (see eqn. 3.7) from the  
 1707 muon track; if they exit and the  $p_T$  of the found track added to the  $E_T$  of the  
 1708 found energy deposit does not exceed 10% of the muon  $p_T$  then the global muon  
 1709 is an isolated global muon. This isolation condition is stringent enough to reject  
 1710 hadrons misidentified as muons.

1711 *Non-isolated global muons* are identified using additional selection requirements  
 1712 on the number of track segments in the muon system and energy deposits along  
 1713 the muon track. Muons inside jets are identified with more stringent criteria  
 1714 in isolation and momentum as described in Reference [99]. The PF elements  
 1715 associated with an identified muon are masked from the PF block.

1716 • Electrons are identified and reconstructed as described above plus some addi-  
 1717 tional requirements on fourteen variables like the amount of energy radiated,  
 1718 the distance between the extrapolated track position at the ECAL and the po-  
 1719 sition of the associated ECAL supercluster, among others, which are combined  
 1720 in an specialized multivariate analysis strategy that improves the electron iden-  
 1721 tification. Tracks and clusters used to identify and reconstruct electrons are  
 1722 masked in the PF block.

- 1723     ● Isolated photons are identified from ECAL superclusters with  $E_T$  larger than 10  
 1724       GeV, for which the energy deposited at a distance of 0.15, from the supercluster  
 1725       position on the  $(\eta,\phi)$  plane, does not exceed 10% of the supercluster energy;  
 1726       note that this is an isolation requirement. In addition, there must not be links  
 1727       to tracks. Clusters involved in the identification and reconstruction are masked  
 1728       in the PF block.
  
- 1729     ● Bremsstrahlung photons and prompt photons tend to convert to electron-positron  
 1730       pairs inside the tracker, therefore, a dedicated finder algorithm is used to link  
 1731       tracks that seem to originate from a photon conversion; in case those two tracks  
 1732       are compatible with the direction of a bremsstrahlung photon, they are also  
 1733       linked to the original electron track. Photon conversion tracks are also masked  
 1734       in the PF block.
  
- 1735     ● The remaining elements in the PF block are used to identify hadrons. In the  
 1736       region  $|\eta| \leq 2.5$ , neutral hadrons are identified with HCAL clusters not linked  
 1737       to any track while photons from neutral pion decays are identified with ECAL  
 1738       clusters without links to tracks. In the region  $|\eta| > 2.5$  ECAL clusters linked to  
 1739       HCAL clusters are identified with a charged or neutral hadron shower; ECAL  
 1740       clusters with no links are identified with photons. HCAL clusters not used yet,  
 1741       are linked to one or more unlinked tracks and to an unlinked ECAL in order to  
 1742       reconstruct charged-hadrons or a combination of photons and neutral hadrons  
 1743       according to certain conditions on the calibrated calorimetric energy.
  
- 1744     ● Charged-particle tracks may be liked together when they converge to a *sec-  
 1745       ondary vertex (SV)* displaced from the interaction point where the PV and PU  
 1746       vertices are reconstructed; at least three tracks are needed in that case, of which  
 1747       at most one has to be an incoming track with hits in tracker region between a

1748 PV and the SV.

1749

1750 The linker algorithm, as well as the whole PF algorithm, has been validated and  
 1751 commissioned; results from that validation are presented in the Reference [92].

1752 **Jet reconstruction.**

1753 Quarks and gluons may be produced in the  $pp$  collisions, therefore, their hadronization  
 1754 will be seen in the detector as a shower of hadrons and their decay products in the  
 1755 form of a *jet*. The anti- $k_t$  algorithm [100] is used to perform the jet reconstruction  
 1756 by clustering those PF particles within a cone (see Figure 4.3); previously, isolated  
 1757 electrons, isolated muons, and charged particles associated with other interaction  
 1758 vertices are excluded from the clustering.

1759 The anti- $k_t$  algorithm proceeds in a sequential recombination of PF particles; the  
 1760 distance between particles  $i$  and  $j$  ( $d_{ij}$ ) and the distance between particles and the  
 1761 beam are defined as

$$d_{ij} = \min\left(\frac{1}{k_{ti}^2}, \frac{1}{k_{tj}^2}\right) \frac{\Delta_{ij}^2}{R^2}$$

$$d_{iB} = \frac{1}{k_{ti}^2} \quad (4.1)$$

1762 where  $\Delta_{ij}^2 = (y_i - y_j)^2 + (\phi_i - \phi_j)^2$ ,  $k_{ti}, y_i$  and  $\phi_i$  are the transverse momentum, ra-  
 1763 pidity and azimuth of particle  $i$  respectively and  $R$  is the called jet radius. For all  
 1764 the remaining PF particles, after removing the isolated ones,  $d_{ij}$  and  $d_{iB}$  are calcu-  
 1765 lated<sup>5</sup> and the smallest is identified; if it is a  $d_{ij}$ , particles  $i$  and  $j$  are replaced with

---

<sup>5</sup> Notice that this is a combinatorial calculation.

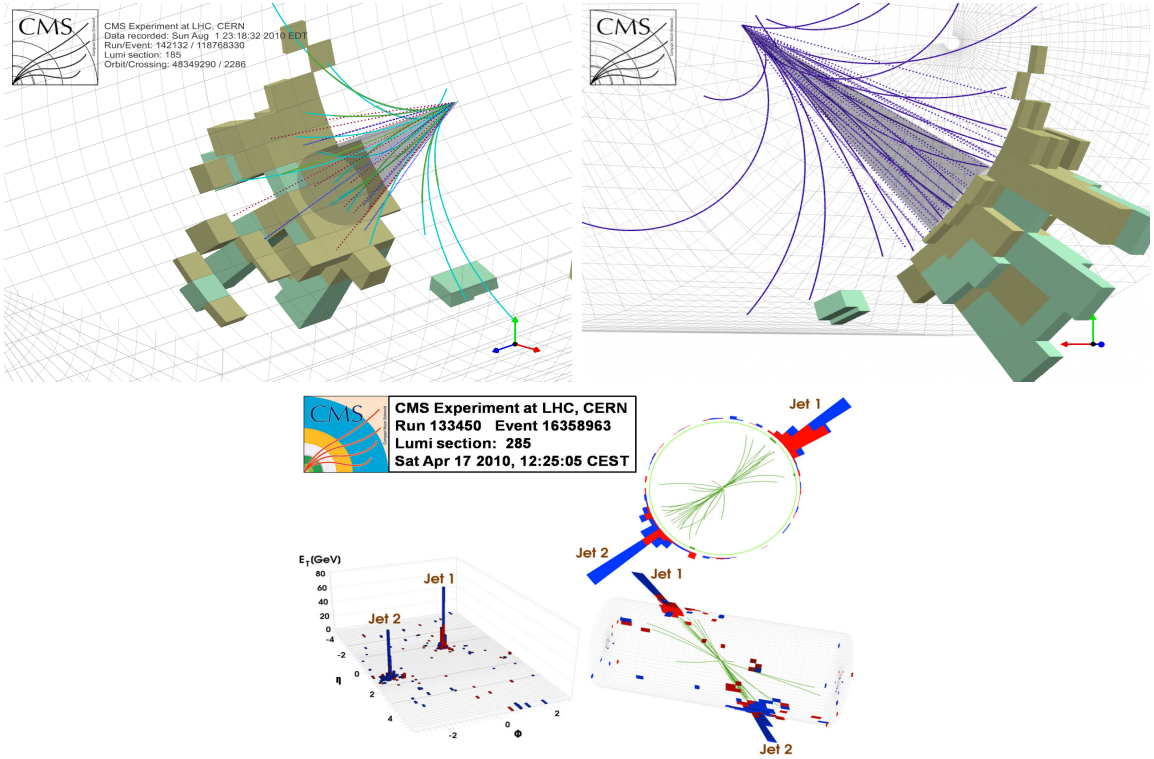


**Figure 4.3:** Jet reconstruction performed by the anti- $k_t$  algorithm. Top: Two different views of a CMS recorded event are presented. Continuous lines correspond to tracks left by charged particles in the tracker while dotted lines are the imaginary paths followed by neutral particles. The green cubes represent the ECAL cells while the blue ones represent the HCAL cells; in both cases, the height of the cube represent the amount of energy deposited in the cells [101]. Bottom: Reconstruction of a recorded event with two jets [102].

1766 a new object whose momentum is the vectorial sum of the combined particles. If the  
 1767 smallest distance is a  $d_{iB}$  the clustering process ends, the object  $i$  (which at this stage  
 1768 should be a combination of several PF particles) is declared as a *Particle-flow-jet* (PF  
 1769 jet) and all the associated PF particles are removed from the detector. The clustering  
 1770 process is repeated until no PF particles remain.

1771 Even though jets can be reconstructed efficiently, there are some effects that are not in-  
 1772 cluded in the reconstruction and that lead to discrepancies between the reconstructed  
 1773 results and the predicted results; in order to overcome these discrepancies, a factor-  
 1774 ized model has been designed in the form of jet energy corrections (JEC) [103, 104]

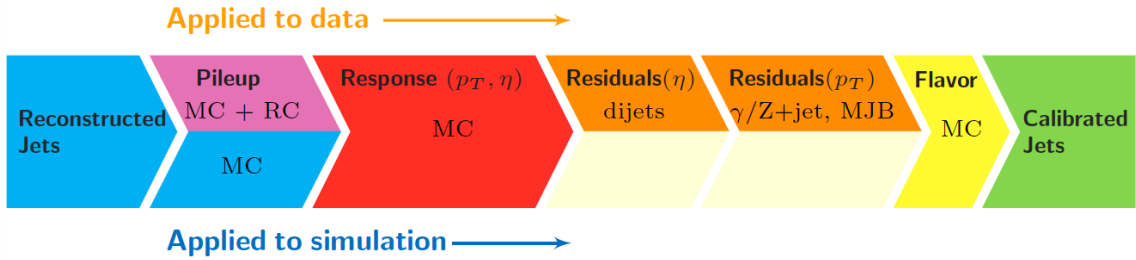


**Figure 4.4:** Jet energy correction diagram. Correction levels are applied sequentially in the indicated fixed order [104].

1775 applied sequentially as shown in the diagram of Figure 4.4.

1776 At each level, the jet four-momentum is multiplied by a scaling factor based on jet  
1777 properties, i.e.,  $\eta$ , flavor, etc.

1778 • Level 1 correction removes the energy coming from pile-up. The scale factor is  
1779 determined using a MC sample of QCD dijet (2 jets) events with and without  
1780 pileup overlay; it is parametrized in terms of the offset energy density  $\rho$ , jet  
1781 area  $A$ , jet  $\eta$  and jet  $p_T$ . Different corrections are applied to data and MC due  
1782 to the detector simulation.

1783 • MC-truth correction accounts for differences between the reconstructed jet en-  
1784 ergy and the MC particle-level energy. The correction is determined on a QCD  
1785 dijet MC sample and is parametrized in terms of the jet  $p_T$  and  $\eta$ .

1786 • Residuals correct remaining small differences within jet response in data and  
1787 MC. The Residuals  $\eta$ -dependent correction compares jets of similar  $p_T$  in the  
1788 barrel reference region. The Residuals  $p_T$ -dependent correct the jet absolute  
1789 scale (JES vs  $p_T$ ).

1790 • Jet-flavor corrections are derived in the same way as MC-truth corrections but  
1791 using QCD pure flavor samples.

1792 ***b*-tagging of jets.**

1793 A particular feature of the hadrons containing bottom quarks (*b*-hadrons) is that  
 1794 their lifetime is long enough to travel some distance before decaying, but it is not as  
 1795 long as those of light quark hadrons; therefore, when looking at the hadrons produced  
 1796 in  $pp$  collisions, *b*-hadrons decay typically inside the tracker rather than reaching the  
 1797 calorimeters as some light-hadrons do. As a result, a *b*-hadron decay gives rise to a  
 1798 displaced vertex (secondary vertex) with respect to the primary vertex as shown in  
 1799 Figure 4.5; the SV displacement is in the order of a few millimeters. A jet resulting  
 1800 from the decay of a *b*-hadron is called *b* jet; other jets are called light jets.

1801

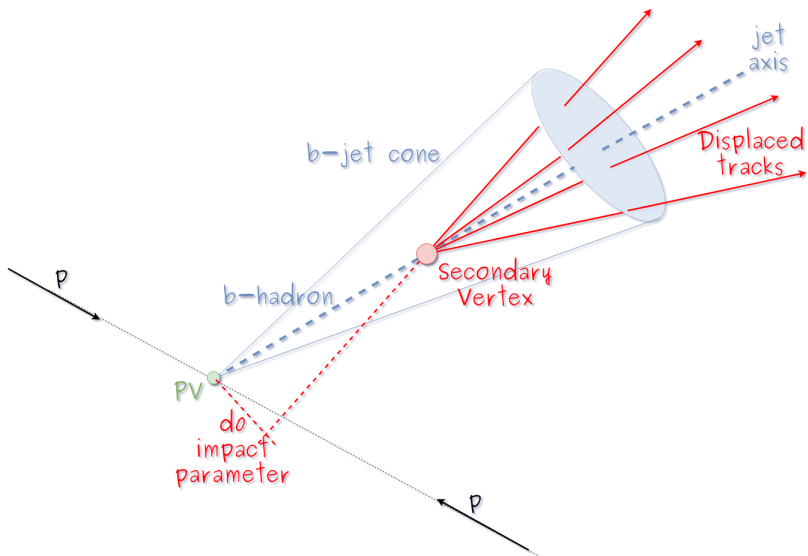


**Figure 4.5:** Secondary vertex in a *b*-hadron decay.

1802 Several methods to identify *b*-jets (*b*-tagging) have been developed; the method used  
 1803 in this thesis is known as *Combined Secondary Vertex* algorithm in its second version  
 1804 (CSVv2) [105]. By using information of the impact parameter, the reconstructed  
 1805 secondary vertices, and the jet kinematics as input in a multivariate analysis that  
 1806 combines the discrimination power of each variable in one global discriminator vari-

able, three working points (references): loose, medium and tight, are defined which quantify the probabilities of mistag jets from light quarks as jets from  $b$  quarks; 10, 1 and 0.1 % respectively. Although the mistagging probability decreases with the working point strength, the efficiency to correctly tag  $b$ -jets also decreases as 83, 69 and 49 % for the respective working point; therefore, a balance needs to be achieved according to the specific requirements of the analysis.

#### 4.4.1.1 Missing transverse energy.

The fact that proton bunches carry momentum along the  $z$ -axis implies that for each event it is expected that the momentum in the transverse plane is balanced. Imbalances are quantified by the missing transverse energy (MET) and are attributed to several sources including particles escaping undetected through the beam pipe, neutrinos produced in weak interactions processes which do not interact with the detector and thus escaping without leaving a sign, or even undiscovered particles predicted by models beyond the SM.

1821

1822 The PF algorithm assigns the negative sum of the momenta of all reconstructed PF  
1823 particles to the *particle-flow MET* according to

$$\vec{E}_T = - \sum_i \vec{p}_{T,i} \quad (4.2)$$

1824 JEC are propagated to the calculation of the  $\vec{E}_T$  as described in the Reference [106].

1825

1826 **4.4.2 Event reconstruction examples**

1827 Figures 4.6-4.8 show the results of the reconstruction performed on 3 recorded events.

1828 Descriptions are taken directly from the source.

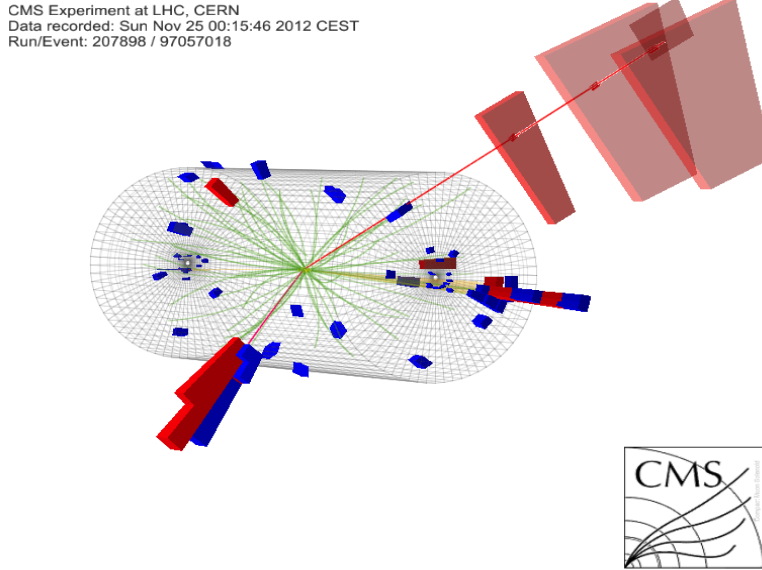


**Figure 4.6:** HIG-13-004 Event 1 reconstruction results; “HIG-13-004 Event 1: Event recorded with the CMS detector in 2012 at a proton-proton center-of-mass energy of 8 TeV. The event shows characteristics expected from the decay of the SM Higgs boson to a pair of  $\tau$  leptons. Such an event is characterized by the production of two forward-going jets, seen here in opposite endcaps. One of the  $\tau$  decays to a muon (red lines on the right) and neutrinos, while the other  $\tau$  decays into a charged hadron and a neutrino.” [107].

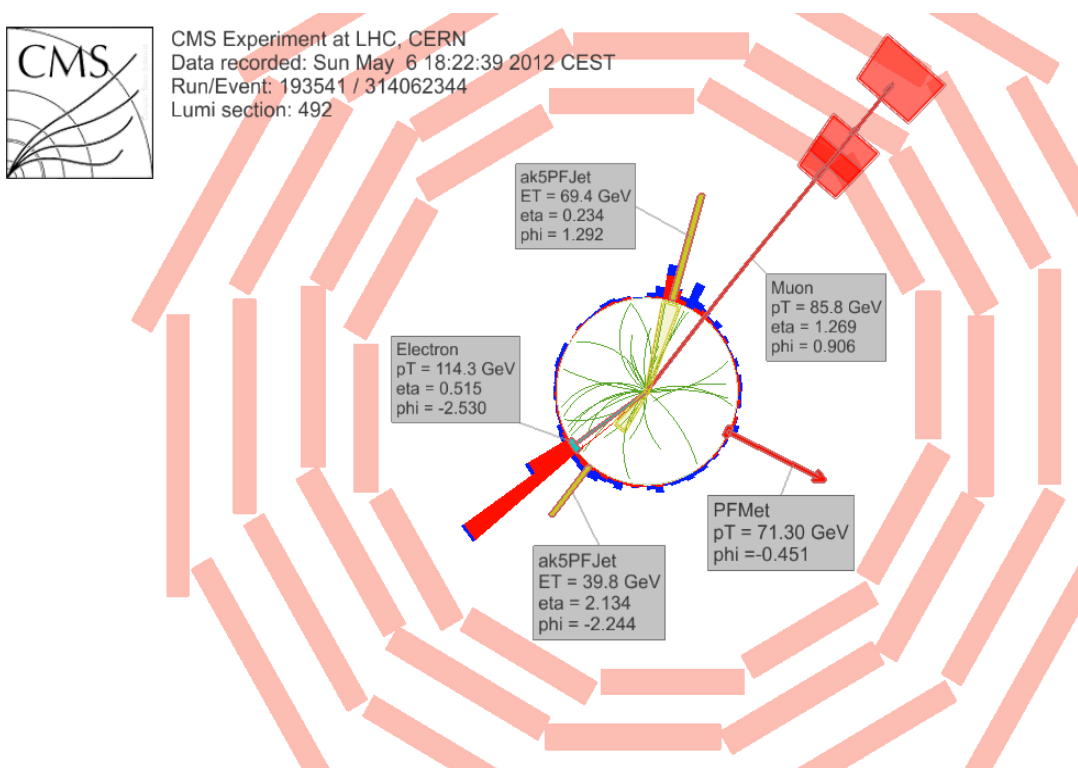


**Figure 4.7:**  $e\mu$  event reconstruction results; “An  $e\mu$  event candidate selected in 8 TeV data, as seen from the direction of the proton beams. The kinematics of the main objects used in the event selection are highlighted: two isolated leptons and two particle-flow jets. The reconstructed missing transverse energy is also displayed for reference” [108].

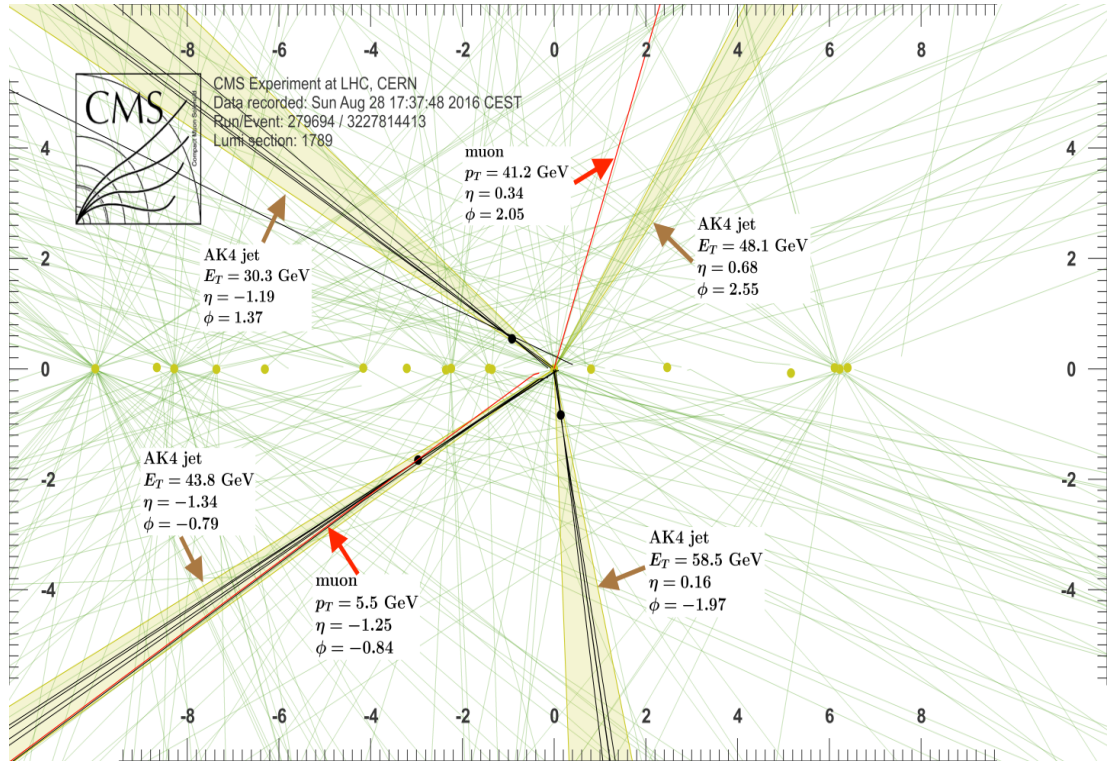


**Figure 4.8:** Recorded event reconstruction results; “Recorded event ( $\rho$ - $z$  projection) with three jets with  $p_T > 30$  GeV with one displaced muon track in 2016 data collected at 13 TeV. Each of the three jets has a displaced reconstructed vertex. The jet with  $p_T(j) = 43.8$  GeV,  $\eta(j) = -1.34$ ,  $\phi(j) = -0.79$  contains muon with  $p_T(\mu) = 5.5$  GeV,  $\eta(\mu) = -1.25$ ,  $\phi(\mu) = -0.84$ . Event contains reconstructed isolated muon with  $p_T(\mu) = 41.2$  GeV,  $\eta(\mu) = 0.34$ ,  $\phi(\mu) = 2.05$  and MET with  $p_T = 72.5$  GeV,  $\phi = -0.32$ . Jet candidates for a  $b$ -jet from top quark leptonic and hadronic decays are tagged by CSVv2T algorithm. One of the other two jets is tagged by CharmT algorithm. Tracks with  $p_T > 0.5$  GeV are shown. The number of reconstructed primary vertices is 18. Reconstructed  $m_T(W)$  is 101.8 GeV. Beam spot position correction is applied. Reconstructed primary vertices are shown in yellow color, while reconstructed displaced vertices and associated tracks are presented in black color. Dimensions are given in cm” [109].

1829 **Chapter 5**

1830 **Statistical methods**

1831 In the course of analyzing the data sets provided by the CMS experiment and used in  
1832 this thesis, several statistical tools have been employed; in this chapter, a description  
1833 of these tools will be presented, starting with the general statement of the multivariate  
1834 analysis method, followed by the particularities of the Boosted Decision Trees (BDT)  
1835 method and its application to the classification problem. Statistical inference methods  
1836 used will also be presented. This chapter is based mainly on the references [110–112].

1837 **5.1 Multivariate analysis**

1838 Multivariate data analysis (MVA) makes reference to statistical techniques that an-  
1839 alyze data containing information of more than one variable, commonly taking into  
1840 account the effects of all variables on the response of the particular variable under  
1841 investigation, i.e., considering all the correlations between variables. MVA is em-  
1842 ployed in a variety of fields like consumer and market research, quality control and  
1843 process optimization. From a MVA it is possible to identify the dominant patterns  
1844 in the data, like groups, outliers and trends, and determine to which group a set of

1845 values belong; in the particle physics context, MVA methods are used to perform the  
 1846 selection of certain type of events, from a large data set, using a potentially large  
 1847 number of measurable properties for each event.

1848 Processes with small cross section, as the  $tHq$  process, normally are hidden behind  
 1849 more common processes; therefore, the data set results in a subset of events with  
 1850 characteristic features of interest (signal) mixed in randomly with a much larger  
 1851 number of SM events that can mimic these features of interest (background) which  
 1852 implies that it is not possible to say with certainty that a given event is signal or  
 1853 background. In that sense, the problem can be formulated as one where a set of  
 1854 events have to be classified according to some features; these features correspond to  
 1855 the measurements of several parameters like energy or momentum, organized in a  
 1856 set of *input variables*. The measurements for each event can be written in a vector  
 1857  $\mathbf{x} = (x_1, \dots, x_n)$  for which

- 1858     • Signal hypotheses  $\rightarrow f(\mathbf{x}|s)$  is the probability density (*likelihood function*) that  
   1859        $\mathbf{x}$  is the set of measured values given that the events is a signal event.
- 1860     • Background hypotheses  $\rightarrow f(\mathbf{x}|b)$  is the probability density (*likelihood function*)  
   1861       that  $\mathbf{x}$  is the set of measured values given that the event is a background event.

1862     Figure 5.1 shows three ways to perform a classification of events for which mea-  
 1863       surements of two properties, two input variables, have been performed; blue circles  
 1864       represent signal events while red triangles represent background events. The classi-  
 1865       fication on (a) is *cut-based* requiring  $x_1 < c_1$  and  $x_2 < c_2$ ; usually the cut values are  
 1866       chosen according to some knowledge about the event process. In (b), the classification  
 1867       is performed by stating a cut involving a linear function of the input variables and  
 1868       so the boundary, while in (c) the the relationship between the input variables is not  
 1869       linear thus the boundary is not linear either.

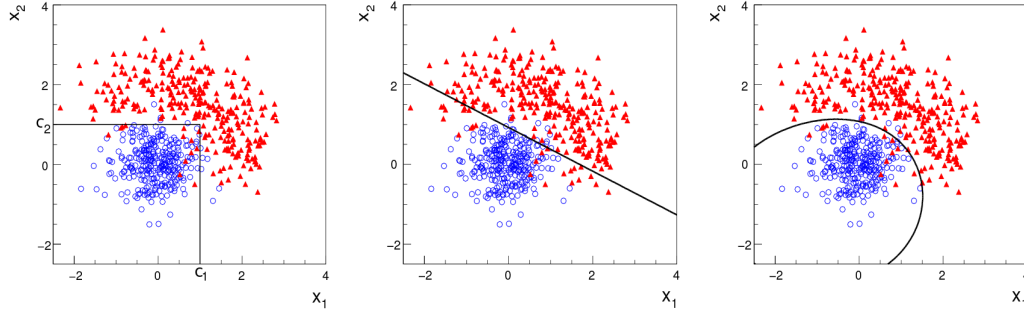


**Figure 5.1:** Scatter plots-MVA event classification. Distribution of two input variables  $x_1$  and  $x_2$  measured for a set of events; blue circles represent signal events and red triangles represent background events. The classification is based on (a) cuts, (b) linear boundary, and (c) nonlinear boundary [110]

1870        The boundary can be parametrized in terms of the input variables such that the  
 1871        cut is set on the parametrization instead of on the variables, i.e.,  $y(\mathbf{x}) = y_{cut}$  with  
 1872         $y_{cut}$  a constant; thus, the acceptance or rejection of an event is based on what side  
 1873        of the boundary is the event located. If  $y(\mathbf{x})$  has functional form, it can be used to  
 1874        determine the probability distribution functions  $p(y|s)$  and  $p(y|b)$  and then perform  
 1875        a scalar test statistic with a single cut on the scalar variable  $y$ .

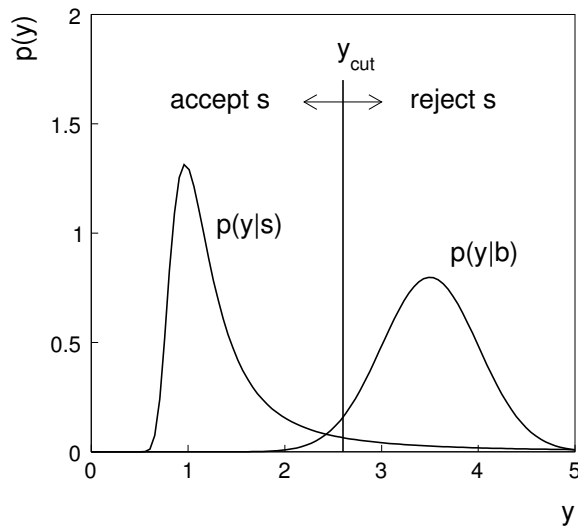


**Figure 5.2:** Distributions of the scalar test statistic  $y(\mathbf{x})$  under the signal and background hypotheses. [110]

1876       Figure 5.2 illustrates what would be the probability distribution functions under  
 1877   the signal and background hypotheses for a scalar test statistic with a cut on the  
 1878   classifier  $y$ . Notice that the tails of the distributions indicate that some signal events  
 1879   fall on the rejection region and some background events fall on the acceptance region;  
 1880   therefore, it is convenient to define the *efficiency* with which events of a given type  
 1881   are accepted, thus, the signal and background efficiencies are given by

$$\varepsilon_s = P(\text{accept event}|s) = \int_A f(\mathbf{x}|s) d\mathbf{x} = \int_{-\infty}^{y_{\text{cut}}} p(y|s) dy , \quad (5.1)$$

$$\varepsilon_b = P(\text{accept event}|b) = \int_A f(\mathbf{x}|b) d\mathbf{x} = \int_{-\infty}^{y_{\text{cut}}} p(y|b) dy , \quad (5.2)$$

1882   where  $A$  is the acceptance region. Under these conditions, the background hypothesis  
 1883   corresponds to the *null hypothesis* ( $H_0$ ), the signal hypothesis corresponds to the  
 1884   *alternative hypothesis* ( $H_1$ ), the background efficiency is the significance level of the  
 1885   test, and signal efficiency is the power of the test; what is sought in an analysis is to  
 1886   maximize the power of the test relative to the significance level.

### 1887 5.1.1 Decision trees

1888   For this thesis, the implementation of the MVA strategy, described above, is per-  
 1889   formed through decision trees by using the TMVA software package [111] included in  
 1890   the the ROOT analysis framework [113]. In a simple picture, a decision tree classifies  
 1891   events according to their input variables values by setting a cut on each input variable  
 1892   and checking which events are on which side of the cut, just as proposed in the MVA  
 1893   strategy, but in addition, as a machine learning algorithm, decision trees offer the  
 1894   possibility to be trained and then perform the classification efficiently.

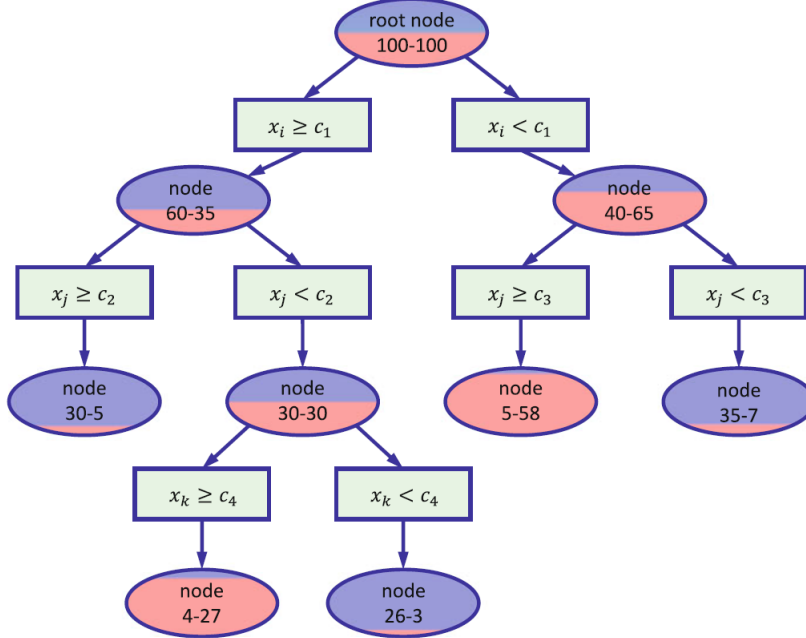


**Figure 5.3:** Example of a decision tree. Each node is fed with a MC sample mixing signal and background events (left-right numbers); nodes colors represent the relative amount of signal/background events [112].

1895        The training or growing of a decision tree is the process that defines the rules for  
 1896        classifying events; this process is represented in figure 5.3 and consist of several steps

1897        • take MC samples of signal and background events and split them into two parts  
 1898        each; first parts form the training sample which will be used in the decision tree  
 1899        training, while the second parts form the test sample which will be used for  
 1900        testing the final classifier obtained from the training. Each event has associated  
 1901        a set of input variables  $\mathbf{x} = (x_1, \dots, x_n)$  which serve to distinguish between signal  
 1902        and background events. The training sample is taken in at the root *node*.

1903        • pick one variable, say  $x_i$   
 1904        • pick one value of  $x_i$ , each event has its own value of  $x_i$ , and split the training  
 1905        sample into two subsamples  $B_1$  and  $B_2$ ;  $B_1$  contains events for which  $x_i < c_1$

- 1906        while  $B_2$  contains the rest of the training events;
- 1907        • scan all possible values of  $x_i$  and find the splitting value that provides the *best*  
 1908        classification<sup>1</sup>, i.e.,  $B_1$  is mostly made of signal events while  $B_2$  is mostly made  
 1909        of background events.
- 1910        • It is possible that variables other than the picked one produce a better classi-  
 1911        fication, hence, all the variables have to be evaluated. Pick the next variable,  
 1912        say  $x_j$ , and repeat the scan over its possible values.
- 1913        • At the end, all the variables and their values will have been scanned, the *best*  
 1914        variable and splitting value will have been identified, say  $x_1, c_1$ , and there will  
 1915        be two nodes fed with the subsamples  $B_1$  and  $B_2$ .
- 1916        Nodes are further split by repeating the decision process until: a given number of  
 1917        final nodes is obtained, nodes are largely dominated by either signal or background  
 1918        events, or nodes has too few events to continue. Final nodes are called *leaves* and they  
 1919        are classified as signal or background leaves according to the class of the majority of  
 1920        events in them. Each *branch* in the tree corresponds to a sequence of cuts.
- 1921        The quality of the classification at each node is evaluated through a separation  
 1922        criteria; there are several of them but the *Gini Index* ( $G$ ) is the one used in the  
 1923        decision trees trained for the analysis in this thesis.  $G$  is written in terms of the  
 1924        purity ( $P$ ), i.e. the fraction of signal events, of the samples after the separation is  
 1925        made; it is given by

$$G = P(1 - P) \quad (5.3)$$

---

<sup>1</sup> Quality of the classification will be treated in the next paragraph.

1926 notice that  $P=0.5$  at the root node while  $G=0$  for pure leaves. For a node  $A$  split  
 1927 into two nodes  $B_1$  and  $B_2$  the G gain is

$$\Delta G = G(A) - G(B_1) - G(B_2) \quad (5.4)$$

1928 the *best* classification corresponds to that for which the gain of G is maximized; hence,  
 1929 the scanning over all event's variables and their values is of capital importance.

1930 In order to provide a numerical output for the classification, events in a sig-  
 1931 nal(background) leaf are assigned an score of 1(-1) each, defining in this way the  
 1932 decision tree *classifier or weak learner* as

$$f(\mathbf{x}) = \begin{cases} 1 & \mathbf{x} \text{ in signal region,} \\ -1 & \mathbf{x} \text{ in background region.} \end{cases}$$

1933 Figure 5.4 shows an example of the classification of a sample of events, containing  
 1934 two variables, performed by a decision tree.

### 1935 5.1.2 Boosted decision trees (BDT).

1936 Event misclassification occurs when a training event ends up in the wrong leaf, i.e., a  
 1937 signal event ends up in a background leaf or a background event ends up in a signal  
 1938 leaf. A way to correct it is to assign a weight to the misclassified events and train  
 1939 a second tree using the reweighted events; the event reweighting is performed by a  
 1940 boosting algorithm, events with increased weight are known as *boosted* events, in such  
 1941 a way that when used in the training of a new decision tree they get correctly classified.  
 1942 The process is repeated iteratively adding a new tree to a forest and creating a set  
 1943 of classifiers which are combined to create the next classifier; the final classifier offers

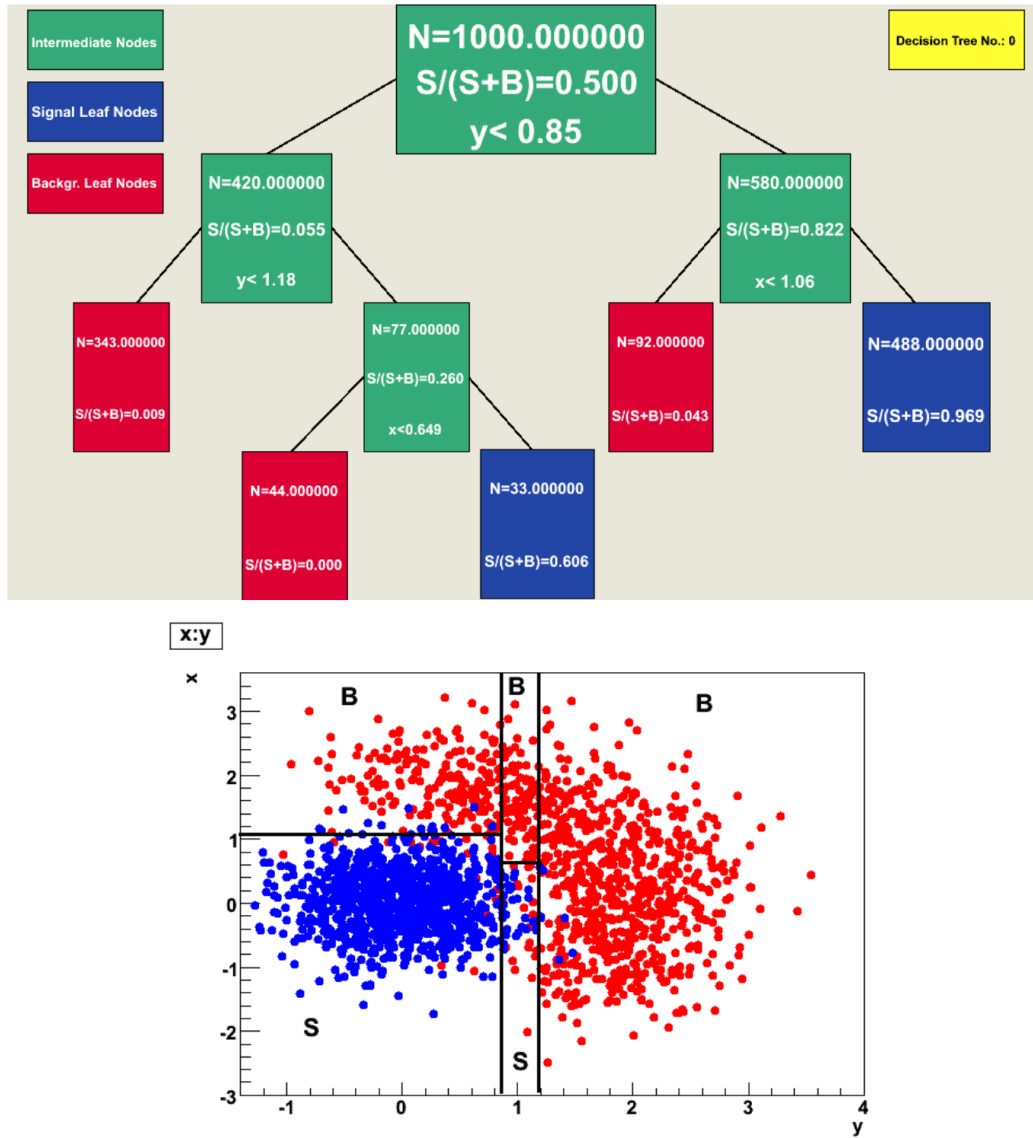


**Figure 5.4:** Example of a decision tree output. Each leaf, blue for signal events and red for background events, represent a region in the variables phase space [114].

1944 more stability<sup>2</sup> and has a smaller misclassification rate than any individual ones. The  
 1945 resulting tree collection is known as a *boosted decision tree (BDT)*.  
 1946 Thus, purity of the sample is generalized to

<sup>2</sup> Decision trees suffer from sensitivity to statistical fluctuations in the training sample which may leads to very different results with an small change in the training samples.

$$P = \frac{\sum_s w_s}{\sum_s w_s + \sum_b w_b} \quad (5.5)$$

1947 where  $w_s$  and  $w_b$  are the weights of the events; the Gini index is also generalized

$$G = \left( \sum_i^n w_i \right) P(1 - P) \quad (5.6)$$

1948 with  $n$  the number of events in the node. The final score of an event, after pass-  
 1949 ing through the forest, is calculated as the renormalized sum of all the individual  
 1950 (possibly weighted) scores; thus, high(low) score implies that the event is most likely  
 1951 signal(background).

1952 The boosting procedure, implemented in the *Gradient boosting* algorithm used  
 1953 in this thesis, produce a classifier  $F(\mathbf{x})$  which is the weighted sum of the individual  
 1954 classifiers obtained after each iteration,i.e.,

$$F(\mathbf{x}) = \sum_{m=1}^M \beta_m f(\mathbf{x}; a_m) \quad (5.7)$$

1955 where M is the number of trees in the forest. The *loss function*  $L(F, y)$  represent the  
 1956 deviation between the classifier  $F(\mathbf{x})$  response and the true value  $y$  obtained from the  
 1957 training sample (1 for signal events and -1 for background event), according to

$$L(F, y) = \ln(1 + e^{-2F(\mathbf{x})y}) \quad (5.8)$$

1958 thus, the reweighting is employed to ensure the minimization of the loss function;  
 1959 a more detailed description of the minimization procedure can be found in reference  
 1960 [115]. The final classifier output is later used as a final discrimination variable, labeled  
 1961 as *BDT output/response*.

1962 **5.1.3 Overtraining.**

1963 Decision trees offer the possibility to have as many nodes as wished in order to  
 1964 reduce the misclassification to zero (in theory); however, when a classifier is too much  
 1965 adjusted to a particular training sample, the classifier response to a slightly different  
 1966 sample may leads to a completely different classification results; this effect is known  
 1967 as *overtraining*.

1968 An alternative to reduce the overtraining in BDTs consist in pruning the tree by  
 1969 removing statistically insignificant nodes after the tree growing is completed but this  
 1970 option is not available for BDTs with gradient boosting in the TMVA-toolkit, there-  
 1971 fore, the overtraining has to be reduced by tuning the algorithm, number of nodes,  
 1972 minimum number of events in the leaves, etc. The overtraining can be evaluated  
 1973 by comparing the responses of the classifier when running over the training and test  
 1974 samples.

1975 **5.1.4 Variable ranking.**

1976 BDTs have the couple of particular advantages related to the input variables; on one  
 1977 side, they are relatively insensitive to the number of input variables used in the vector  
 1978  $\mathbf{x}$ . The ranking of the BDT input variables is determined by counting the number of  
 1979 times a variable is used to split decision tree nodes; in addition, the separation gain-  
 1980 squared achieved in the splitting and the number of events in the node are accounted  
 1981 by applying a weighting to that number. Thus, those variables with small or no power  
 1982 to separate signal and background events are rarely chosen to split the nodes,i.e., are  
 1983 effectively ignored.

1984 On the other side, variables correlations play an important role for some MVA  
 1985 methods like the Fisher discriminant algorithm in which the first step consist of

1986 performing a linear transformation to a phase space where the correlations between  
 1987 variables are removed; in case of BDT algorithm, correlations do not affect the per-  
 1988 formance.

1989 **5.1.5 BDT output example.**

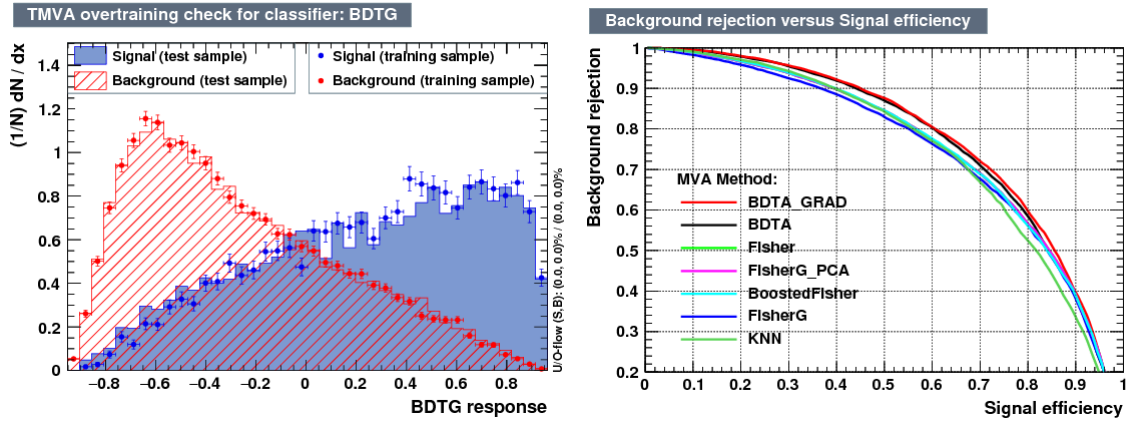


**Figure 5.5:** Left: Output distributions for the gradient boosted decision tree (BDTG) classifier using a sample of signal( $pp \rightarrow tHq$ ) and background( $pp \rightarrow t\bar{t}$ ) events. Right: Background rejection vs signal efficiency (ROC curves) for various MVA classifiers running over the same sample used to produce the plot on the left.

1990 Left side of figure 5.5 shows the BDT output distributions for signal( $pp \rightarrow tHq$ )  
 1991 and background( $pp \rightarrow t\bar{t}$ ) events; this plot is the equivalent to the one showed in  
 1992 figure 5.2. A forest with 800 trees, maximum depth per tree = 3, and gradient  
 1993 boosting have been used as training parameters. The BDTG classifier offers a good  
 1994 separation power; while there is a small overtraining in the signal distribution, the  
 1995 background distribution seems to be well predicted which might indicate that the  
 1996 sample is composed of more background than signal events.

1997 Right side of figure 5.5 shows the background rejection vs signal efficiency curves  
 1998 for several combinations of MVA classifiers-boosting algorithms; these curves are  
 1999 known as ROC curves and give an indication of the performance of the classifier. The

2000 best performance is achieved with the BDTG classifier (BDTA\_GRAD).

## 2001 5.2 Statistical inference.

2002 Once events are classified, the next step consists in finding the parameters that define  
 2003 the likelihood functions  $f(\mathbf{x}|s), f(\mathbf{x}|b)$  for signal and background events respectively.  
 2004 In general, likelihood functions depend not only on the measurements but also on  
 2005 parameters ( $\theta_m$ ) that define their shapes; the process of estimating these *unknown*  
 2006 *parameters* and their uncertainties from the experimental data is called *inference*.  
 2007 The likelihood function for  $N$  the events the in a sample is the combination of all the  
 2008 likelihoods functions

$$L(\boldsymbol{\theta}) = \prod_{i=1}^N f(\mathbf{x}^i | \boldsymbol{\theta}) = \prod_{i=1}^N f(x_1^i, \dots, x_n^i; \theta_1, \dots, \theta_m) \quad (5.9)$$

2009 Thus, the estimation of the unknown parameters from experimental data samples  
 2010 is written in terms of a central value using the notation

$$\theta = \hat{\theta} \pm \delta\theta \quad (5.10)$$

2011 where the interval  $[\hat{\theta} + \delta\theta, \hat{\theta} - \delta\theta]$  is called *confidence interval*; it is usually inter-  
 2012 preted, in the limit of infinite number of experiments, as the interval where the true  
 2013 value of the unknown parameter  $\theta$  is contained with a probability of 0.6827 (if no  
 2014 other convention is stated).

### 2015 5.2.1 Nuisance parameters.

2016 The unknown parameter vector  $\boldsymbol{\theta}$  is made of two types of parameters: on one side,  
 2017 those parameters that provide information about the physical observables of interest

2018 for the experiment (*parameters of interest*); on the other side, the *nuisance parameters*  
 2019 that are not of direct interest for the experiment but that needs to be included in  
 2020 the analysis in order to achieve a satisfactory description of the data. They represent  
 2021 effects of the detector response like the finite resolutions of the detection systems,  
 2022 miscalibrations, and in general any source of uncertainty introduced in the analysis.

2023 In some cases the nuisance parameters are estimated using dedicated data samples,  
 2024 for instance data from test beams for calibration purposes, when MC samples are  
 2025 not suitable. The nuisance parameter uncertainties produce *systematic uncertainties*  
 2026 while the uncertainties associated to fluctuations in data and related to the estimation  
 2027 of the parameters of interest produce *statistical uncertainties*.

## 2028 5.2.2 Maximum likelihood estimation method

2029 The function that produce the estimate of a parameter is called *estimator*, there-  
 2030 fore, estimators are usually constructed using mathematical procedures encoded in  
 2031 algorithms. The estimation method used in this thesis is the *Maximum Likelihood*  
 2032 *Estimation* method (MLE); it is based on the combined likelihood function defined  
 2033 by eqn. 5.9 and the procedure seeks for the parameter set that corresponds to the  
 2034 maximum value of the combined likelihood function, i.e., the *maximum likelihood*  
 2035 *estimator* of the unknown parameter vector  $\boldsymbol{\theta}$  is the function that produce the vec-  
 2036 tor  $\hat{\boldsymbol{\theta}}$  for which the likelihood function  $L(\boldsymbol{\theta})$  evaluated at the measured sample  $\mathbf{x}$  is  
 2037 maximum.

2038 Usually, the logarithm of the likelihood function is used in the numerical algo-  
 2039 rithms implementations in order to avoid underflow the numerical precision of the  
 2040 computers due to the product of low likelihoods. In addition, it is usual minimize the  
 2041 negative logarithm of the likelihood function instead of maximizing the logarithm of

2042 it because in this way the procedure consist of differentiate a sum of therms and set  
 2043 the sum to zero; therefore

$$F(\boldsymbol{\theta}) = -\ln L(\boldsymbol{\theta}) = -\sum_{i=1}^N f(\mathbf{x}^i | \boldsymbol{\theta}). \quad (5.11)$$

2044 The minimization process is performed by the software MINUIT [116] imple-  
 2045 mented in the ROOT analysis framework. In case of large data samples the compu-  
 2046 tational resources needed to calculate the likelihood function are too big; therefore,  
 2047 the parameter estimation is performed using binned distributions of the variables of  
 2048 interest for which the *binned likelihood function* is given by

$$L(data|\mu, \theta) = \prod_{i=1} \frac{(\mu s_i(\theta) + b_i(\theta))^{n_i}}{n_i!} e^{-\mu s_i(\theta) - b_i(\theta)}, \quad (5.12)$$

2049 with  $s_i$  and  $b_i$  the expected number of signal and background yields for bin  $i$  respec-  
 2050 tively,  $n_i$  is the observed number of events in the bin  $i$  and  $\mu = \sigma/\sigma_{SM}$  is the signal  
 2051 strength. Notice that the number of entries per bin follows a Poisson distribution.  
 2052 The analysis presented in this thesis is based on the binned distribution of the ratio  
 2053 signal/background obtained from the BDT outputs.

### 2054 5.2.3 Hypothesis test

2055 The test statistic mentioned in section 5.1 involving  
 2056 ; it is achieved, according to the Neyman-Pearson lemma [117],  
 2057 by defining the acceptance region such that, for  $\mathbf{x}$  inside the region, the likelihood  
 2058 ratio, i.e., the ratio of probability distribution functions for signal and background,

2059 **5.3 exclusion limits**

2060 **5.4 asymptotic limits**

# <sup>2061</sup> Chapter 6

<sup>2062</sup> **Search for production of a Higgs**  
<sup>2063</sup> **boson and a single top quark in**  
<sup>2064</sup> **multilepton final states in pp**  
<sup>2065</sup> **collisions at  $\sqrt{s} = 13$  TeV**

## <sup>2066</sup> 6.1 Introduction

<sup>2067</sup> The Higgs boson discovery, supported on experimental observations and theoretical  
<sup>2068</sup> predictions made about the SM, gives the clue of the way in that elementary particles  
<sup>2069</sup> acquire mass through the Higgs mechanism; therefore, knowing the Higgs mass, the  
<sup>2070</sup> Higgs-boson and Higgs-fermion couplings can be tested. In order to test the Higgs-top  
<sup>2071</sup> coupling, several measurements have been performed, as stated in the chapter 2, but  
<sup>2072</sup> they are limited to measure the square of the coupling; however, the production of a  
<sup>2073</sup> Higgs boson in association with a single top quark ( $tH$ ) not only offers access to the  
<sup>2074</sup> sign of the coupling, but also, to the CP phase of the Higgs couplings.

2075 This chapter presents the search for the associated production of a Higgs boson  
 2076 and a single top quark events, focusing on leptonic signatures provided by the Higgs  
 2077 decay modes to  $WW$ ,  $ZZ$ , and  $\tau\tau$ ; the 13 TeV dataset produced in 2016, which  
 2078 corresponds to an integrated luminosity of  $35.9\text{fb}^{-1}$ , is used. Constraints on the sign  
 2079 of the Higgs-top coupling ( $y_t$ ) have been derived from the decay rate of Higgs boson  
 2080 to photon pairs [40] and from the cross section for associated production of Higgs and  
 2081 Z bosons via gluon fusion [118], with recent results disfavoring negative signs of the  
 2082 coupling [51, 53, 119]. It expands previous analyses performed at 8 TeV [120, 121] and  
 2083 searches for associated production of  $t\bar{t}$  pair and a Higgs boson in the multilepton final  
 2084 state channel [122]; it also complements searches in other decay channels targeting  
 2085  $H \rightarrow b\bar{b}$  [123].

2086 As shown in section 2.4, the SM cross section of the associated production of a  
 2087 Higgs boson and a single top quark ( $tHq$ ) process is driven by a destructive interfer-  
 2088 ence between two contributions (see Figure 2.13), where the Higgs couples to either  
 2089 the W boson or the top quark; however, if the sign of the Higgs-top coupling is flipped  
 2090 with respect to the SM prediction, a large enhancement of the cross section occurs,  
 2091 making this analysis sensitive to such deviation. A second process, where the Higgs  
 2092 boson and top quark are accompanied by a W boson ( $tHW$ ) has similar behavior,  
 2093 albeit with a weaker interference pattern and lower contribution to the  $tH$  cross sec-  
 2094 tion, therefore, a combination of both processes would increase the sensitivity; in  
 2095 this analysis both contributions are combined and referred as  $tH$ channel. A third  
 2096 contribution comes from  $t\bar{t}H$  process. The purpose of this analysis is to investigate  
 2097 the exclusion of the presence of the  $tH + t\bar{t}H$  processes under the assumption of the  
 2098 anomalous Higgs-top coupling modifier ( $\kappa_t = -1$ ). The analysis exploits signatures  
 2099 with two leptons of the same sign (*2lss channel*) and three leptons (*3l channel*) in  
 2100 the final state.

2101        The first sections present the characteristic  $tHq$  signature as well as the expected  
 2102   backgrounds. The MC samples, data sets, and the physics object definitions are  
 2103   then defined. Following, the background predictions, the signal extraction, and the  
 2104   statistical treatment of the selected events as well as the systematic uncertainties are  
 2105   described. The final section present the results for the exclusion limits as a function  
 2106   of the ratio of  $\kappa_t$  and the dimensionless modifier of the Higgs-vector boson  $\kappa_V$ .

## 2107   **6.2 $tHq$ signature**

2108   In order to select events of  $tHq$  process, its features are translated into a set of  
 2109   selection rules; figure 6.1 shows the Feynman diagram and an schematic view of the  
 2110    $tHq$  process from the  $pp$  collision to the final state configuration. A single top quark  
 2111   is produced accompanied by a light quark, denoted as  $q$ ; this light quark is produced  
 2112   predominantly in the forward region of the detector. The Higgs boson which can  
 2113   be either emitted by the exchanged  $W$  boson or directly by the singly produced top  
 2114   quark.

2115        The top quark and Higgs boson decay after their production in the detector due to  
 2116   their high masses/low lifetimes. The Higgs boson is required to decay into a  $W$  boson  
 2117   pair<sup>1</sup>. The top quark almost always decays into a bottom quark and a  $W$  boson, as  
 2118   encoded in the CMK matrix. The  $W$  bosons are required to decay hadronically in  
 2119   the 2lss channel case and leptonically in the 3l channel case, while  $\tau$  leptons are not  
 2120   reconstructed separately and only their leptonic decays into either electrons or muons  
 2121   are considered in this analysis.

2122        In summary, the signal process is characterized by a the final state with

- 2123        • one light-flavored forward jet,

---

<sup>1</sup> ZZ and  $\tau\tau$  decays are also include in the analysis but they are not separately reconstructed

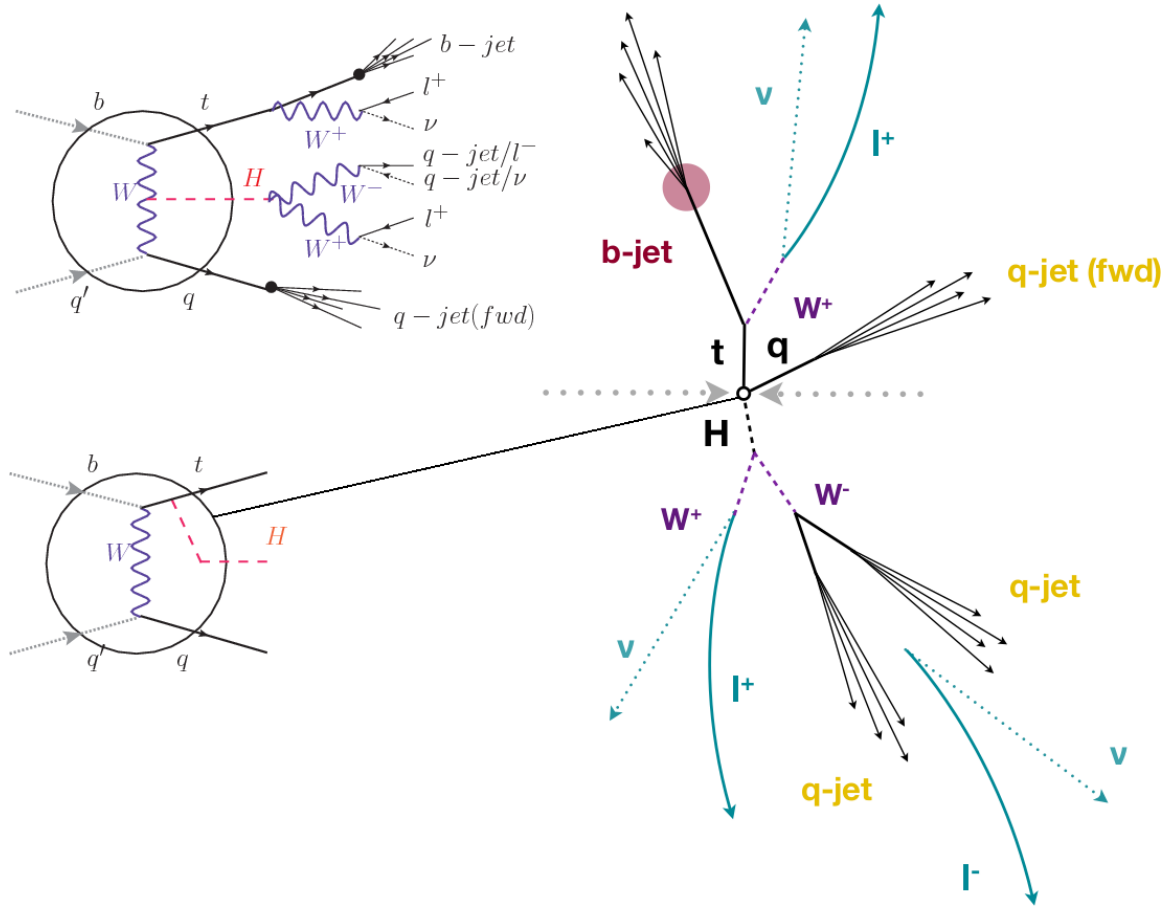


**Figure 6.1:**  $tHq$  event signature. Left: Feynman diagram including the whole evolution up to the final state for the case of the Higgs boson emitted by the  $W$  boson (top); Feynman diagram for the case where the Higgs boson is emitted by the top quark. Right: Schematic view as it would be seen in the detector; the circle in the Feynman diagrams on the left corresponds to the circle in the center of the schematic view as indicated by the line connecting them. In the 2lss channel, one of the  $W$  bosons from the Higgs boson decays to two light-quark jets while in the 3l channel both  $W$  bosons decays to leptons.

- 2124     • one central b-jet,
  - 2125     • 2lss channel  $\rightarrow$  two leptons of the same sign, two neutrinos and two light (often  
2126       soft) jets,
  - 2127     • 3l channel  $\rightarrow$  three leptons, three neutrinos and no central light-flavored jets,
- 2128     The presence of neutrinos is inferred from the presence of MET. The analysis has

been made public by CMS as a Physics Analysis Summary [124] combining the result for the three lepton and two lepton same-sign channels. Currently, an effort to turn the analysis into a paper is ongoing.

## 6.3 Background processes

The background processes are those that can mimic the signal signature or at least can be reconstructed as that as a result of certain circumstances. The backgrounds can be classified as

- Irreducible backgrounds where genuine prompt leptons are produced in on-shell W and Z boson decays; they can be reliably estimated directly from MC simulated events, using higher-order cross sections or data control regions for the overall normalization.

- Reducible backgrounds where at least one of the leptons is *non-prompt*, i.e., produced within a hadronic jet, either a genuine lepton from heavy flavor decays. misreconstructed jets, also known as *mis-ID leptons* or *fake leptons*, are considered non-prompt leptons as well. These non-prompt leptons leave tracks and hits in the detection systems as would a prompt lepton, but correlating those hits with nearby jets could be a way of removing them. Reducible backgrounds are not well predicted by simulation, and are estimated using data-driven methods.

The main sources of background events in the case of  $tHq$  process are  $t\bar{t}$  process and  $t\bar{t} + X(X = W, Z, \gamma)$  processes, here represented together as  $t\bar{t}V$  process. Figure 6.2 shows the signature for  $t\bar{t}$  and  $t\bar{t}W$  processes;

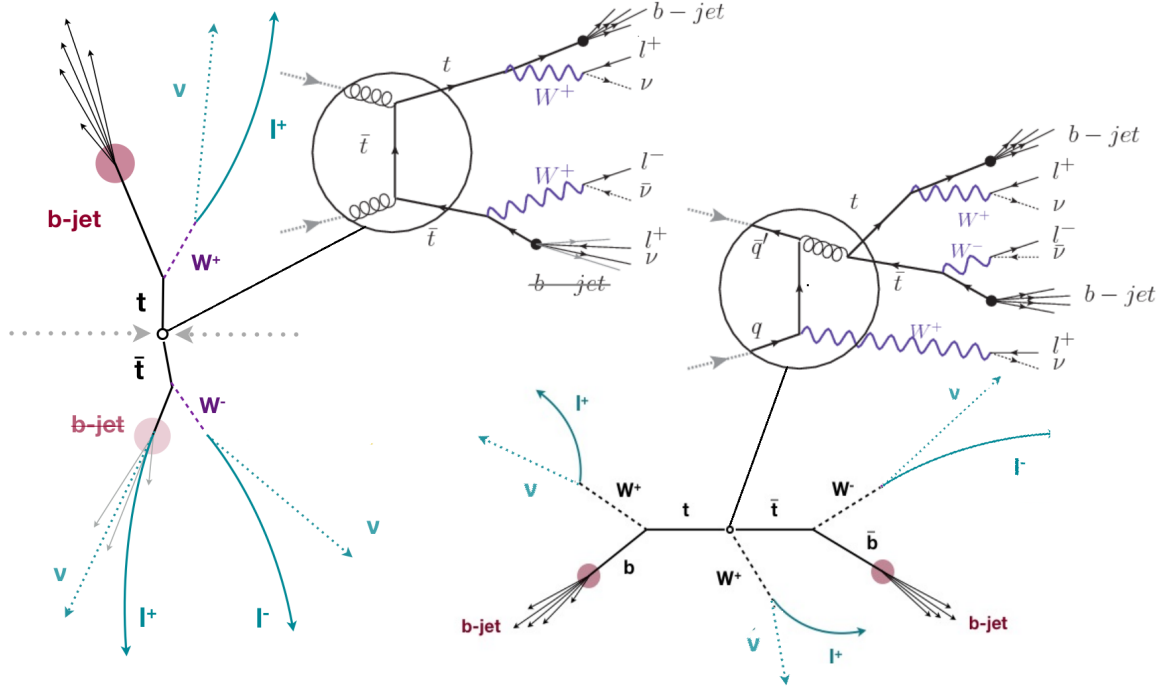


**Figure 6.2:**  $t\bar{t}$  (left) and  $t\bar{t}W$  (right) events signature as they would be seen in the detector; the Feynman diagrams including the whole evolution up to the final state are also showed. The  $t\bar{t}$  process signature is very similar to that of the signal process with one fake lepton and no forward activity. The  $t\bar{t}W$  process present a higher b-jet multiplicity compared to the signal process, a prompt lepton and no forward activity.

2151        The largest contribution to irreducible backgrounds involving prompt leptons  
 2152      comes from  $t\bar{t}W$ ,  $t\bar{t}Z$ , processes for which the number of ( $b-$ )jets (( $b-$ )jet multiplicity)  
 2153      is higher than that of the signal events, while for other contributing background  
 2154      events,  $WZ$ ,  $ZZ$ , and rare SM processes like  $W^\pm W^\pm qq$ ,  $t\bar{t}t\bar{t}$ ,  $tZq$ ,  $tZW$ ,  $WWW$ ,  
 2155       $WWZ$ ,  $WZZ$ ,  $ZZZ$ , the ( $b-$ )jet multiplicity is lower compared to that of the signal  
 2156      events. None of the irreducible backgrounds present activity in the forward region of  
 2157      the detector.

2158        On the side of the reducible backgrounds, the largest contribution comes from the  
 2159       $t\bar{t}$  events which have a very similar signature to the signal events but does no present  
 2160      activity in the forward region of the detector either; A particular feature of the  $t\bar{t}$   
 2161      events is their charge-symmetry which is also a difference with the signal events.

2162        The charge misidentification plays an important role in the the 2lss channel since  
 2163      leptons in processes like  $t\bar{t}$  + jets or  $Z$  + jets can be charge misidentified, leading to  
 2164      backgrounds increments. An identification variable have been designed in order to  
 2165      reject this type of background events.

## 2166     **6.4 Data and MC Samples**

2167    Technical developments on the event generator side allow for an event-wise reweight-  
 2168    ing that can change the event kinematics based on specific generation parameters.  
 2169    This way not only the case of  $C_t = \sqrt{2}$ , but a whole range of  $\kappa_t$  and  $\kappa_V$  values can  
 2170    be investigated.

2171        The data considered in this analysis were collected by the CMS experiment dur-  
 2172        ing 2016 and correspond to a total integrated luminosity of  $35.9 fb^{-1}$ . Only periods  
 2173        when the CMS magnet was on were considered when selecting the data samples, that  
 2174        corresponds to the 23 Sep 2016 (Run B to G) and PromptReco (Run H) versions  
 2175        of the datasets. The MC samples used in this analysis correspond to the RunI-  
 2176        ISummer16MiniAODv2 campaign produced with CMSSW 80X. The two signal sam-  
 2177        ples (for  $tHq$  and  $tHW$ ) were produced with MG5\_aMC@NLO (version 5.222), in  
 2178        leading-order order mode, and are normalized to next-to-leading-order cross sections,  
 2179        see Tab. 6.1. Each sample is generated with a set of event weights corresponding to  
 2180        different values of  $\kappa_t$  and  $\kappa_V$  couplings as shown in Tab. 6.2.

### 2181     **6.4.1 Full 2016 dataset and MC samples**

2182        Different MC generators were used to generate the background processes. The dom-  
 2183        inant sources ( $t\bar{t}$ ,  $t\bar{t}W$ ,  $t\bar{t}Z$ ,  $t\bar{t}H$ ) were produced using AMC@NLO interfaced to  
 2184        PYTHIA8, and are scaled to NLO cross sections. Other processes are simulated us-

Sample	$\sigma$ [pb]	BF
/THQ_Hincl_13TeV-madgraph-pythia8_TuneCUETP8M1/	0.7927	0.324
/THW_Hincl_13TeV-madgraph-pythia8_TuneCUETP8M1/	0.1472	1.0

**Table 6.1:** Signal samples and their cross section and branching fraction used in this analysis. See Ref. [133] for more details.

ing POWHEG interfaced to PYTHIA, or bare PYTHIA (see table 6.3 and [122] for more details).

## 6.4.2 Triggers

We consider online-reconstructed events triggered by one, two, or three leptons. Single-lepton triggers are included to boost the acceptance of events where the  $p_T$  of the sub-leading lepton falls below the threshold of the double-lepton triggers. Additionally, by including double-lepton triggers in the  $\geq 3$  lepton category, as well as single-lepton triggers in all categories, we increase the efficiency, considering the logical “or” of the trigger decisions of all the individual triggers in a given category. Tab. 6.5 shows the lowest-threshold non-prescaled triggers present in the High-Level Trigger (HLT) menus for both Monte-Carlo and data in 2016.

### Trigger efficiency scale factors

The efficiency of events to pass the trigger is measured in simulation (trivially using generator information) and in the data (using event collected by an uncorrelated MET trigger). Small differences between the data and MC efficiencies are corrected by applying scale factors as shown in Tab. 6.6. The exact procedure and control plots are documented in [127] for the current analysis.

		<i>tHq</i>		<i>tHW</i>		
$\kappa_V$	$\kappa_t$	sum of weights	cross section [pb]	sum of weights	cross section [pb]	LHE weights
1.0	-3.0	35.700022	2.991	11.030445	0.6409	LHEweight_wgt[446]
1.0	-2.0	20.124298	1.706	5.967205	0.3458	LHEweight_wgt[447]
1.0	-1.5	14.043198	1.205	4.029093	0.2353	LHEweight_wgt[448]
1.0	-1.25	11.429338	0.9869	3.208415	0.1876	LHEweight_wgt[449]
1.0	-1.0		0.7927		0.1472	
1.0	-0.75	7.054998	0.6212	1.863811	0.1102	LHEweight_wgt[450]
1.0	-0.5	5.294518	0.4723	1.339886	0.07979	LHEweight_wgt[451]
1.0	-0.25	3.818499	0.3505	0.914880	0.05518	LHEweight_wgt[452]
1.0	0.0	2.627360	0.2482	0.588902	0.03881	LHEweight_wgt[453]
1.0	0.25	1.719841	0.1694	0.361621	0.02226	LHEweight_wgt[454]
1.0	0.5	1.097202	0.1133	0.233368	0.01444	LHEweight_wgt[455]
1.0	0.75	0.759024	0.08059	0.204034	0.01222	LHEweight_wgt[456]
1.0	1.0	0.705305	0.07096	0.273617	0.01561	LHEweight_wgt[457]
1.0	1.25	0.936047	0.0839	0.442119	0.02481	LHEweight_wgt[458]
1.0	1.5	1.451249	0.1199	0.709538	0.03935	LHEweight_wgt[459]
1.0	2.0	3.335034	0.2602	1.541132	0.08605	LHEweight_wgt[460]
1.0	3.0	10.516125	0.8210	4.391335	0.2465	LHEweight_wgt[461]
1.5	-3.0	45.281492	3.845	13.426212	0.7825	LHEweight_wgt[462]
1.5	-2.0	27.606715	2.371	7.809713	0.4574	LHEweight_wgt[463]
1.5	-1.5	20.476088	1.784	5.594971	0.3290	LHEweight_wgt[464]
1.5	-1.25	17.337465	1.518	4.635978	0.2749	LHEweight_wgt[465]
1.5	-1.0	14.483302	1.287	3.775902	0.2244	LHEweight_wgt[466]
1.5	-0.75	11.913599	1.067	3.014744	0.1799	LHEweight_wgt[467]
1.5	-0.5	9.628357	0.874	2.352505	0.1410	LHEweight_wgt[468]
1.5	-0.25	7.627574	0.702	1.789184	0.1081	LHEweight_wgt[469]
1.5	0.0	5.911882	0.5577	1.324946	0.08056	LHEweight_wgt[470]
1.5	0.25	4.479390	0.4365	0.959295	0.05893	LHEweight_wgt[471]
1.5	0.5	3.331988	0.3343	0.692727	0.04277	LHEweight_wgt[472]
1.5	0.75	2.469046	0.2558	0.525078	0.03263	LHEweight_wgt[473]
1.5	1.0	1.890565	0.2003	0.456347	0.02768	LHEweight_wgt[474]
1.5	1.25	1.596544	0.1689	0.486534	0.02864	LHEweight_wgt[475]
1.5	1.5	1.586983	0.1594	0.615638	0.03509	LHEweight_wgt[476]
1.5	2.0	2.421241	0.2105	1.170602	0.06515	LHEweight_wgt[477]
1.5	3.0	7.503280	0.5889	3.467546	0.1930	LHEweight_wgt[478]
0.5	-3.0	27.432685	2.260	8.929074	0.5136	LHEweight_wgt[479]
0.5	-2.0	13.956013	1.160	4.419093	0.2547	LHEweight_wgt[480]
0.5	-1.5	8.924438	0.7478	2.757611	0.1591	LHEweight_wgt[481]
0.5	-1.25	6.835341	0.5726	2.075247	0.1204	LHEweight_wgt[482]
0.5	-1.0	5.030704	0.4273	1.491801	0.08696	LHEweight_wgt[483]
0.5	-0.75	3.510528	0.2999	1.007273	0.05885	LHEweight_wgt[484]
0.5	-0.5	2.274811	0.1982	0.621663	0.03658	LHEweight_wgt[485]
0.5	-0.25	1.323555	0.1189	0.334972	0.01996	LHEweight_wgt[486]
0.5	0.0	0.656969	0.06223	0.147253	0.008986	LHEweight_wgt[487]
0.5	0.25	0.274423	0.02830	0.058342	0.003608	LHEweight_wgt[488]
0.5	0.5	0.176548	0.01778	0.068404	0.003902	LHEweight_wgt[489]
0.5	0.75	0.363132	0.03008	0.177385	0.009854	LHEweight_wgt[490]
0.5	1.0	0.834177	0.06550	0.385283	0.02145	LHEweight_wgt[491]
0.5	1.25	1.589682	0.1241	0.692099	0.03848	LHEweight_wgt[492]
0.5	1.5	2.629647	0.2047	1.097834	0.06136	LHEweight_wgt[493]
0.5	2.0	5.562958	0.4358	2.206057	0.1246	LHEweight_wgt[494]
0.5	3.0	14.843102	1.177	5.609519	0.3172	LHEweight_wgt[495]

**Table 6.2:**  $\kappa_V$  and  $\kappa_t$  combinations generated for the two signal samples and their NLO cross sections. The *tHq* cross section is multiplied by the branching fraction of the enforced leptonic decay of the top quark (0.324). See also Ref. [133].

Sample	$\sigma$ [pb]
TTWJetsToLNu_TuneCUETP8M1_13TeV-amcatnloFXFX-madspin-pythia8	0.2043
TTZToLLNuNu_M-10_TuneCUETP8M1_13TeV-amcatnlo-pythia8	0.2529
ttHJetToNonbb_M125_13TeV_amcatnloFXFX_madspin_pythia8_mWCutfix /store/cmst3/group/susy/gpetrucc/13TeV/u/TTLL_m1to10_LO_NoMS_for76X/	0.2151 0.0283
WGToLNuG_TuneCUETP8M1_13TeV-madgraphMLM-pythia8	585.8
ZGTo2LG_TuneCUETP8M1_13TeV-amcatnloFXFX-pythia8	131.3
TGJets_TuneCUETP8M1_13TeV_amcatnlo_madspin_pythia8	2.967
TGJets_TuneCUETP8M1_13TeV_amcatnlo_madspin_pythia8	2.967
TTGJets_TuneCUETP8M1_13TeV-amcatnloFXFX-madspin-pythia8	3.697
WpWpJJ_EWK-QCD_TuneCUETP8M1_13TeV-madgraph-pythia8	0.03711
ZZZ_TuneCUETP8M1_13TeV-amcatnlo-pythia8	0.01398
WWZ_TuneCUETP8M1_13TeV-amcatnlo-pythia8	0.1651
WZZ_TuneCUETP8M1_13TeV-amcatnlo-pythia8	0.05565
WW_DoubleScattering_13TeV-pythia8	1.64
tZq_ll_4f_13TeV-amcatnlo-pythia8_TuneCUETP8M1	0.0758
ST_tWll_5f_LO_13TeV-MadGraph-pythia8	0.01123
TTTT_TuneCUETP8M1_13TeV-amcatnlo-pythia8	0.009103
WZTo3LNu_TuneCUETP8M1_13TeV-powheg-pythia8	4.4296
ZZTo4L_13TeV_powheg_pythia8	1.256
TTJets_SingleLeptFromTbar_TuneCUETP8M1_13TeV-madgraphMLM-pythia8	182.1754
TTJets_SingleLeptFromT_TuneCUETP8M1_13TeV-madgraphMLM-pythia8	182.1754
TTJets_DiLept_TuneCUETP8M1_13TeV-madgraphMLM-pythia8	87.3
DYJetsToLL_M-10to50_TuneCUETP8M1_13TeV-amcatnloFXFX-pythia8	18610
DYJetsToLL_M-50_TuneCUETP8M1_13TeV-madgraphMLM-pythia8	6024
WJetsToLNu_TuneCUETP8M1_13TeV-amcatnloFXFX-pythia8	61526.7
ST_tW_top_5f_inclusiveDecays_13TeV-powheg-pythia8_TuneCUETP8M1	35.6
ST_tW_antitop_5f_inclusiveDecays_13TeV-powheg-pythia8_TuneCUETP8M1	35.6
ST_t-channel_4f_leptonDecays_13TeV-amcatnlo-pythia8_TuneCUETP8M1	70.3144
ST_t-channel_antitop_4f_leptonDecays_13TeV-powheg-pythia8_TuneCUETP8M1	26.2278
ST_s-channel_4f_leptonDecays_13TeV-amcatnlo-pythia8_TuneCUETP8M1	3.68064
WWTo2L2Nu_13TeV-powheg	10.481

**Table 6.3:** List of background samples used in this analysis (CMSSW 80X). In the first section of the table are listed the samples of the processes for which we use the simulation to extract the final yields and shapes, in the second section the samples of the processes we will estimate from data. The MC simulation is used to design the data driven methods and derive the associated systematics.

Sample	$\sigma$ [pb]
ttWJets_13TeV_madgraphMLM	0.6105
ttZJets_13TeV_madgraphMLM	0.5297/0.692

**Table 6.4:** Leading-order  $t\bar{t}W$  and  $t\bar{t}Z$  samples used in the signal BDT training.

Same-sign dilepton (==2 muons)
HLT_Mu17_TrkIsoVVL_Mu8_TrkIsoVVL_DZ_v*
HLT_Mu17_TrkIsoVVL_TkMu8_TrkIsoVVL_DZ_v*
HLT_IsoMu22_v*
HLT_IsoTkMu22_v*
HLT_IsoMu22_eta2p1_v*
HLT_IsoTkMu22_eta2p1_v*
HLT_IsoMu24_v*
HLT_IsoTkMu24_v*
Same-sign dilepton (==2 electrons)
HLT_Ele23_Ele12_CaloIdL_TrackIdL_IsoVL_DZ_v*
HLT_Ele27_eta2p1_WP Loose_Gsf_v*
HLT_Ele27_WPTight_Gsf_v*
HLT_Ele25_eta2p1_WPTight_Gsf_v*
Same-sign dilepton (==1 muon, ==1 electron)
HLT_Mu23_TrkIsoVVL_Ele8_CaloIdL_TrackIdL_IsoVL_v*
HLT_Mu8_TrkIsoVVL_Ele23_CaloIdL_TrackIdL_IsoVL_v*
HLT_Mu23_TrkIsoVVL_Ele8_CaloIdL_TrackIdL_IsoVL_DZ_v*
HLT_Mu8_TrkIsoVVL_Ele23_CaloIdL_TrackIdL_IsoVL_DZ_v*
HLT_IsoMu22_v*
HLT_IsoTkMu22_v*
HLT_IsoMu22_eta2p1_v*
HLT_IsoTkMu22_eta2p1_v*
HLT_IsoMu24_v*
HLT_IsoTkMu24_v*
HLT_Ele27_WPTight_Gsf_v*
HLT_Ele25_eta2p1_WPTight_Gsf_v*
HLT_Ele27_eta2p1_WP Loose_Gsf_v*
Three lepton and Four lepton
HLT_DiMu9_Ele9_CaloIdL_TrackIdL_v*
HLT_Mu8_DiEle12_CaloIdL_TrackIdL_v*
HLT_TripleMu_12_10_5_v*
HLT_Ele16_Ele12_Ele8_CaloIdL_TrackIdL_v*
HLT_Mu23_TrkIsoVVL_Ele8_CaloIdL_TrackIdL_IsoVL_v*
HLT_Mu23_TrkIsoVVL_Ele8_CaloIdL_TrackIdL_IsoVL_DZ_v*
HLT_Mu8_TrkIsoVVL_Ele23_CaloIdL_TrackIdL_IsoVL_v*
HLT_Mu8_TrkIsoVVL_Ele23_CaloIdL_TrackIdL_IsoVL_DZ_v*
HLT_Ele23_Ele12_CaloIdL_TrackIdL_IsoVL_DZ_v*
HLT_Mu17_TrkIsoVVL_Mu8_TrkIsoVVL_DZ_v*
HLT_Mu17_TrkIsoVVL_TkMu8_TrkIsoVVL_DZ_v*
HLT_IsoMu22_v*
HLT_IsoTkMu22_v*
HLT_IsoMu22_eta2p1_v*
HLT_IsoTkMu22_eta2p1_v*
HLT_IsoMu24_v*
HLT_IsoTkMu24_v*
HLT_Ele27_WPTight_Gsf_v*
HLT_Ele25_eta2p1_WPTight_Gsf_v*
HLT_Ele27_eta2p1_WP Loose_Gsf_v*

**Table 6.5:** Table of high-level triggers that we consider in the analysis.

Category	Scale Factor
ee	$1.01 \pm 0.02$
e $\mu$	$1.01 \pm 0.01$
$\mu\mu$	$1.00 \pm 0.01$
3l	$1.00 \pm 0.03$

**Table 6.6:** Trigger efficiency scale factors and associated uncertainties, shown here rounded to the nearest percent.

## 2202 6.5 Object Identification

2203 In this section, the specific definitions of the physical objects in terms of the numerical  
 2204 values assigned to the reconstruction parameters are presented; thus, the provided  
 2205 details summarize and complement the descriptions presented in previous chapters.  
 2206 The object reconstruction and selection strategy used in this thesis is inherited from  
 2207 the analyses in references [122, 127], thus, the information provided in this section is  
 2208 extracted from those documents unless other references are stated.

### 2209 6.5.1 Jets and $b$ tagging.

2210 In this analysis, jets are reconstructed by clustering PF candidates using the anti- $k_t$   
 2211 algorithm with parameter distance  $\Delta R = 0.4$ ; those charged hadrons that are not  
 2212 consistent with the selected primary vertex are discarded from the clustering. The  
 2213 jet energy is then corrected for the varying response of the detector as a function  
 2214 of transverse momentum  $p_T$  and pseudorapidity  $\eta$ . Jets are selected for use in the  
 2215 analysis only if they have  $p_T > 25$  GeV and are separated from any selected leptons  
 2216 by  $\Delta R > 0.4$ .

2217 Jets coming from the primary vertex and jets coming from pile-up vertices are  
 2218 distinguished using a MVA discriminator based on the differences in the jet shapes,  
 2219 in the relative multiplicity of charged and neutral components, and in the different  
 2220 fraction of transverse momentum which is carried by the hardest components. Jet

2221 tracks are also required to be compatible with the primary vertex.

2222 Jets originated from the hadronization of a  $b$  quark are selected using a MVA  
 2223 likelihood discriminant which uses track-based lifetime information and reconstructed  
 2224 secondary vertices (CSV algorithm). Only jets within the CMS tracker acceptance  
 2225 ( $\eta < 2.4$ ) are identified with this tool. Data samples are used to measure the efficiency  
 2226 of the  $b$  tagging and the probability to misidentify jets from light quarks or gluons;  
 2227 in both cases the measurements are parametrized as a function of the jet  $p_T$  and  $\eta$   
 2228 and later used to correct differences between the data and MC simulation in the  $b$   
 2229 tagging performance, by applying per-jet weights to the simulation, dependent on  
 2230 the jet  $p_T$ ,  $\eta$ ,  $b$  tagging discriminator, and flavor (from simulation truth) [125]. The  
 2231 per-event weight is taken as the product of the per-jet weights, including those of the  
 2232 jets associated to the leptons. The weights are derived on  $t\bar{t}$  and Z+jets events.

2233 Two working points are defined, based on the CSV algorithm output: *loose*' work-  
 2234 ing point (CSV>0.46) with a  $b$  signal tagging efficiency of about 83% and a mistagging  
 2235 rate of about 8%; and *medium* working point (CSV>0.80) with  $b$ -tagging efficiency of  
 2236 about 69% and mistagging rate of order 1% [126]. Tagging of jets from charm quarks  
 2237 have efficiencies of about 40% and 18% for loose and medium working points re-  
 2238 spectively. Separate scale factors are applied to jets originating from bottom/charm  
 2239 quarks and from light quarks in simulated events to match the tagging efficiencies  
 2240 measured in the data.

## 2241 **6.5.2 Missing Energy MET.**

2242 As stated in section 4.4.1.1, the MET vector is calculated as the negative of the vector  
 2243 sum of transverse momenta of all PF candidates in the event and its magnitude is  
 2244 referred to as  $E_T^{miss}$ . Due to pile-up interactions, the performance in determining

2245 MET is degraded; in order to correct for that, the energy from the selected jets and  
 2246 leptons that compose the event is assigned to the variable  $H_T^{miss}$ . It is calculated in  
 2247 the same way as  $E_T^{miss}$  and although it has worse resolution than  $E_T^{miss}$ , it is more  
 2248 robust in the sense that it does not rely on the soft part of the event. The event  
 2249 selection uses a linear discriminator based on the two variables given by

$$E_T^{miss} LD = 0.00397 * E_T^{miss} + 0.00265 * H_T^{miss} \quad (6.1)$$

2250 taking advantage of the fact that the correlation between  $E_T^{miss}$  and  $H_T^{miss}$  is less  
 2251 for events with instrumental missing energy than for events with real missing energy.  
 2252 The working point  $E_T^{miss} LD > 0.2$  was chosen to ensure a good signal efficiency while  
 2253 keeping a good background rejection.

### 2254 6.5.3 Lepton reconstruction and identification

2255 Two types of leptons are defined in this analysis: *signal leptons* are those coming from  
 2256  $W, Z$  and  $\tau$  decays which usually are isolated from other particles; *background leptons*  
 2257 are defined as leptons produced in  $b$  hadron decays, light-jets misidentification, and  
 2258 photon conversions.

2259 The process of reconstruction and identification of electron and muon candidates  
 2260 was described in chapter4, hence, the identification variables used in order to retain  
 2261 the highest possible efficiency for signal leptons while maximizing the rejection of  
 2262 background leptons are listed and described in the following sections <sup>2</sup>.

2263 The identification variables include not only observables related directly to the re-  
 2264 constructed leptons themselves, but also to the clustered energy deposits and charged  
 2265 particles in a cone around the lepton direction (jet-related variables); an initial loose

---

<sup>2</sup> the studies performed to optimize the identification are far from the scope of this thesis, therefore, only general descriptions are provided

2266 preselection of leptons candidates is performed and then an MVA discriminator, re-  
 2267 ferred to as *lepton MVA* discriminator, is used to distinguish signal leptons from  
 2268 background leptons.

2269 **Muons.**

2270 The Physics Objects Groups (POG) at CMS, are in charge of studying and defining  
 2271 the set of selection criteria applied on the course of reconstruction and identification  
 2272 of particles. These selection criteria are implemented in the CMS framework in the  
 2273 form of several object identification working points according to the strength of the  
 2274 requirements.

2275 The muon candidates are reconstructed by combining information from the tracker  
 2276 system and the muon detection system of CMS detector and the POG defined three  
 2277 working points for muon identification *MuonID* [128];

- 2278     • *POG Loose Muon ID* is a particle identified as a muon by the PF event re-  
 2279       construction and also reconstructed either as a global-muon or as an arbitrated  
 2280       tracker-muon. This identification criteria is designed to be highly efficient for  
 2281       prompt muons and for muons from heavy and light quark decays; it can be com-  
 2282       plemented by applying impact parameter cuts in analyses with prompt muon  
 2283       signals.
- 2284     • *POG Medium Muon ID* is a Loose muon with additional track-quality and  
 2285       muon-quality (spatial matching between the individual measurements in the  
 2286       tracker and the muon system) requirements. This identification criteria is de-  
 2287       signed to be highly efficient in the separation of the muons coming from decay  
 2288       in flight of heavy quarks and muons coming from B meson decays as well as  
 2289       prompt muons. An additional category *MVA Prompt ID* is defined in this iden-

2290 tification criteria directed to discriminated muons from B mesons and prompt  
 2291 muons (from W,Z and  $\tau$  decays). The Medium ID provides the same fake rate as  
 2292 the Tight Muon ID but a higher efficiency on prompt and B-decays muons. [129]

- 2293 • *POG Tight Muon ID* is a global muon with additional muon-quality require-  
 2294 ments Tight Muon ID selects a subset of the PF muons.

2295 Only muons within the muon system acceptance  $|\eta| < 2.4$  and minimum  $p_T$  of 5  
 2296 GeV are considered.

2297 **Electrons.**

2298 Electrons are reconstructed using information from the tracker and from the electro-  
 2299 magnetic calorimeter and identified by an MVA algorithm (*MVA eID* discriminant)  
 2300 using the shape of the calorimetric shower variables like the shape in  $\eta$  and  $\phi$ , the clus-  
 2301 ter circularity, widths along  $\eta$  and  $\phi$ ; track-cluster matching variables like  $E_{tot}/p_{in}$ ,  
 2302  $E_{Ele}/p_{out}$ ,  $\Delta\eta_{in}$ ,  $\Delta\eta_{out}$ ,  $\Delta\phi_{in}$ ,  $1/E - 1/p$ ; and track quality variables like  $\xi^2$  of the  
 2303 GSF tracks, the number of hits used by the GSF filter [130].

2304 A loose selection based on  $\eta$ -dependent cuts on this discriminant is used to prese-  
 2305 lect electron candidates, the full shape of the discriminant is used in the lepton MVA  
 2306 selection to separate signal leptons from background leptons (described in section  
 2307 6.5.3).

2308 In order to reject electrons from photon conversions, electron candidates with  
 2309 missing hits in the pixel tracker layers or matched to a conversion secondary vertex  
 2310 are discarded. Electrons are selected for the analysis if they have  $p_T > 7$  GeV and  
 2311 are located within the tracker system acceptance region ( $|\eta| < 2.5$ ).

2312 **Lepton vertexing and pile-up rejection.**

2313 The impact parameter in the transverse plane  $d_0$ , impact parameter along the z  
 2314 axis  $d_z$ , and the impact parameter significance in the detector space  $SIP_{3D}$ , are  
 2315 considered to perform the identification and rejection of pile-up, misreconstructed  
 2316 tracks, and background leptons from b-hadron decays; pile-up and misreconstructed  
 2317 track mitigation is achieved by imposing loose cuts on the impact parameter variables.  
 2318 The full shape of the those variables is used in a lepton MVA classifier to achieve the  
 2319 best separation between the signal and the background leptons.

2320 **Lepton isolation.**

2321 PF is able to recognize leptons from two different sources: on one side, leptons from  
 2322 the decays of heavy particles, such as W and Z bosons, which are normally isolated  
 2323 in space from the hadronic activity in the event; on the other side, leptons from the  
 2324 decays of hadrons and jets misidentified as leptons, which are not isolated as the  
 2325 former. For highly boosted systems, like the lepton and the  $b$ -jet generated in the  
 2326 semileptonic decay of a boosted top, the decay products tend to be more closer and  
 2327 sometimes they even overlap; thus, the PF standard definition of isolation in terms of  
 2328 the separation between the lepton candidates and other PF objects in the  $\eta$ - $\phi$  plane,

$$\Delta R = \sqrt{(\eta^l - \eta^i)^2 + (\phi^l - \phi^i)^2} < 0.3 \quad (6.2)$$

2329 which considers all the neutral, charged hadrons and photons in a cone around the  
 2330 leptons, is refocused to the local isolation of the leptons through the mini-isolation  
 2331  $I_{mini}$  [131] defined as the sum of particle flow candidates  $p_T$  within a cone around

2332 the lepton, corrected for the effects of pileup and divided by the lepton  $p_T$

$$I_{mini} = \frac{\sum_R p_T(h^\pm) - \max\left(0, \sum_R p_T(h^0) + p_T(\gamma) - \rho \mathcal{A} \left(\frac{R}{0.3}\right)^2\right)}{p_T(l)} \quad (6.3)$$

2333 where  $\rho$  is the pileup energy density,  $h^\pm, h^0, \gamma, l$ , represent the charged hadron, neutral  
 2334 hadrons, photons, and the lepton, respectively. The radius  $R$  of the cone depends on  
 2335 the  $p_T$  of the lepton according to

$$R = \frac{10\text{GeV}}{\min(\max(p_T(l), 50\text{GeV}), 200\text{GeV})}, \quad (6.4)$$

2336 The  $p_T$  dependence of the cone size allows for greater signal efficiency. Setting a  
 2337 cut on  $I_{mini}$  below a given threshold ensures that the lepton is locally isolated, even  
 2338 in boosted systems. The effect of pileup is mitigated using the so-called effective area  
 2339 correction  $\mathcal{A}$  listed in Table 6.7.

$ \eta $ range	$\mathcal{A}(e)$ neutral/charged	$\mathcal{A}(\mu)$ neutral/charged
0.0 - 0.8	0.1607 / 0.0188	0.1322 / 0.0191
0.8 - 1.3	0.1579 / 0.0188	0.1137 / 0.0170
1.3 - 2.0	0.1120 / 0.0135	0.0883 / 0.0146
2.0 - 2.2	0.1228 / 0.0135	0.0865 / 0.0111
2.2 - 2.5	0.2156 / 0.0105	0.1214 / 0.0091

**Table 6.7:** Effective areas, for electrons and muons used to mitigate the effect of pileup by using the so-called effective area correction.

2340 A loose cut on  $I_{mini}$  is applied to pre-select the muon and electron candidates;  
 2341 however, the full shape is used in the lepton MVA discriminator when performing the  
 2342 signal lepton selection.

2343 **Jet-related variables.**

2344 In order to reject misidentified leptons from  $b$ -jets, mostly coming from  $t\bar{t}$ +jets,  
 2345 Drell-Yan+jets, and W+jets events, the vertexing and isolation described in previous  
 2346 sections are complemented with additional variables related to the closest recon-  
 2347 structed jet to the lepton, i.e., the PF jets reconstructed<sup>3</sup> around the leptons with  
 2348  $\Delta R = \sqrt{(\eta^l - \eta^{jet})^2 + (\phi^l - \phi^{jet})^2} < 0.5$ . The identification variables used in the lep-  
 2349 ton MVA discriminator are the ratio  $p_T^l/p_T^{jet}$ , the CSV b-tagging discriminator value  
 2350 of the jet, the number of charged tracks of the jet, and the relative  $p_T$  given by

$$p_T^{rel} = \frac{(\vec{p}_{jet} - \vec{p}_l) \cdot \vec{p}_l}{\|\vec{p}_{jet} - \vec{p}_l\|}. \quad (6.5)$$

2351 **LeptonMVA discriminator.**

2352 Electrons and muons passing the basic selection process described above are referred  
 2353 to as *loose leptons*. Additional discrimination between signal leptons and background  
 2354 leptons is crucial considering that the rate of  $t\bar{t}$  production is much larger than the  
 2355 signal, hence, an overwhelming background from  $t\bar{t}$  production. To maximally ex-  
 2356 ploit the available information in each event to that end, the dedicated lepton MVA  
 2357 discriminator, based on a boosted decision tree (BDT) algorithm, has been built so  
 2358 that all the identification variables can be used together.

2359 The lepton MVA discriminator training is performed using simulated signal Loose  
 2360 leptons from the  $t\bar{t}H$  MC sample and fake leptons from the  $t\bar{t}$  +jets MC sample,  
 2361 separately for muons and electrons. The input variables used include vertexing, iso-  
 2362 lation and jet-related variables, the  $p_T$  and  $\eta$  of the lepton, the electron MVA eID  
 2363 discriminator and the muon segment-compatibility variables. An additional require-  
 2364 ment known as *tight-charge* requirement, is imposed by comparing two independent

---

<sup>3</sup> charged hadrons from PU vertices are not removed prior to the jet clustering.

measurement of the charge, one from the ECAL supercluster and the other from the tracker; thus, the consistency in the measurements of the electron charge is ensured so that events with a wrong electron charge assignment are rejected; this variable is particularly used in the 2lss channel to suppress opposite-sign events for which the charge of one of the leptons has been mismeasured. The tight-charge requirement for muons is represented by the requirement of a consistently well measured track transverse momentum given by  $\Delta p_T/p_T < 0.2$ . Leptons are selected for the final analysis if they pass a given threshold of the BDT output, and are referred to as *tight leptons* in the following.

The validation of the lepton MVA algorithm and the lepton identification variables is performed using data in various control regions; the details about that validation are not discussed here but can be found in Reference [127].

### Selection definitions

Electron and muon object identification is defined in three different sets of selections criteria; the *Loose*, *Fakeable Object*, and *Tight* selection. These three levels of selection are designed to serve for event level vetoes, the fake rate estimation application region, and the final signal selection, respectively. The  $p_T$  of fakeable objects is defined as  $0.85 \times p_T(\text{jet})$ , where the jet is the one associated to the lepton object. This mitigates the dependence of the fake rate on the momentum of the fakeable object and thereby improves the precision of the method.

Tables 6.8 and 6.9 list the full criteria for the different selections of muons and electrons.

In addition to the previously defined requirements for jets, they are required to be separated from any lepton candidates passing the fakeable object selections by  $\Delta R > 0.4$ .

Cut	Loose	Fakeable object	Tight
$ \eta  < 2.4$	✓	✓	✓
$p_T$	$> 5\text{GeV}$	$> 15\text{GeV}$	$> 15\text{GeV}$
$ d_{xy}  < 0.05$ (cm)	✓	✓	✓
$ d_z  < 0.1$ (cm)	✓	✓	✓
$\text{SIP}_{3D} < 8$	✓	✓	✓
$I_{\text{mini}} < 0.4$	✓	✓	✓
is Loose Muon	✓	✓	✓
jet CSV	—	$< 0.8484$	$< 0.8484$
is Medium Muon	—	—	✓
tight-charge	—	—	✓
lepMVA $> 0.90$	—	—	✓

**Table 6.8:** Requirements on each of the three muon selections. In the cases where the cut values change between the selections, those values are listed in the table. Otherwise, whether the cut is applied is indicated.

Cut	Loose	Fakeable Object	Tight
$ \eta  < 2.5$	✓	✓	✓
$p_T$	$> 7\text{GeV}$	$> 15\text{GeV}$	$> 15\text{GeV}$
$ d_{xy}  < 0.05$ (cm)	✓	✓	✓
$ d_z  < 0.1$ (cm)	✓	✓	✓
$\text{SIP}_{3D} < 8$	✓	✓	✓
$I_{\text{mini}} < 0.4$	✓	✓	✓
MVA eID $> (0.0, 0.0, 0.7)$	✓	✓	✓
$\sigma_{in\eta} < (0.011, 0.011, 0.030)$	—	✓	✓
H/E $< (0.10, 0.10, 0.07)$	—	✓	✓
$\Delta\eta_{in} < (0.01, 0.01, 0.008)$	—	✓	✓
$\Delta\phi_{in} < (0.04, 0.04, 0.07)$	—	✓	✓
$-0.05 < 1/E - 1/p < (0.010, 0.010, 0.005)$	—	✓	✓
$p_T^{\text{ratio}}$	—	$> 0.5^\dagger / -$	—
jet CSV	—	$< 0.3^\dagger / < 0.8484$	$< 0.8484$
tight-charge	—	—	✓
conversion rejection	—	—	✓
Number of missing hits	$< 2$	$= 0$	$= 0$
lepton MVA $> 0.90$	—	—	✓

**Table 6.9:** Criteria for each of the three electron selections. In cases where the cut values change between selections, those values are listed in the table. Otherwise, whether the cut is applied is indicated. In some cases, the cut values change for different  $\eta$  ranges. These ranges are  $0 < |\eta| < 0.8$ ,  $0.8 < |\eta| < 1.479$ , and  $1.479 < |\eta| < 2.5$  and the respective cut values are given in the form (value<sub>1</sub>, value<sub>2</sub>, value<sub>3</sub>). For the two  $p_T^{\text{ratio}}$  and CSV rows, the cuts marked with a  $\dagger$  are applied to leptons that fail the lepton MVA cut, while the loose cut value is applied to those that pass the lepton MVA cut.

### 2390 6.5.4 Lepton selection efficiency

2391 Efficiencies of reconstruction and selecting loose leptons are measured both for muons  
 2392 and electrons using a tag and probe method on both data and MC, using  $Z \rightarrow \ell^+ \ell^-$   
 2393 [132]. The scale factors are derived from the ratio of efficiencies  $\varepsilon_i(p_T, \eta)$  measured  
 2394 for a given lepton in data/MC, according to

$$\rho(p_T, \eta) = \frac{\varepsilon_{\text{data}}(p_T, \eta)}{\varepsilon_{\text{MC}}(p_T, \eta)}. \quad (6.6)$$

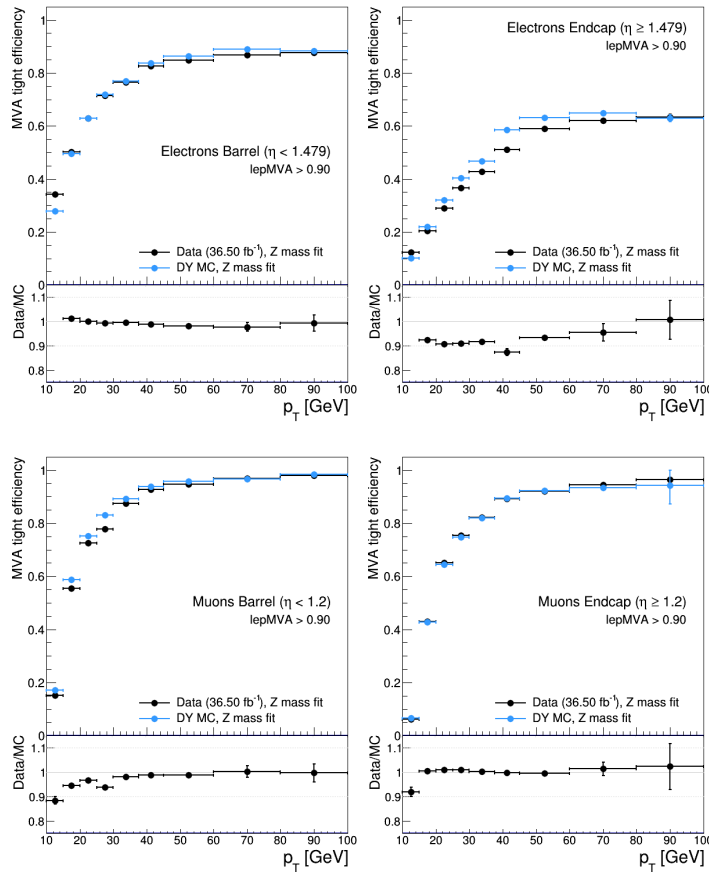


**Figure 6.3:** Tight vs loose selection efficiencies for electrons (top), and muons (bottom), for the 2lss definition, i.e., including the tight-charge requirement.

2395 The scale factor for each event is used to correct the weight of the event in the

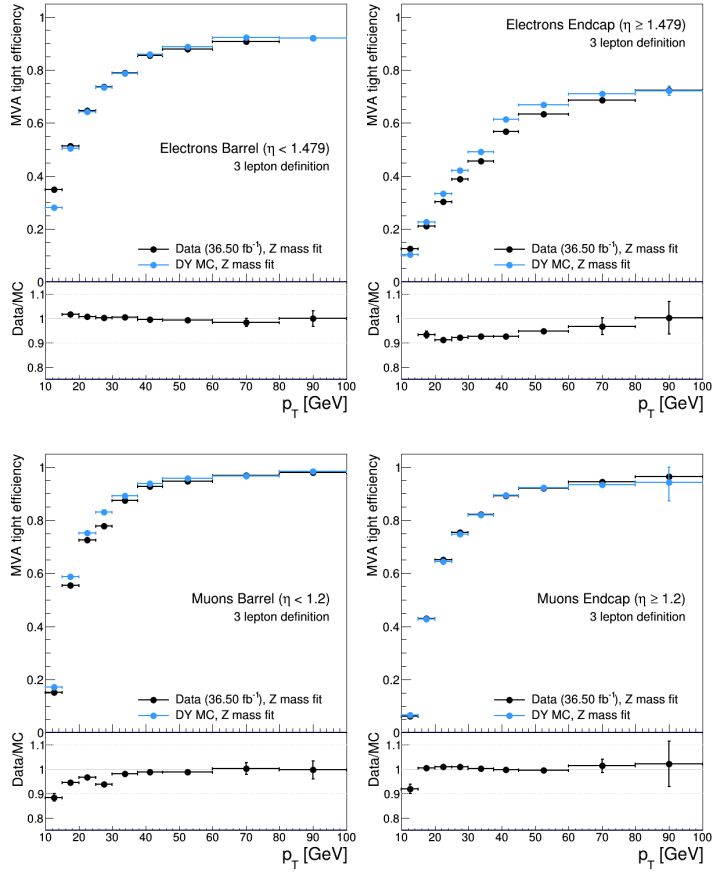


**Figure 6.4:** Tight vs loose selection efficiencies for electrons (top), and muons (bottom), for the 3l channel not including the tight-charge requirement.

2396 full sample; therefore, the full simulation correction is given by the product of all  
 2397 the individual scale factors. The scale factors used in this thesis are inherited from  
 2398 the reference [127] which in turns inherited them from leptonic SUSY analyses using  
 2399 equivalent lepton selections.

2400 The efficiency of applying the tight selection as defined in Tables 6.8 and 6.9, on the  
 2401 loose leptons are determined by using a tag and probe method on a sample of Drell-  
 2402 Yan enriched events. Figures 6.3 and 6.4 show the efficiencies for the 2lss channel and  
 2403 3l channel respectively. Efficiencies in the 2lss channel have been produced including  
 2404 the tight-charge requirement, while for the 3l channel it is not included. Number

2405 of passed and failed probes are determined from a fit to the invariant mass of the  
 2406 dilepton system.

2407 Simulation is corrected using these scale factors; note that they depends on  $\eta$  and  
 2408  $p_T$ .

2409 **6.6 Event selection**

2410 .

2411 .

2412 .

2413 .

2414 .

2415 .

2416 .

2417 .

2418 .

2419 . . .

2420 The analysis is designed to efficiently identify and select prompt leptons from  
 2421 on-shell W and

2422 Z boson decays and to reject non-prompt leptons from b quark decays and spurious  
 2423 lepton

2424 signatures from hadronic jets. Events are then selected in the various lepton  
 2425 channels, and are

2426 required to contain hadronic jets, some of which must be consistent with b quark  
 2427 hadronization. Finally, the signal yield is extracted by simultaneously fitting the  
 2428 output of two dedicated

2429 multivariate discriminants (trained to separate the  $tHq$  signal from the two dom-  
 2430 inant backgrounds) in all categories

2431 . Multivariate techniques are used to discriminate the signal from the dominant  
 2432 backgrounds. The analysis yields a 95% confidence level (C.L.) upper limit on the  
 2433 combined  $tH + ttH$  production cross section times branching ratio of 0.64 pb, with  
 2434 an expected limit of 0.32 pb, for a scenario with  $kt = \sqrt{1.0}$  and  $kV = 1.0$ . Values  
 2435 of  $kt$  outside the range of  $\sqrt{1.25}$  to  $\sqrt{1.60}$  are excluded at 95% C.L., assuming  $kV$   
 2436 = 1.0.

2437 Dont forget to mention previous constrains to ct check reference ?? and references  
 2438 <https://link.springer.com/content/pdf/10.1007%2FJHEP01%282013%29088.pdf> (para-  
 2439 graph after eq 2)

2440 We selects events with three leptons and a  $b$  tagged jet in the final state. The  $tHq$   
 2441 signal contribution is then determined in a fit of the observed data to two multivariate  
 2442 classifier outputs, each trained to discriminate against one of the two dominant back-  
 2443 grounds of events with non-prompt leptons from  $t\bar{t}$  and of associated production of  $t\bar{t}$   
 2444 and vector bosons ( $t\bar{t}W$ ,  $t\bar{t}Z$ ). The fit result is then used to set an upper limit on the  
 2445 combined  $t\bar{t}H$ ,  $tHq$  and  $tHW$  production cross section, as a function of the relative  
 2446 coupling strengths of Higgs and top quark and Higgs and W boson, respectively.

## 2447 6.7 Background predictions

2448 The modeling of reducible and irreducible backgrounds in this analysis uses the exact  
 2449 methods, analysis code, and ROOT trees used for the  $t\bar{t}H$  multilepton analysis. We  
 2450 give a brief description of the methods and refer to the documentation of that analysis  
 2451 in Refs. [122, 127] for any details.

2452 The backgrounds in three-lepton final states can be split in two broad categories:

irreducible backgrounds with genuine prompt leptons (i.e. from on-shell W and Z boson decays); and reducible backgrounds where at least one of the leptons is “non-prompt”, i.e. produced within a hadronic jet, either a genuine lepton from heavy flavor decays, or simply mis-reconstructed jets.

Irreducible backgrounds can be reliably estimated directly from Monte-Carlo simulated events, using higher-order cross sections or data control regions for the overall normalization. This is done in this analysis for all backgrounds involving prompt leptons:  $t\bar{t}W$ ,  $t\bar{t}Z$ ,  $t\bar{t}H$ ,  $WZ$ ,  $ZZ$ ,  $W^\pm W^\pm qq$ ,  $t\bar{t}t\bar{t}$ ,  $tZq$ ,  $tZW$ ,  $WWW$ ,  $WWZ$ ,  $WZZ$ ,  $ZZZ$ .

Reducible backgrounds, on the other hand, are not well predicted by simulation, and are estimated using data-driven methods. In the case of non-prompt leptons, a fake rate method is used,

Additional identification criteria are applied for electrons with  $p_T$  greater than 30 GeV to mimic the identification applied at trigger level in order to ensure consistency between the measurement region and application region of the fake-rate.

where the contribution to the final selection is estimated by extrapolating from a sideband (or “application region”) with a looser lepton definition (the fakeable object definitions in Tabs. 6.8 and 6.9) to the signal selection. The tight-to-loose ratios (or “fake rates”) are measured in several background dominated data events with dedicated triggers, subtracting the residual prompt lepton contribution using MC. Non-prompt leptons in our signal regions are predominantly produced in  $t\bar{t}$  events, with a much smaller contribution, from Drell–Yan production. The systematic uncertainty on the normalization of the non-prompt background estimation is on the order of 50%, and thereby one of the dominant limitations on the performance of multilepton analyses in general and this analysis in particular. It consists of several individual sources, such as the result of closure tests of the method using simulated

2479 events, limited statistics in the data control regions due to necessary prescaling of  
 2480 lepton triggers, and the uncertainty in the subtraction of residual prompt leptons  
 2481 from the control region.

2482 The fake background where the leptons pass the looser selection are weighted  
 2483 according to how many of them fail the tight criteria. Events with a single failing  
 2484 lepton are weighted with the factor  $f/(1-f)$  for the estimate to the tight selection  
 2485 region, where  $f$  is the fake rate. Events with two failing leptons are given the negative  
 2486 weight  $-f_i f_j / (1-f_i)(1-f_j)$ , and for three leptons the weight is positive and equal  
 2487 to the product of  $f/(1-f)$  factor evaluated for each failing lepton.

2488 Figures 6.5 show the distributions of some relevant kinematic variables, normalized  
 2489 to the cross section of the respective processes and to the integrated luminosity.

## 2490 6.8 Signal discrimination

2491 The  $tHq$  signal is separated from the main backgrounds using a boosted decision  
 2492 tree (BDT) classifier, trained on simulated signal and background events. A set  
 2493 of discriminating variables are given as input to the BDT which produces a output  
 2494 distribution maximizing the discrimination power. Table 6.10 lists the input variables  
 2495 used while Figures 6.6 show their distributions for the relevant signal and background  
 2496 samples, for the three lepton channel. Two BDT classifiers are trained for the two  
 2497 main backgrounds expected in the analysis: events with prompt leptons from  $t\bar{t}W$  and  
 2498  $t\bar{t}Z$  (also referred to as  $t\bar{t}V$ ), and events with non-prompt leptons from  $t\bar{t}$ . The datasets  
 2499 used in the training are the  $tHq$  signal (see Tab. 6.1), and LO MADGRAPH samples  
 2500 of  $t\bar{t}W$  and  $t\bar{t}Z$ , in an admixture proportional to their respective cross sections (see  
 2501 Tab. 6.4).

2502 The MVA analysis consist of two stages: first a “training” where the MVA method

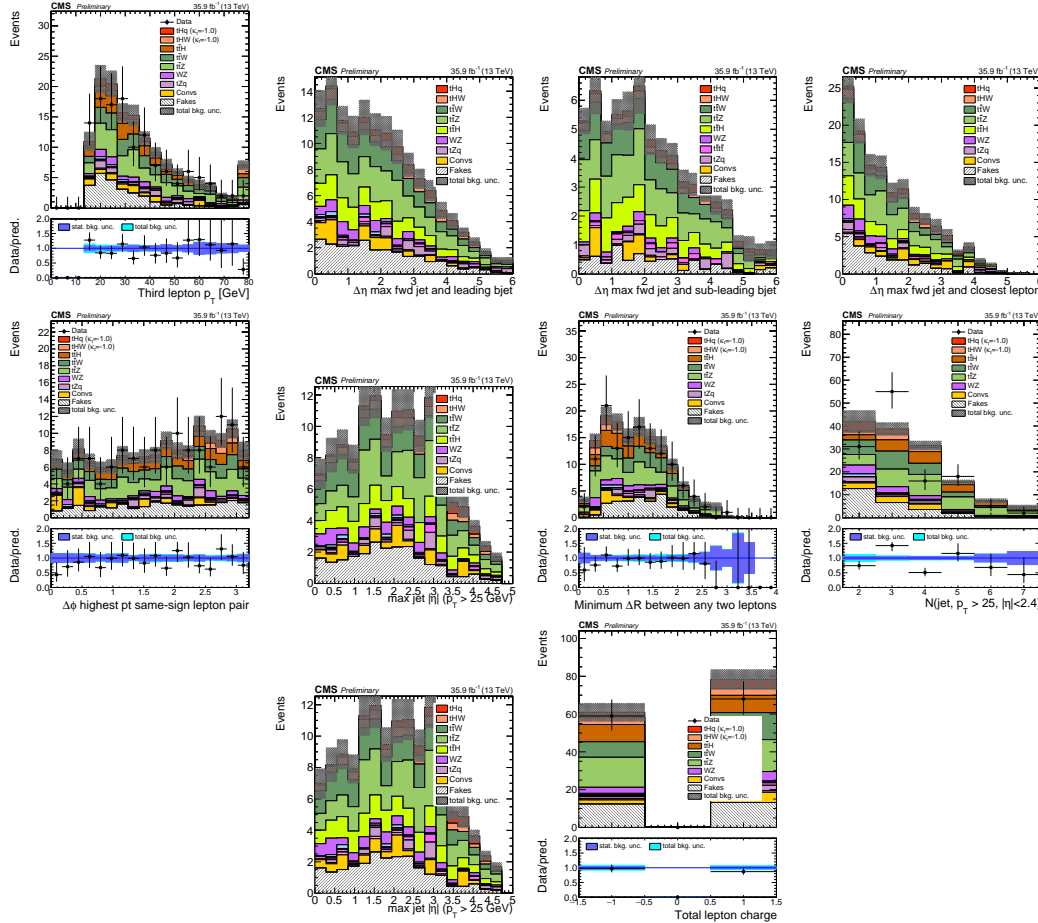


**Figure 6.5:** Distributions of input variables to the BDT for signal discrimination, three lepton channel, normalized to their cross section and to  $35.9\text{fb}^{-1}$ .

is trained to discriminate between simulated signal and background events, then a “test” stage where the trained algorithm is used to classify different events from the samples. The sample is obtained from a pre-selection (see Tab. ?? with pre-selection cuts). Figures 6.7 show the input variables distributions as seen by the MVA algorithm. Note that in contrast to the distributions in Fig. 6.6 only the main backgrounds ( $t\bar{t}$  from simulation,  $t\bar{t}V$ ) are included.

Note that splitting the training in two groups reveals that some variables show opposite behavior for the two background sources; potentially screening the discrimination power if they were to be used in a single discriminant. For some other variables

Variable name	Description
nJet25	Number of jets with $p_T > 25$ GeV, $ \eta  < 2.4$
MaxEtaJet25	Maximum $ \eta $ of any (non-CSV-loose) jet with $p_T > 25$ GeV
totCharge	Sum of lepton charges
nJetEta1	Number of jets with $ \eta  > 1.0$ , non-CSV-loose
detaFwdJetBJet	$\Delta\eta$ between forward light jet and hardest CSV loose jet
detaFwdJet2BJet	$\Delta\eta$ between forward light jet and second hardest CSV loose jet (defaults to -1 in events with only one CSV loose jet)
detaFwdJetClosestLep	$\Delta\eta$ between forward light jet and closest lepton
dphiHighestPtSSPair	$\Delta\phi$ of highest $p_T$ same-sign lepton pair
minDRll	minimum $\Delta R$ between any two leptons
Lep3Pt/Lep2Pt	$p_T$ of the 3 <sup>rd</sup> lepton (2 <sup>nd</sup> for ss2l)

**Table 6.10:** MVA input discriminating variables

2512 the distributions are similar in both background cases.

2513 From table 6.10, it is clear that the input variables are correlated to some extend.  
 2514 These correlations play an important role for some MVA methods like the Fisher  
 2515 discriminant method in which the first step consist of performing a linear transfor-  
 2516 mation to an phase space where the correlations between variables are removed. In  
 2517 case a boosted decision tree (BDT) method however, correlations do not affect the  
 2518 performance. Figure 6.9 show the linear correlation coefficients for signal and back-  
 2519 ground for the two training cases (the signal values are identical by construction). As  
 2520 expected, strong correlations appears for variables related to the forward jet activity.  
 2521 Same trend is seen in case of the same sign dilepton channel in Figure ??.

### 2522 6.8.1 Classifiers response

2523 Several MVA algorithms were evaluated to determine the most appropriate method  
 2524 for this analysis. The plots in Fig. 6.10 (top) show the background rejection as a  
 2525 function of the signal efficiency for  $t\bar{t}$  and  $t\bar{t}V$  trainings (ROC curves) for the different

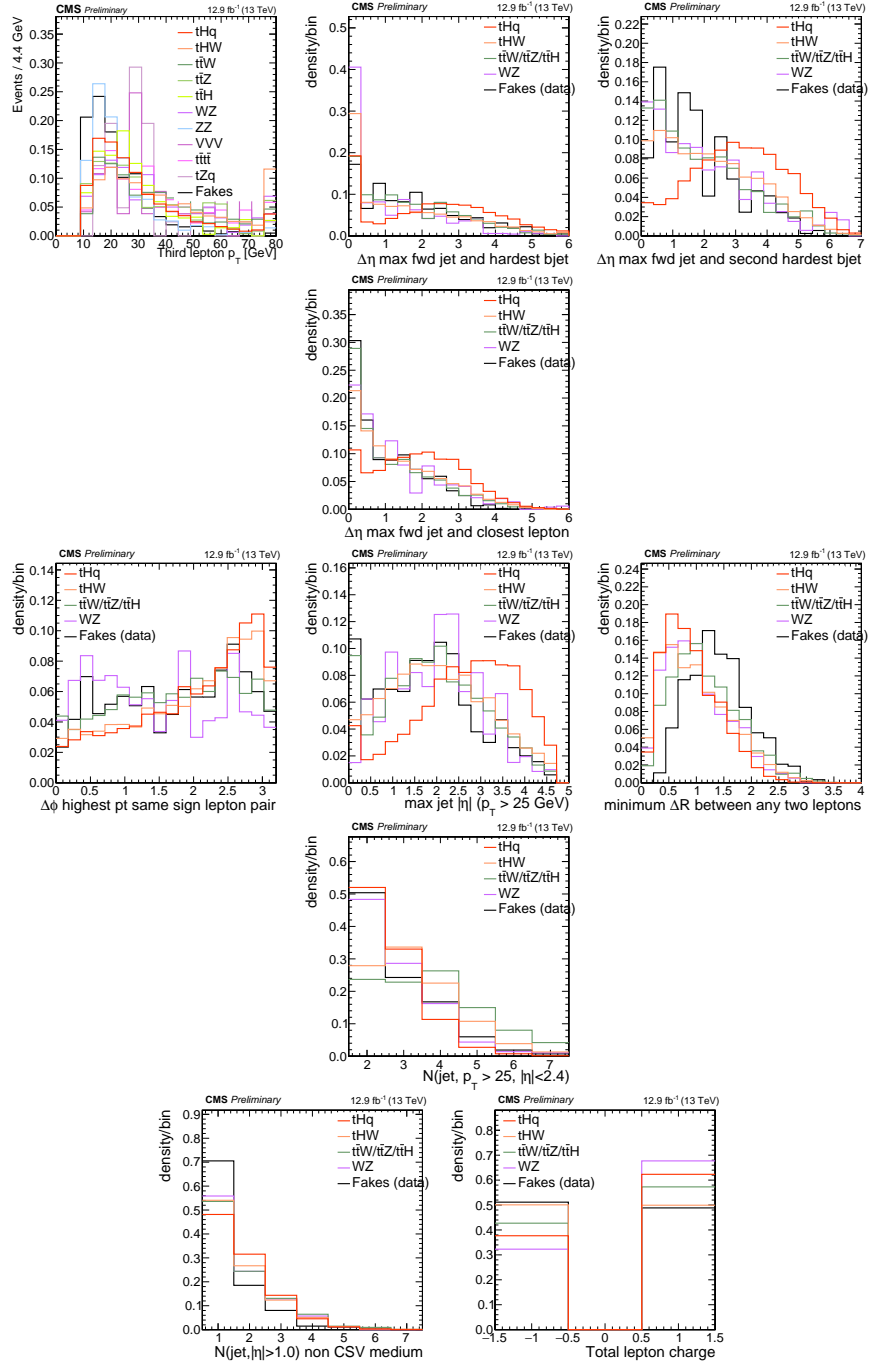


**Figure 6.6:** Distributions of input variables to the BDT for signal discrimination, three lepton channel.

algorithms that were evaluated.

In both cases the gradient boosted decision tree (“BDT<sub>A</sub>\_GRAD”) classifier offers

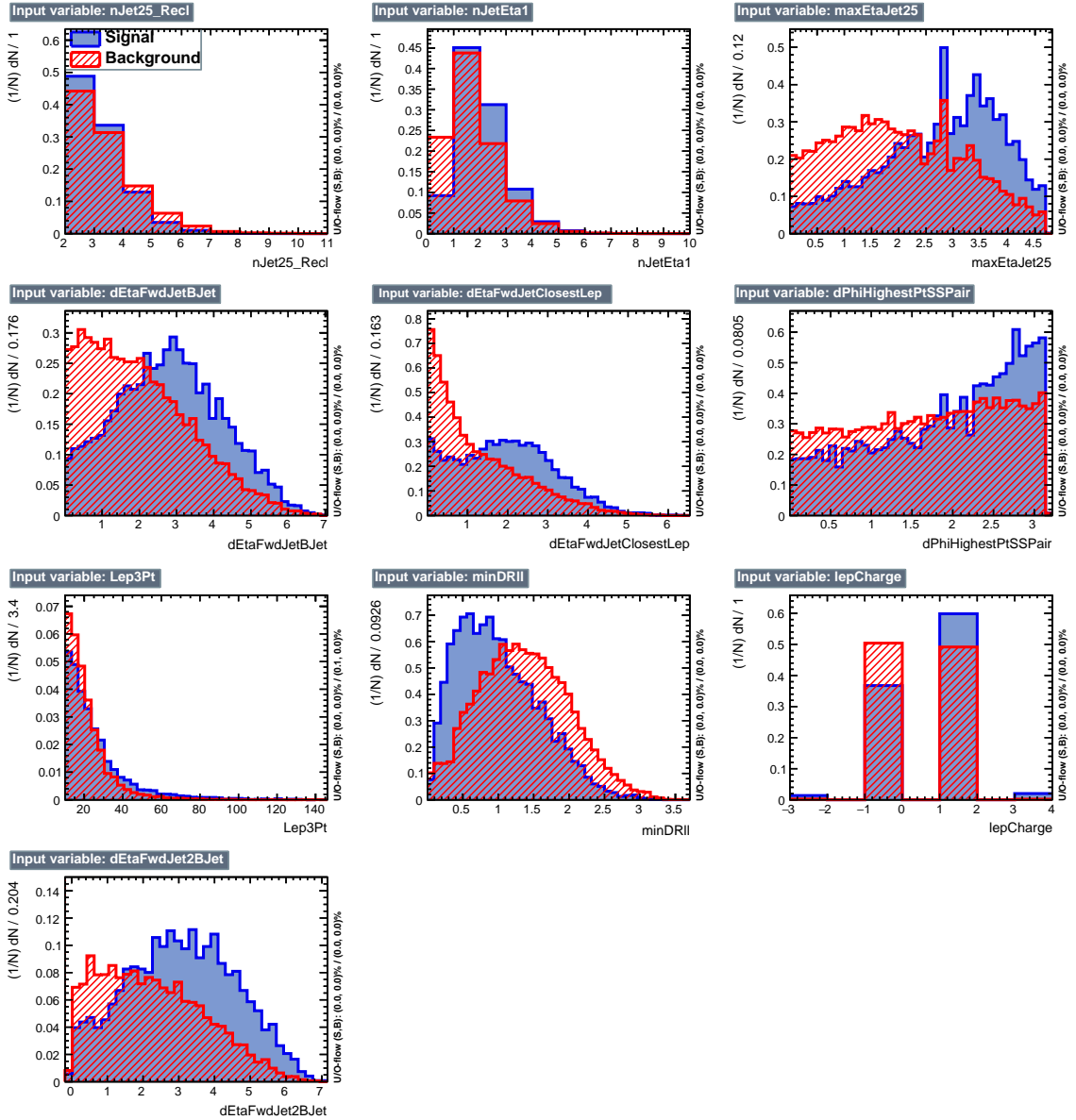


**Figure 6.7:** BDT inputs as seen by TMVA (signal, in blue, is  $tHq$ , background, in red, is  $t\bar{t}$ ) for the three lepton channel, discriminated against  $t\bar{t}$  (fakes) background.

the best results, followed by an adaptive BDT classifier (“BDTA”). The BDTA\_GRAD classifier output distributions for signal and backgrounds are shown on the bottom of Fig. 6.10. As expected, a good discrimination power is obtained using default discriminator parameter values, with minimal overtraining. TMVA provides a ranking of the input variables by their importance in the classification process, shown in Tab. 6.11.

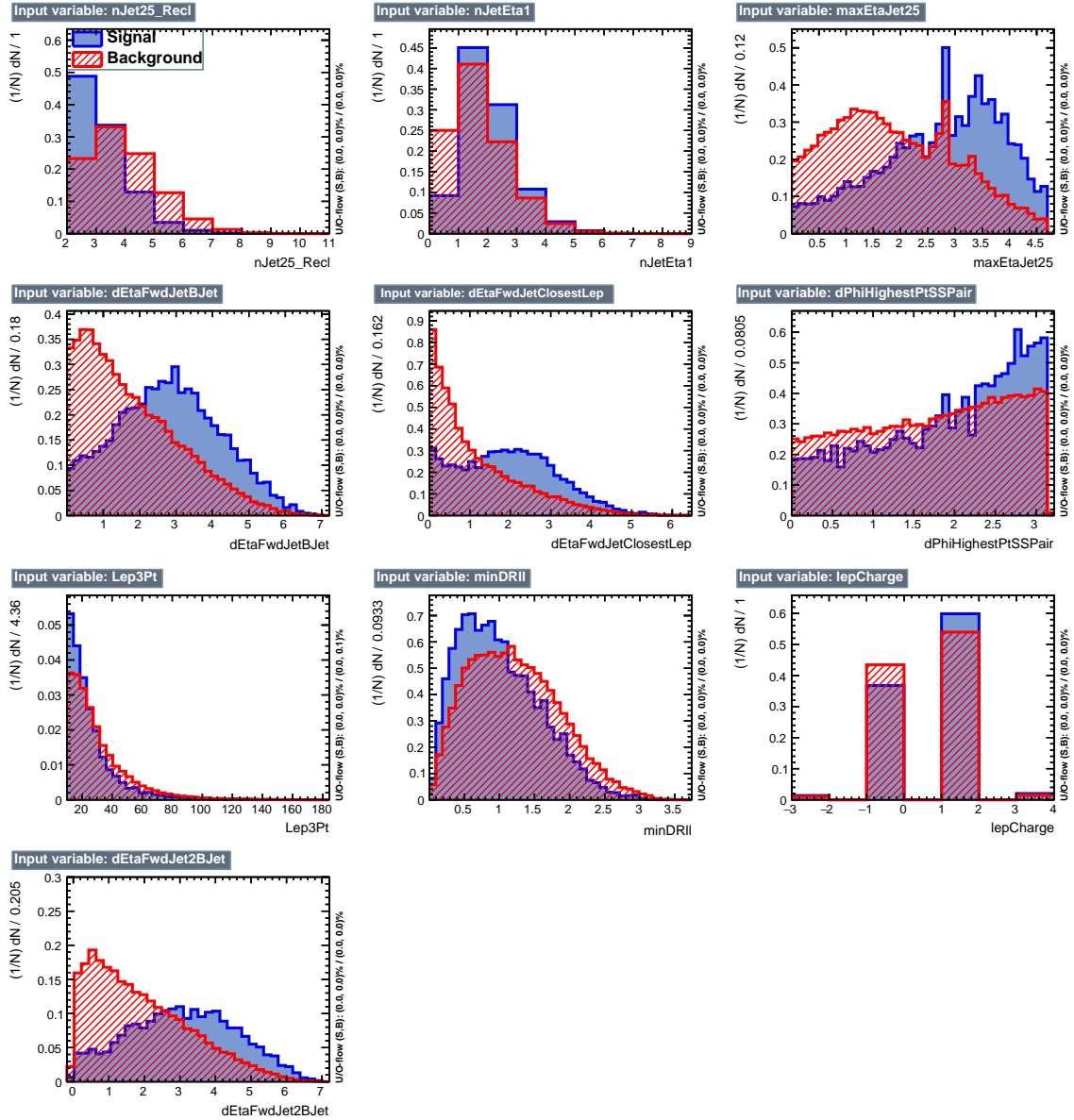


**Figure 6.8:** BDT inputs as seen by TMVA (signal, in blue, is  $tHq$ , background, in red, is  $t\bar{t}W+t\bar{t}Z$ ) for the three lepton channel, discriminated against  $t\bar{t}V$  background.

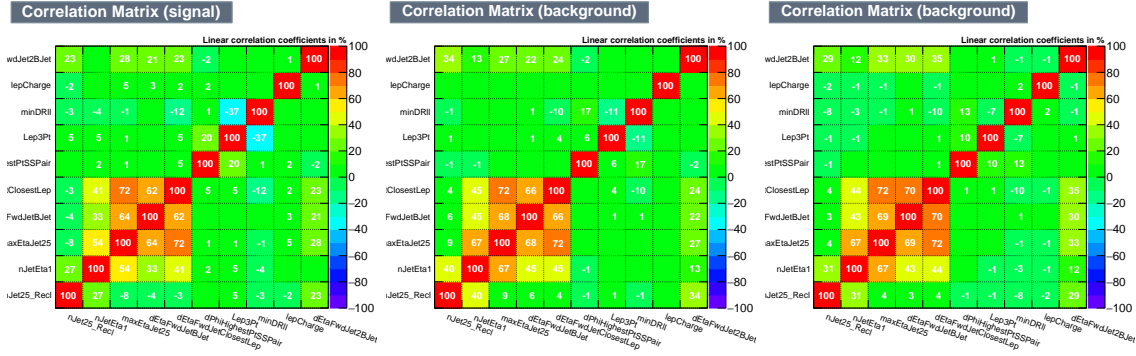


**Figure 6.9:** Signal (left),  $t\bar{t}$  background (middle), and  $t\bar{t}V$  background (right.) correlation matrices for the input variables in the TMVA analysis for the three lepton channel.

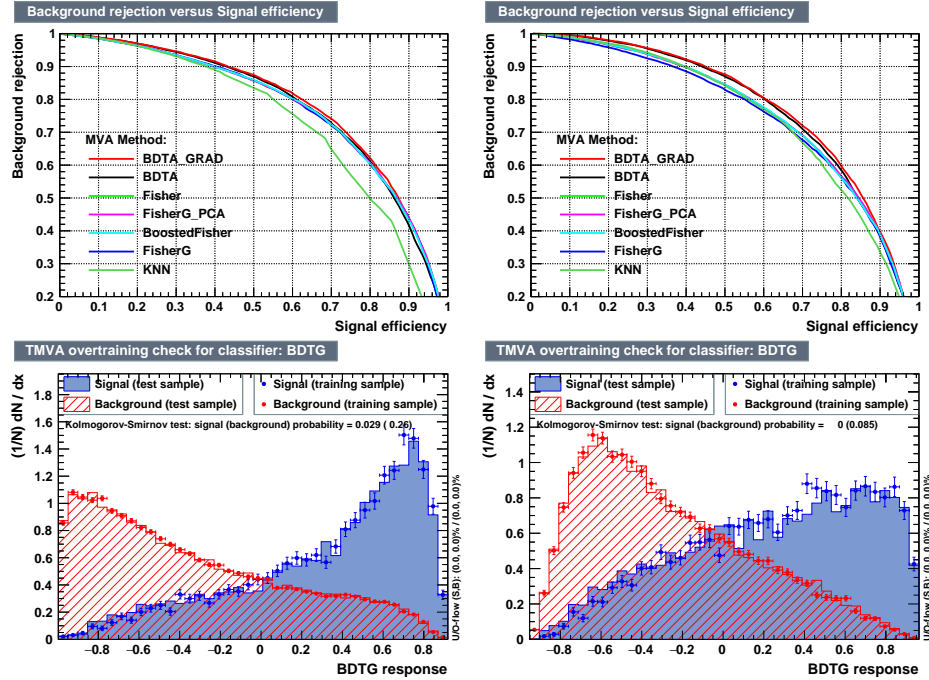


**Figure 6.10:** Top: background rejection vs signal efficiency (ROC curves) for various MVA classifiers (top) in the three lepton channel against  $t\bar{t}V$  (left) and  $t\bar{t}$  (right). Bottom: classifier output distributions for the gradient boosted decision trees, for training against  $t\bar{t}V$  (left) and against  $t\bar{t}$  (right).

2534

## 6.9 Additional discriminating variables

2535 Two additional discriminating variables were tested considering the fact that the  
 2536 forward jet in the background could come from the pileup; since we have a real forward

ttbar training			ttV training		
Rank	Variable	Importance	Variable	Importance	
1	minDRll	1.329e-01	dEtaFwdJetBJet	1.264e-01	
2	dEtaFwdJetClosestLep	1.294e-01	Lep3Pt	1.224e-01	
3	dEtaFwdJetBJet	1.209e-01	maxEtaJet25	1.221e-01	
4	dPhiHighestPtSSPair	1.192e-01	dEtaFwdJet2BJet	1.204e-01	
5	Lep3Pt	1.158e-01	dEtaFwdJetClosestLep	1.177e-01	
6	maxEtaJet25	1.121e-01	minDRll	1.143e-01	
7	dEtaFwdJet2BJet	9.363e-02	dPhiHighestPtSSPair	9.777e-02	
8	nJetEta1	6.730e-02	nJet25_Recl	9.034e-02	
9	nJet25_Recl	6.178e-02	nJetEta1	4.749e-02	
10	lepCharge	4.701e-02	lepCharge	4.116e-02	

**Table 6.11:** TMVA input variables ranking for BDTA\_GRAD method for the trainings in the three lepton channel. For both trainings the rankings show almost the same 5 variables in the first places.

---

```

TMVA.Types.kBDT
NTrees=800
BoostType=Grad
Shrinkage=0.10
!UseBaggedGrad
nCuts=50
MaxDepth=3
NegWeightTreatment=PairNegWeightsGlobal
CreateMVAPdfs

```

---

**Table 6.12:** TMVA configuration used in the BDT training.

jet in the signal, it could give some improvement in the discriminating power. The additional variables describe the forward jet momentum (fwdJetPt25) and the forward jet identification(fwdJetPUID). Distributions for these variables in the three lepton channel are shown in the figure 6.11. The forward jet identification distribution show that for both, signal and background, jets are mostly real jets.

The testing was made including in the MVA input one variable at a time, so we can evaluate the dicrimination power of each variable, and then both simultaneously. fwdJetPUID was ranked in the last place in importance (11) in both training (ttV and tt) while fwdJetPt25 was ranked 3 in the ttV training and 7 in the tt training. When training using 12 variables, fwdJetPt25 was ranked 5 and 7 in the ttV and tt

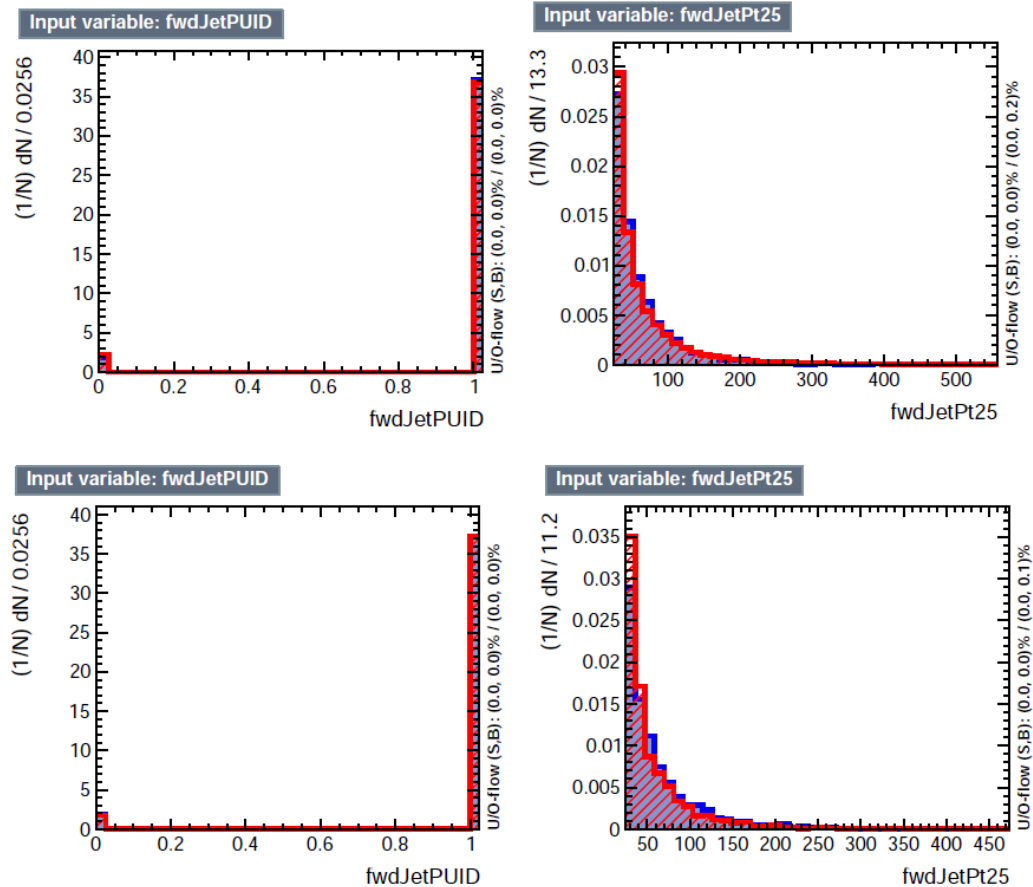


**Figure 6.11:** Additional discriminating variables distributions for ttv training (Top row) and tt training (bottom row) in the three lepton channel. The origin of the jets in the forward jet identification distribution is tagged as 0 for “pileup jets” while “real jets” are tagged as 1.

2547 trainings respectively, while `fwdJetPUID` was ranked 12 in both cases.

2548 The improvement in the discrimination performance provided by the additional  
 2549 variables is about 1%, so it was decided not to include them in the procedure. Table  
 2550 6.13 show the ROC-integral for all the testing cases we made.

ROC-integral	
base 10 var ttv	0.848
+ fwdJetPUID ttv	0.849
+ fwdJetPt25 ttv	0.856
12 var ttv	0.856
<hr/>	
base 10 var tt	0.777
+ fwdJetPUID tt	0.777
+ fwdJetPt25 tt	0.787
12 var	0.787

**Table 6.13:** ROC-integral for all the testing cases we made in the evaluation of the additional variables discriminating power. The improvement in the discrimination performance provided by the additional variables is about 1%

2551 **References**

- 2552 [1] J. Schwinger. "Quantum Electrodynamics. I. A Covariant Formulation". Physical  
2553 Review. 74 (10): 1439-61, (1948).
- 2554 [2] R. P. Feynman. "Space-Time Approach to Quantum Electrodynamics". Physical  
2555 Review. 76 (6): 769-89, (1949).
- 2556 [3] S. Tomonaga. "On a Relativistically Invariant Formulation of the Quantum  
2557 Theory of Wave Fields". Progress of Theoretical Physics. 1 (2): 27-42, (1946).
- 2558 [4] D.J. Griffiths, "Introduction to electrodynamics". 4th ed. Pearson, (2013).
- 2559 [5] F. Mandl, G. Shaw. "Quantum field theory." Chichester, Wiley (2009).
- 2560 [6] F. Halzen, and A.D. Martin, "Quarks and leptons: An introductory course in  
2561 modern particle physics". New York: Wiley, (1984) .
- 2562 [7] File: Standard\_Model\_of\_Elementary\_Particle\_dark.svg. (2017, June 12)  
2563 Wikimedia Commons, the free media repository. Retrieved November  
2564 27, 2017 from <https://www.collegiate-advanced-electricity.com/single-post/2017/04/10/The-Standard-Model-of-Particle-Physics>.
- 2566 [8] E. Noether, "Invariante Variationsprobleme", Nachrichten von der Gesellschaft  
2567 der Wissenschaften zu Göttingen, mathematisch-physikalische Klasse, vol. 1918,  
2568 pp. 235-257, (1918).

- 2569 [9] C. Patrignani et al. (Particle Data Group), Chin. Phys. C, 40, 100001 (2016)  
2570 and 2017 update.
- 2571 [10] M. Goldhaber, L. Grodzins, A.W. Sunyar “Helicity of Neutrinos”, Phys. Rev.  
2572 109, 1015 (1958).
- 2573 [11] Palanque-Delabrouille N et al. “Neutrino masses and cosmology with Lyman-  
2574 alpha forest power spectrum”, JCAP 11 011 (2015).
- 2575 [12] M. Gell-Mann. “A Schematic Model of Baryons and Mesons”. Physics Letters.  
2576 8 (3): 214-215 (1964).
- 2577 [13] G. Zweig. “An SU(3) Model for Strong Interaction Symmetry and its Breaking”  
2578 (PDF). CERN Report No.8182/TH.401 (1964).
- 2579 [14] G. Zweig. “An SU(3) Model for Strong Interaction Symmetry and its Breaking:  
2580 II” (PDF). CERN Report No.8419/TH.412(1964).
- 2581 [15] M. Gell-Mann. “The Interpretation of the New Particles as Displaced Charged  
2582 Multiplets”. Il Nuovo Cimento 4: 848. (1956).
- 2583 [16] T. Nakano, K, Nishijima. “Charge Independence for V-particles”. Progress of  
2584 Theoretical Physics 10 (5): 581-582. (1953).
- 2585 [17] N. Cabibbo, “Unitary symmetry and leptonic decays” Physical Review Letters,  
2586 vol. 10, no. 12, p. 531, (1963).
- 2587 [18] M.Kobayashi, T.Maskawa, “CP-violation in the renormalizable theory of weak  
2588 interaction,” Progress of Theoretical Physics, vol. 49, no. 2, pp. 652-657, (1973).
- 2589 [19] File: Weak Decay (flipped).svg. (2017, June 12). Wikimedia Commons,  
2590 the free media repository. Retrieved November 27, 2017 from

- 2591 https://commons.wikimedia.org/w/index.php?title=File:Weak\_Decay\_(flipped)  
2592 .svg&oldid=247498592.
- 2593 [20] Georgia Tech University. Coupling Constants for the Fundamental  
2594 Forces(2005). Retrieved January 10, 2018, from http://hyperphysics.phy-  
2595 astr.gsu.edu/hbase/Forces/couple.html#c2
- 2596 [21] M. Strassler. (May 31, 2013).The Strengths of the Known Forces. Retrieved Jan-  
2597 uary 10, 2018, from https://profmattstrassler.com/articles-and-posts/particle-  
2598 physics-basics/the-known-forces-of-nature/the-strength-of-the-known-forces/
- 2599 [22] S.L. Glashow. “Partial symmetries of weak interactions”, Nucl. Phys. 22 579-  
2600 588, (1961).
- 2601 [23] A. Salam, J.C. Ward. “Electromagnetic and weak interactions”, Physics Letters  
2602 13 168-171, (1964).
- 2603 [24] S. Weinberg, “A model of leptons”, Physical Review Letters, vol. 19, no. 21, p.  
2604 1264, (1967).
- 2605 [25] M. Peskin, D. Schroeder, “An introduction to quantum field theory”. Perseus  
2606 Books Publishing L.L.C., (1995).
- 2607 [26] A. Pich. “The Standard Model of Electroweak Interactions”  
2608 https://arxiv.org/abs/1201.0537
- 2609 [27] F.Bellaiche. (2012, 2 September). “What’s this Higgs boson anyway?”. Retrieved  
2610 from: https://www.quantum-bits.org/?p=233
- 2611 [28] M. Endres et al. Nature 487, 454-458 (2012) doi:10.1038/nature11255

- 2612 [29] F. Englert, R. Brout. “Broken Symmetry and the Mass of Gauge  
 2613 Vector Mesons”. Physical Review Letters. 13 (9): 321-23.(1964)  
 2614 doi:10.1103/PhysRevLett.13.321
- 2615 [30] P.Higgs. “Broken Symmetries and the Masses of Gauge Bosons”. Physical Re-  
 2616 view Letters. 13 (16): 508-509,(1964). doi:10.1103/PhysRevLett.13.508.
- 2617 [31] G.Guralnik, C.R. Hagen and T.W.B. Kibble. “Global Conservation Laws  
 2618 and Massless Particles”. Physical Review Letters. 13 (20): 585-587, (1964).  
 2619 doi:10.1103/PhysRevLett.13.585.
- 2620 [32] CMS collaboration. “Observation of a new boson at a mass of 125 GeV with  
 2621 the CMS experiment at the LHC”. Physics Letters B. 716 (1): 30-61 (2012).  
 2622 arXiv:1207.7235. doi:10.1016/j.physletb.2012.08.021
- 2623 [33] ATLAS collaboration. “Observation of a New Particle in the Search for the Stan-  
 2624 dard Model Higgs Boson with the ATLAS Detector at the LHC”. Physics Letters  
 2625 B. 716 (1): 1-29 (2012). arXiv:1207.7214. doi:10.1016/j.physletb.2012.08.020.
- 2626 [34] ATLAS collaboration; CMS collaboration (26 March 2015). “Combined Mea-  
 2627 surement of the Higgs Boson Mass in pp Collisions at  $\sqrt{s}=7$  and 8 TeV with  
 2628 the ATLAS and CMS Experiments”. Physical Review Letters. 114 (19): 191803.  
 2629 arXiv:1503.07589. doi:10.1103/PhysRevLett.114.191803.
- 2630 [35] LHC InternationalMasterclasses“When protons collide”. Retrieved from [http://atlas.physicsmasterclasses.org/en/zpath\\_protoncollisions.htm](http://atlas.physicsmasterclasses.org/en/zpath_protoncollisions.htm)  
 2631
- 2632 [36] CMS Collaboration, “SM Higgs Branching Ratios and Total Decay Widths (up-  
 2633 date in CERN Report4 2016)”. <https://twiki.cern.ch/twiki/bin/view/LHCPhysics/CERNYellowReportPageBR> , last accessed on 17.12.2017.  
 2634

- 2635 [37] R.Grant V. “Determination of Higgs branching ratios in  $H \rightarrow W^+W^- \rightarrow l\nu jj$   
 2636 and  $H \rightarrow ZZ \rightarrow l^+l^-jj$  channels”. Physics Department, University of Tennessee  
 2637 (Dated: October 31, 2012). Retrieved from <http://aesop.phys.utk.edu/ph611/2012/projects/Riley.pdf>
- 2639 [38] LHC Higgs Cross Section Working Group, Denner, A., Heinemeyer, S. et al.  
 2640 “Standard model Higgs-boson branching ratios with uncertainties”. Eur. Phys.  
 2641 J. C (2011) 71: 1753. <https://doi.org/10.1140/epjc/s10052-011-1753-8>
- 2642 [39] F. Maltoni, K. Paul, T. Stelzer, and S. Willenbrock, “Associated production  
 2643 of Higgs and single top at hadron colliders”, Phys.Rev. D64 (2001) 094023,  
 2644 [hep-ph/0106293].
- 2645 [40] S. Biswas, E. Gabrielli, F. Margaroli, and B. Mele, “Direct constraints on the  
 2646 top-Higgs coupling from the 8 TeV LHC data,” Journal of High Energy Physics,  
 2647 vol. 07, p. 073, (2013).
- 2648 [41] M. Farina, C. Grojean, F. Maltoni, E. Salvioni, and A. Thamm, “Lifting de-  
 2649 generacies in Higgs couplings using single top production in association with a  
 2650 Higgs boson,” Journal of High Energy Physics, vol. 05, p. 022, (2013).
- 2651 [42] T.M. Tait and C.-P. Yuan, “Single top quark production as a window to physics  
 2652 beyond the standard model”, Phys. Rev. D 63 (2000) 014018 [hep-ph/0007298].
- 2653 [43] F. Demartin, F. Maltoni, K. Mawatari, and M. Zaro, “Higgs production in  
 2654 association with a single top quark at the LHC,” European Physical Journal C,  
 2655 vol. 75, p. 267, (2015).

- 2656 [44] CMS Collaboration, “Modelling of the single top-quark production in associa-  
2657 tion with the Higgs boson at 13 TeV.” [https://twiki.cern.ch/twiki/bin/](https://twiki.cern.ch/twiki/bin/viewauth/CMS/SingleTopHiggsGeneration13TeV)  
2658 [viewauth/CMS/SingleTopHiggsGeneration13TeV](#), last accessed on 16.01.2018.
- 2659 [45] CMS Collaboration, “SM Higgs production cross sections at  $\sqrt{s} =$   
2660 13 TeV.” [https://twiki.cern.ch/twiki/bin/](https://twiki.cern.ch/twiki/bin/view/LHCPhysics/CERNYellowReportPageAt13TeV)  
2661 [view/LHCPhysics/CERNYellowReportPageAt13TeV](#), last accessed on 16.01.2018.
- 2662 [46] S. Dawson, The effective W approximation, Nucl. Phys. B 249 (1985) 42.
- 2663 [47] S. Biswas, E. Gabrielli and B. Mele, JHEP 1301 (2013) 088 [[arXiv:1211.0499 \[hep-ph\]](#)].
- 2665 [48] F. Demartin, B. Maier, F. Maltoni, K. Mawatari, and M. Zaro, “tWH associated  
2666 production at the LHC”, European Physical Journal C, vol. 77, p. 34, (2017).  
2667 [arXiv:1607.05862](#)
- 2668 [49] LHC Higgs Cross Section Working Group, “Handbook of LHC Higgs Cross  
2669 Sections: 4.Deciphering the Nature of the Higgs Sector”, [arXiv:1610.07922](#).
- 2670 [50] J. Ellis, D. S. Hwang, K. Sakurai, and M. Takeuchi.“Disentangling Higgs-Top  
2671 Couplings in Associated Production”, JHEP 1404 (2014) 004, [[arXiv:1312.5736](#)].
- 2672 [51] CMS Collaboration, V. Khachatryan et al., “Precise determination of the mass  
2673 of the Higgs boson and tests of compatibility of its couplings with the standard  
2674 model predictions using proton collisions at 7 and 8 TeV,” [arXiv:1412.8662](#).
- 2675 [52] ATLAS Collaboration, G. Aad et al., “Updated coupling measurements of the  
2676 Higgs boson with the ATLAS detector using up to  $25 \text{ fb}^{-1}$  of proton-proton  
2677 collision data”, ATLAS-CONF-2014-009.

- 2678 [53] ATLAS and CMS Collaborations, “Measurements of the Higgs boson produc-  
2679 tion and decay rates and constraints on its couplings from a combined ATLAS  
2680 and CMS analysis of the LHC pp collision data at  $\sqrt{s} = 7$  and 8 TeV,” (2016).  
2681 CERN-EP-2016-100, ATLAS-HIGG-2015-07, CMS-HIG-15-002.
- 2682 [54] File:Cern-accelerator-complex.svg. Wikimedia Commons,  
2683 the free media repository. Retrieved January, 2018 from  
2684 <https://commons.wikimedia.org/wiki/File:Cern-accelerator-complex.svg>
- 2685 [55] J.L. Caron , “Layout of the LEP tunnel including future LHC infrastructures.”,  
2686 (Nov, 1993). A C Collection. Legacy of AC. Pictures from 1992 to 2002. Re-  
2687 trieval from <https://cds.cern.ch/record/841542>
- 2688 [56] M. Vretenar, “The radio-frequency quadrupole”. CERN Yellow Report CERN-  
2689 2013-001, pp.207-223 DOI:10.5170/CERN-2013-001.207. arXiv:1303.6762
- 2690 [57] L.Evans. P. Bryant (editors). “LHC Machine”. JINST 3 S08001 (2008).
- 2691 [58] CERN Photographic Service.“Radio-frequency quadrupole, RFQ-1”, March  
2692 1983, CERN-AC-8303511. Retrieved from <https://cds.cern.ch/record/615852>.
- 2693 [59] CERN Photographic Service “Animation of CERN’s accelerator net-  
2694 work”, 14 October 2013. DOI: 10.17181/cds.1610170 Retrieved from  
2695 <https://videos.cern.ch/record/1610170>
- 2696 [60] C.Sutton. “Particle accelerator”.Encyclopedia Britannica. July 17, 2013. Re-  
2697 trieval from <https://www.britannica.com/technology/particle-accelerator>.
- 2698 [61] L.Guiraud. “Installation of LHC cavity in vacuum tank.”. July 27 2000. CERN-  
2699 AC-0007016. Retrieved from <https://cds.cern.ch/record/41567>.

- 2700 [62] J.L. Caron, “Magnetic field induced by the LHC dipole’s superconducting coils”.  
2701 March 1998. AC Collection. Legacy of AC. Pictures from 1992 to 2002. LHC-  
2702 PHO-1998-325. Retrieved from <https://cds.cern.ch/record/841511>
- 2703 [63] AC Team. “Diagram of an LHC dipole magnet”. June 1999. CERN-DI-9906025  
2704 retrieved from <https://cds.cern.ch/record/40524>.
- 2705 [64] CMS Collaboration “Public CMS Luminosity Information”.  
2706 <https://twiki.cern.ch/twiki/bin/view/CMSPublic/LumiPublicResults#2016>  
2707 \_proton\_proton\_13\_TeV\_collis, last accessed 24.01.2018
- 2708 [65] J.L Caron. “LHC Layout” AC Collection. Legacy of AC. Pictures  
2709 from 1992 to 2002. September 1997, LHC-PHO-1997-060. Retrieved from  
2710 <https://cds.cern.ch/record/841573>.
- 2711 [66] J.A. Coarasa. “The CMS Online Cluster:Setup, Operation and Maintenance  
2712 of an Evolving Cluster”. ISGC 2012, 26 February - 2 March 2012, Academia  
2713 Sinica, Taipei, Taiwan.
- 2714 [67] CMS Collaboration. “The CMS experiment at the CERN LHC” JINST 3 S08004  
2715 (2008).
- 2716 [68] CMS Collaboration. “CMS detector drawings 2012” CMS-PHO-GEN-2012-002.  
2717 Retrieved from <http://cds.cern.ch/record/1433717>.
- 2718 [69] R. Breedon. “View through the CMS detector during the cooldown of the  
2719 solenoid on February 2006. CMS Collection”, February 2006, CMS-PHO-  
2720 OREACH-2005-004, Retrieved from <https://cds.cern.ch/record/930094>.
- 2721 [70] A. Dominguez et. al. “CMS Technical Design Report for the Pixel Detector  
2722 Upgrade”, CERN-LHCC-2012-016. CMS-TDR-11.

- 2723 [71] CMS Collaboration. “Description and performance of track and primary-vertex  
2724 reconstruction with the CMS tracker,” Journal of Instrumentation, vol. 9, no.  
2725 10, p. P10009,(2014).
- 2726 [72] CMS Collaboration and M. Brice. “Images of the CMS Tracker Inner  
2727 Barrel”, November 2008, CMS-PHO-TRACKER-2008-002. Retrieved from  
2728 <https://cds.cern.ch/record/1431467>.
- 2729 [73] M. Weber. “The CMS tracker”. 6th international conference on hyperons, charm  
2730 and beauty hadrons Chicago, June 28-July 3 2004.
- 2731 [74] CMS Collaboration. “Projected Performance of an Upgraded CMS Detector at  
2732 the LHC and HL-LHC: Contribution to the Snowmass Process”. Jul 26, 2013.  
2733 arXiv:1307.7135
- 2734 [75] L. Veillet. “End assembly of HB with EB rails and rotation in-  
2735 side SX ”,January 2002. CMS-PHO-HCAL-2002-002. Retrieved from  
2736 <https://cds.cern.ch/record/42594>.
- 2737 [76] J. Puerta-Pelayo.“First DT+RPC chambers installation round in the  
2738 UX5 cavern.”. January 2007, CMS-PHO-OREACH-2007-001. Retrieved from  
2739 <https://cds.cern.ch/record/1019185>
- 2740 [77] X. Cid Vidal and R. Cid Manzano. “CMS Global Muon Trigger” web  
2741 site: Taking a closer look at LHC. Retrieved from [https://www.lhc-closer.es/taking\\_a\\_closer\\_look\\_at\\_lhc/0.lhc\\_trigger](https://www.lhc-closer.es/taking_a_closer_look_at_lhc/0.lhc_trigger)
- 2743 [78] WLCG Project Office, “Documents & Reference - Tiers - Structure,” (2014).  
2744 <http://wlcg.web.cern.ch/documents-reference> , last accessed on 30.01.2018.

- 2745 [79] CMS Collaboration. “CMSSW Application Framework”,  
 2746 <https://twiki.cern.ch/twiki/bin/view/CMSPublic/WorkBookCMSSWFramework>,  
 2747 last accesses 06.02.2018
- 2748 [80] A. Buckleya, J. Butterworthb, S. Giesekec, et. al. “General-purpose event gen-  
 2749 erators for LHC physics”. arXiv:1101.2599v1 [hep-ph] 13 Jan 2011
- 2750 [81] A. Quadt. “Top Quark Physics at Hadron Colliders”. Advances in the Physics  
 2751 of Particles and Nuclei. Springer-Verlag Berlin Heidelberg. DOI: 10.1007/978-  
 2752 3-540-71060-8 (2007)
- 2753 [82] DurhamHep Data Project, “The Durham HepData Project - PDF Plotter.”  
 2754 <http://hepdata.cedar.ac.uk/pdf/pdf3.html> , last accessed on 02.02.2018.
- 2755 [83] F. Maltoni, G. Ridolfi, and M. Ubiali, “b-initiated processes at the LHC: a  
 2756 reappraisal,” Journal of High Energy Physics, vol. 07, p. 022, (2012).
- 2757 [84] B. Andersson, G. Gustafson, G.Ingelman and T. Sjostrand, “Parton fragmen-  
 2758 tation and string dynamics”, Physics Reports, Vol. 97, No. 2-3, pp. 31-145,  
 2759 1983.
- 2760 [85] CMS Collaboration, “Event generator tunes obtained from underlying event  
 2761 and multiparton scattering measurements;” European Physical Journal C, vol.  
 2762 76, no. 3, p. 155, (2016).
- 2763 [86] J. Alwall et. al., “The automated computation of tree-level and next-to-leading  
 2764 order differential cross sections, and their matching to parton shower simula-  
 2765 tions,” Journal of High Energy Physics, vol. 07, p. 079, (2014).

- 2766 [87] S. Frixione, P. Nason, and C. Oleari, “Matching NLO QCD computations with  
2767 Parton Shower simulations: the POWHEG method,” Journal of High Energy  
2768 Physics, vol. 11, p. 070, (2007).
- 2769 [88] S. Agostinelli et al., “GEANT4: A Simulation toolkit,” Nuclear Instruments  
2770 and Methods in Physics, vol. A506, pp. 250–303, (2003).
- 2771 [89] J.Allison et.al.,“Recent developments in Geant4”, Nuclear Instruments and  
2772 Methods in Physics Research A 835 (2016) 186-225.
- 2773 [90] CMS Collaboration “Full Simulation Offline Guide”, <https://twiki.cern.ch/twiki/bin/view/CMSPublic/SWGuideSimulation>, last accessed 04.02.2018
- 2775 [91] A. Giammanco. “The Fast Simulation of the CMS Experiment” J. Phys.: Conf.  
2776 Ser. 513 022012 (2014)
- 2777 [92] A.M. Sirunyan et. al. “Particle-flow reconstruction and global event description  
2778 with the CMS detector”, JINST 12 P10003 (2017) <https://doi.org/10.1088/1748-0221/12/10/P10003>.
- 2780 [93] The CMS Collaboration. “ Description and performance of track and pri-  
2781 mary vertex reconstruction with the CMS tracker”. JINST 9 P10009 (2014).  
2782 doi:10.1088/1748-0221/9/10/P10009
- 2783 [94] J. Incandela. “Status of the CMS SM Higgs Search” July 4, 2012. Pdf slides.  
2784 Retrieved from [https://indico.cern.ch/event/197461/contributions/1478917/attachments/290954/406673/CMS\\_4July2012\\_Final.pdf](https://indico.cern.ch/event/197461/contributions/1478917/attachments/290954/406673/CMS_4July2012_Final.pdf)
- 2786 [95] P. Billoir and S. Qian, “Simultaneous pattern recognition and track fitting by  
2787 the Kalman filtering method”, Nucl. Instrum. Meth. A 294 219. (1990).

- 2788 [96] W. Adam, R. Fruhwirth, A. Strandlie and T. Todorov, “Reconstruction of  
 2789 electrons with the Gaussian sum filter in the CMS tracker at LHC”, eConf  
 2790 C 0303241 (2003) TULT009 [physics/0306087].
- 2791 [97] K. Rose, “Deterministic Annealing for Clustering, Compression, Classification,  
 2792 Regression and related Optimisation Problems”, Proc. IEEE 86 (1998) 2210.
- 2793 [98] R. Fruhwirth, W. Waltenberger and P. Vanlaer, “ Adaptive Vertex Fitting”,  
 2794 CMS Note 2007-008 (2007).
- 2795 [99] CMS collaboration, “Performance of CMS muon reconstruction in pp collision  
 2796 events at  $\sqrt{s} = 7$  TeV ”, JINST 7 P10002 2012, [arXiv:1206.4071].
- 2797 [100] M. Cacciari, G. P. Salam, and G. Soyez, “The anti- $k_t$  jet clustering algorithm,”  
 2798 Journal of High Energy Physics, vol. 04, p. 063, (2008).
- 2799 [101] B. Dorney. “Anatomy of a Jet in CMS”. Quantum Diaries. June  
 2800 1st, 2011. Retrieved from <https://www.quantumdiaries.org/2011/06/01/anatomy-of-a-jet-in-cms/>
- 2802 [102] The CMS Collaboration.“Event Displays from the high-energy collisions at 7  
 2803 TeV”, May 2010, CMS-PHO-EVENTS-2010-007, Retrieved from <https://cds.cern.ch/record/1429614>.
- 2805 [103] The CMS collaboration. “Determination of jet energy calibration and transverse  
 2806 momentum resolution in CMS”. JINST 6 P11002 (2011). <http://dx.doi.org/10.1088/1748-0221/6/11/P11002>
- 2808 [104] The CMS Collaboration, “Introduction to Jet Energy Corrections at  
 2809 CMS.”. <https://twiki.cern.ch/twiki/bin/view/CMS/IntroToJEC>, last ac-  
 2810 cessed 10.02.2018.

- 2811 [105] CMS Collaboration Collaboration. “Identification of b quark jets at the CMS  
2812 Experiment in the LHC Run 2”. Tech. rep. CMS-PAS-BTV-15-001. Geneva:  
2813 CERN, (2016). <https://cds.cern.ch/record/2138504>.
- 2814 [106] CMS Collaboration Collaboration. “Performance of missing energy reconstruc-  
2815 tion in 13 TeV pp collision data using the CMS detector”. Tech. rep. CMS-PAS-  
2816 JME16-004. Geneva: CERN, 2016. <https://cds.cern.ch/record/2205284>.
- 2817 [107] CMS Collaboration, “New CMS results at Moriond (Electroweak) 2013”,  
2818 Retrieved from <http://cms.web.cern.ch/sites/cms.web.cern.ch/files/>  
2819 [styles/large/public/field/image/HIG13004\\_Event01\\_0.png?itok=L AwZzPHR](#)
- 2820
- 2821 [108] CMS Collaboration, “New CMS results at Moriond (Electroweak) 2013”,  
2822 Retrieved from <http://cms.web.cern.ch/sites/cms.web.cern.ch/>  
2823 [files/styles/large/public/field/image/TOP12035\\_Event01.png?itok=uMdnSqzC](#)
- 2824
- 2825 [109] K. Skovpen. “Event displays highlighting the main properties of heavy flavour  
2826 jets in the CMS Experiment”, Aug 2017, CMS-PHO-EVENTS-2017-006. Re-  
2827 trieved from <https://cds.cern.ch/record/2280025>.
- 2828 [110] G. Cowan. “Topics in statistical data analysis for high-energy physics”.  
2829 arXiv:1012.3589v1
- 2830 [111] A. Hoecker et al., “TMVA-Toolkit for multivariate data analysis”  
2831 arXiv:physics/0703039v5 (2009)

- 2832 [112] L. Lista. “Statistical Methods for Data Analysis in Particle Physics”, 2nd  
2833 ed. Springer International Publishing. (2017) <https://dx.doi.org/10.1007/978-3-319-62840-0>
- 2835 [113] I. Antcheva et al., “ROOT-A C++ framework for petabyte data storage, sta-  
2836 tistical analysis and visualization ,” Computer Physics Communications, vol.  
2837 182, no. 6, pp. 1384â€¢1385, (2011).
- 2838 [114] Y. Coadou. “Boosted decision trees”, ESIPAP, Archamps, 9 Febru-  
2839 ary 2016. Lecture. Retrieved from [https://indico.cern.ch/event/472305/contributions/1982360/attachments/1224979/1792797/ESIPAP\\_MVA160208-BDT.pdf](https://indico.cern.ch/event/472305/contributions/1982360/attachments/1224979/1792797/ESIPAP_MVA160208-BDT.pdf)
- 2842 [115] J.H. Friedman. “Greedy function approximation: A gradient boosting ma-  
2843 chine”. Ann. Statist. Volume 29, Number 5 (2001), 1189-1232. [https://projecteuclid.org/download/pdf\\_1/euclid-aos/1013203451](https://projecteuclid.org/download/pdf_1/euclid-aos/1013203451).
- 2845 [116] F. James, M. Roos, “MINUIT: Function minimization and error analysis”. Cern  
2846 Computer Centre Program Library, Geneve Long Write-up No. D506, 1989
- 2847 [117] J. Neyman and E. S. Pearson, “On the problem of the most efficient tests  
2848 of statistical hypotheses”. Philosophical Transactions of the Royal Society of  
2849 London. Series A, Containing Papers of a Mathematical or Physical Character.  
2850 Vol. 231 (1933), pp. 289-337
- 2851 [118] B. Hespel, F. Maltoni, and E. Vryonidou, “Higgs and Z boson associated pro-  
2852 duction via gluon fusion in the SM and the 2HDM”, JHEP 06 (2015) 065,  
2853 [https://dx.doi.org/10.1007/JHEP06\(2015\)065](https://dx.doi.org/10.1007/JHEP06(2015)065), arXiv:1503.01656.

- 2854 [119] ATLAS Collaboration, “Measurements of Higgs boson produc-  
 2855 tion and couplings in diboson final states with the ATLAS  
 2856 detector at the LHC”, Phys. Lett. B726 (2013) 88âš119,  
 2857 doi:10.1016/j.physletb.2014.05.011,10.1016/j.physletb.2013.08.010,  
 2858 arXiv:1307.1427. [Erratum: Phys. Lett.B734,406(2014)].
- 2859 [120] CMS Collaboration, “Search for the associated production of a Higgs boson  
 2860 with a single top quark in proton-proton collisions at  $\sqrt{s} = 8$  TeV”, JHEP 06  
 2861 (2016) 177,doi:10.1007/JHEP06(2016)177, arXiv:1509.08159.
- 2862 [121] B. Stieger, C. Jordà Lope et al., “Search for Associated Production of a Single  
 2863 Top Quark and a Higgs Boson in Leptonic Channels”, CMS Analysis Note CMS  
 2864 AN-14-140, 2014.
- 2865 [122] M. Peruzzi, C. Mueller, B. Stieger et al., “Search for ttH in multilepton final  
 2866 states at  $\sqrt{s} = 13$  TeV”, CMS Analysis Note CMS AN-16-211, 2016.
- 2867 [123] CMS Collaboration, “Search for H to bbar in association with a single top quark  
 2868 as a test of Higgs boson couplings at  $\sqrt{s} = 13$  TeV”, CMS Physics Analysis  
 2869 Summary CMS-PAS-HIG-16-019, 2016.
- 2870 [124] CMS Collaboration, “Search for production of a Higgs boson and a single top  
 2871 quark in multilepton final states in proton collisions at  $\sqrt{s} = 13$  TeV”, CMS  
 2872 Physics Analysis Summary CMS-PAS-HIG-17-005, 2016.
- 2873 [125] B. WG, “BtagRecommendation80XReReco”, February, 2017. <https://twiki.cern.ch/twiki/bin/view/CMS/BtagRecommendation80XReReco>.

- 2875 [126] CMS Collaboration, “Identification of b quark jets at the CMS Experiment  
2876 in the LHC Run 2”, CMS Physics Analysis Summary CMS-PAS-BTV-15-001,  
2877 2016.
- 2878 [127] M. Peruzzi, F. Romeo, B. Stieger et al., “Search for ttH in multilepton final1  
2879 states at  $\sqrt{s} = 13$  TeV”, CMS Analysis Note CMS AN-17-029, 2017.
- 2880 [128] CMS Collaboration, “Baseline muon selections for Run-II.” <https://twiki.cern.ch/twiki/bin/view/CMSPublic/SWGuideMuonIdRun2>, last accessed on  
2881 24.02.2018.
- 2883 [129] G. Petrucciani and C. Botta, “Two step prompt muon identification”, January,  
2884 2015. <https://indico.cern.ch/event/368007/contribution/2/material/slides/0.pdf>.
- 2886 [130] H. Brun and C. Ochando, “Updated Results on MVA eID with 13 TeV samples”,  
2887 October, 2014. <https://indico.cern.ch/event/298249/contribution/3/material/slides/0.pdf>.
- 2889 [131] K. Rehermann and B. Tweedie, “Efficient Identification of Boosted Semileptonic  
2890 Top Quarks at the LHC”, JHEP 03 (2011) 059, [https://dx.doi.org/10.1007/JHEP03\(2011\)059](https://dx.doi.org/10.1007/JHEP03(2011)059), arXiv:1007.2221.
- 2892 [132] CMS Collaboration. “Tag and Probe”, <https://twiki.cern.ch/twiki/bin/view/CMSPublic/TagAndProbe>, last accessed on 02.03.2018.
- 2894 [133] B. Maier, “SingleTopHiggProduction13TeV”, February, 2016.  
2895 <https://twiki.cern.ch/twiki/bin/viewauth/CMS/SingleTopHiggsGeneration13TeV>.